Max-Planck-Institut für Metallforschung

Stuttgart

Nanopatterning of Poly(ethylene terephthalate) by Plasma Etching

Ellen Wohlfart

Dissertation
an der
Universität Stuttgart

Bericht Nr. 227
Mai 2010

Nanopatterning of Poly(ethylene terephthalate) by Plasma Etching

Von der Fakultät Chemie der Universität Stuttgart
zur Erlangung der Würde eines Doktors der
Naturwissenschaften (Dr. rer. nat.) genehmigte Abhandlung

Vorgelegt von

Dipl.-Ing. Ellen Wohlfart

aus Stuttgart

Hauptberichter:	Prof. Dr. Eduard Arzt
Mitberichter:	Prof. Dr. Joachim Bill
Tag der mündlichen Prüfung:	17.5.2010

Max-Planck-Institut für Metallforschung Stuttgart
und
Institut für Materialwissenschaft der Universität Stuttgart

Stuttgart, März 2010

“Nicht der Beginn wird belohnt, sondern einzig und allein das Durchhalten.“

Katharina von Sienna

Für meine Familie

Danksagung

Die vorliegende Arbeit wurde von Januar 2006 bis März 2010 am Max-Planck-Institut für Metallforschung in Stuttgart angefertigt. Es ist mir ein großes Anliegen an dieser Stelle denjenigen zu danken, die mich bei dieser großen Aufgabe unterstützt und zum Gelingen dieser Arbeit beigetragen haben.

An erster Stelle gilt mein Dank Herrn Prof. E. Arzt für die Möglichkeit, diese interessante Arbeit in seiner Abteilung durchführen zu können unter überaus familienfreundlichen Arbeitsbedingungen.

Herrn Prof. J. Bill danke ich für die freundliche Übernahme des Mitberichts sowie Herrn Prof. E. J. Mittemeijer für die Zusage, den Prüfungsvorsitz zu übernehmen.

Diese Arbeit wäre nicht das geworden was sie jetzt ist, ohne die großartige Unterstützung meiner Betreuerin Dr. A. del Campo. Ihr stetes Interesse und Engagement sowie die vielen wissenschaftlichen Diskussionen und Anregungen waren für die erfolgreiche Durchführung und das Abschließen dieser Arbeit unerlässlich. Dafür bin ich ihr zu großem Dank verpflichtet.

A big thanks goes to Dr. J. P. Fernández Blázquez for all the interesting discussions which provided me a deeper knowledge in the behaviour of polymers. His support in the lab as well as his comments to my work has become indispensable.

Vielen Dank an alle Mitglieder der Chemiegruppe für ihre stete Hilfe und Unterstützung. Besonders bedanken möchte ich mich bei Dr. S. Blöß, der die Vorarbeit zu dieser Doktorarbeit geleistet hat und E. Knoche, die in ihrer Diplomarbeit nicht nur einen wichtigen Beitrag zum Einfluss der Kristallinität auf die Entstehung der Nanostrukturen geliefert hat, sondern auch viele Anfangsprobleme mit unserem neuen Plasmagerät aus dem Weg geräumt hat. M. Wirkner und Dr. J. M. Alonso danke ich für Hilfe in chemischen Fragen.

Für die Einführung und Unterstützung in die Ultramikrotomie möchte ich mich bei M. Sycha, S. Osterloh, U. Salzberger, M. Kelsch und B. Bussmann bedanken. Vielen Dank an P. Kopold für die Arbeit am TEM.

Während der Arbeit mit unserem Plasmagerät sind immer wieder Probleme und Fragen aufgetaucht. T. Ahlinger und J. Eisenlohr von der Firma plasmatechnology waren jederzeit bereit mir schnell weiterzuhelfen und das Plasmagerät nach unseren Wünschen zu verändern. Dafür herzlichen Dank. Für die Durchführung verschiedener Versuche mit anderen Plasmageräten möchte ich mich bei F. Thiele und bei Dr. U. Schweitzer und J. Schneider vom Institut für Plasmaforschung der Uni Stuttgart bedanken.

During my thesis, I had the opportunity to work two weeks at the Instituto de Ciencia y Tecnología de Polímeros in Madrid. I am very grateful for the big support of Prof. A. Bello and Prof. E. Pérez in performing uniaxial tensile tests, WAXS measurements and the interpretation of the results.

Allen Kollegen der Abteilung Arzt möchte ich für das angenehme Arbeitsklima danken. Im Besonderen geht mein Dank an unsere Sekretärin Frau J. Hess, die mir eine große Hilfe war und viele administrative Stolperfallen aus dem Weg geräumt hat. Bei Richard Segar bedanke ich mich für die Hilfe bei der Fertigstellung der Arbeit.

Ein großes Dankeschön geht an Dr. J. Deuschle, C. Miksch und Dr. C. Greiner, die bei allen großen und kleinen Problemen immer zugehört und geholfen haben. Ohne Sie hätte die Arbeit nur halb so viel Spaß gemacht.

Eine Promotion ist eine große Aufgabe, die ohne Unterstützung im Privaten kaum machbar ist. Dafür möchte ich mich ganz herzlich bei meiner Familie, M. Krpic und ganz besonders bei meinem Mann Alexander Goerke bedanken, ohne dessen Rückhalt und Geduld diese Arbeit kaum möglich gewesen wäre.

Index

Symbols and Abbreviations

Symbols

c	Crystalline fraction [-]
d	Distance between two bodies/atoms [m]
E_{VdW}	Van-der-Waals energy [J]
F_{cap}	Capillary force [N]
F_{el}	Electrostatic force [N]
F_{VdW}	Van-der-Waals force [N]
h	Height [m]
H	Hamaker constant [J]
k	Coulomb constant [Nm^2/C^2]
L	Substrate thickness [m]
l_0	Length [m]
p	Pressure [bar]
P	Power [W]
$<P_2>$	Average degree of orientation [-]
q	Force of spherical charge [C]
q_+	Flux of positive ions [W/m^2]
$q_L(T)$	Heat loss function [W/m^2]
$q_n(T)$	Net flux to the substrate [W/m^2]
r	Ratio of the true area of liquid-solid contact to the projected area [-]
R	Radius [m]
r_1, r_2	Principal radii of surface curvature of the meniscus [m]
R_a	Surface roughness, arithmetic average of the absolute values [µm]
T	Temperature [°C]
t	Time [s]
T_0	Wall temperature [K]
t_{ann}	Annealing time [min]
U	Voltage [V]

v	Stretching rate [mm/min]
v_e	Total etching rate [nm/min]
$v_{e,a}$	Etching rate of the amorphous phase [nm/min]
$v_{e,c}$	Etching rate of the crystalline phase [nm/min]
w_c	Degree of crystallinity [-]
α	Accomodation coefficient for molecular heat transfer [-]
γ_{lv}	Interfacial free energy per unit area for the liquid-vapour interface [N/m^2]
γ_{sl}	Interfacial free energy per unit area for the solid-liquid interface [N/m^2]
γ_{sv}	Interfacial free energy per unit area for the solid-vapour interface [N/m^2]
Δh_0^m	Melting enthalpy of 100% crystalline polymer [J/g]
Δh^m	Melting enthalpy [J/g]
Δp	Laplace pressure [Pa]
ε	Elongation [%]
ε	Surface radiation emissivity constant [-]
θ	Contact angle [°]
θ^{CB}	Apparent contact angle according to Cassie and Baxter [°]
θ_e	Equilibrium angle of contact [°]
θ^W	Apparent contact angle according to Wenzel [°]
κ_g	Thermal conductivity of gas [W/Km]
Λ_0	Molecular thermal conductivity of gas [W/m^{2}KPa]
ρ	Density [g/cm^3]
σ_{SB}	Stefan-Boltzmann constant [W/m^{2}K^4]
φ_{air}	Area fraction of air [-]
φ_s	Area fraction of solid [-]

Abbreviations

AFM	Atomic force microscopy
Ar	Argon
AuPd	Gold palladium
CA	Contact angle
CF_4	Methane
DMT	Dimethylterephthalate
DSC	Differential scanning calometry
e-beam	Electron beam
EG	Ethylene glycol
F	Fluorine
H_2O	Water
HAR	High aspect ratio
He	Helium
LMWF	Low molecular weight fragments
MD	Machine direction
MEH-PPV	Poly(2-methoxy-5-(20-ethylhexyloxy)-1,4-phenylenevinylene)
N/N_2	Nitrogen
N_2O	Nitrous oxide
Nd	Neodymium
NH_3	Ammonia
O/O_2	Oxygen
PA66	Polyamide
PBT	Poly(buthylene terephthalate)
PDMS	Polydimethylsiloxane
PE	Polyethylene
PEDOT:PSS	Poly(3,4-ethylenedioxythiophene) poly(styrenesulfonate)
PEM	Polyelectrolyte multilayers
PEN	Poly(ethylene naphthalate)
PET	Poly(ethylene terephthalate)

PMMA	Polymethylmethacrylate
PP	Polypropylene
PPY	Polypyrrole
PS	Polystyrene
PTFE	Poly(tetrafluoroethylene)
PVDF	Polyvinylidene difluoride
rf	Radio frequency
RIE	Reactive ion etching
RuO_4	Ruthenium tetraoxide
SEM	Scanning electron microscopy
SF_6	Sulfur hexafluoride
Si	Silicon
SU8	1-methoxy-2-propylacetate
T_c	Crystallisation temperature
TD	Transverse direction
TEM	Transmission electron microscopy
T_g	Glass transition temperature
TiO_2	Titanium dioxide
TPA	Terephthalic acid
UHMW	Ultra high molecular weigth
UV	Ultraviolet
VUV	Vacuum ultraviolet
VdW	Van der Waals
WAXS	Wide-angle X-ray diffraction
YAG	Yttrium aluminium garnet

Ellen Wohlfart

Nanopatterning of Poly(ethylene terephthalate) by Plasma Etching

Institute of Materials Science, University of Stuttgart and
Max Planck Institute for Metals Research, Stuttgart, 2010

179 pages, 84 figures, 12 tables

Abstract: Nano and microstructured surfaces found on shark skins, lotus plants, moth eyes or gecko feet can reduce flow resistance, generate self-cleaning surfaces, antireflection layers or reversible adhesion forces. Great interest has developed in transferring the principles of nature to technical applications. Therefore, different patterning techniques have been developed, such as optical, e-beam, or soft lithography, to generate micro and nanostructures on material surfaces. However, all of these techniques have limitations. Most of them require special equipment, are time consuming, expensive or can only structure small areas. In this thesis a simpler, time-saving and less costly patterning procedure is developed which relies on reactive ion etching of polymer surfaces. High aspect ratio nano structures with diameters between 15 and 40 nm and lengths up to 1 µm were fabricated on Poly(ethylene terephthalate). A systematic study of the influence of plasma and polymer parameters was performed to understand and control structure formation during plasma treatment. Commercial and laboratory-made films with different amounts of crystallinity and orientation were plasma treated and subsequently analysed using scanning electron microscopy, weight loss measurements, differential scanning calometry and wide-angle x-ray diffraction. Fibril length could be adjusted by variation of plasma parameters, whereas the polymer microstructure influenced material response to plasma treatment and therefore the resultant surface design. Different etching rates in domains of different order, generated by thermal and mechanical pretreatment, was considered as the mechanism for fibril generation. The nanostructured surfaces exhibited very low adhesion compared to flat analogues and an increasing friction coefficient with increasing surface roughness. By combining plasma treatment with fluorinated coatings, superhydrophobic surfaces with a lotus effect were obtained.

Ellen Wohlfart

Nanopatterning of Poly(ethylene terephthalate) by Plasma Etching

Institut für Materialwissenschaft, Universität Stuttgart und
Max-Planck-Institut für Metallforschung, Stuttgart, 2010

179 Seiten, 84 Abbildungen, 12 Tabellen

Kurzzusammenfassung: Nano- und mikrostrukturierte Oberflächen auf der Haifischhaut, der Lotuspflanze, den Mottenaugen oder den Geckofüßen reduzieren den Reibungswiderstand, erzeugen selbstreinigende Oberflächen, entspiegelnde Beschichtungen oder reversible Haftung. Es ist ein großes Interesse entstanden, die Prinzipien der Natur auf technische Anwendungen zu übertragen. Deshalb wurden unterschiedliche Strukturierungsmethoden wie zum Beispiel Lithographieverfahren entwickelt. Allerdings haben alle Techniken Beschränkungen. Sie benötigen eine spezielle Ausrüstung, sind sehr zeitintensiv, teuer oder es können nur kleine Flächen strukturiert werden. In der vorliegenden Arbeit wurde eine einfache Strukturierungsmethode entwickelt, die auf reaktivem Ionenätzen von Polymeroberflächen basiert. Strukturen mit einem hohen Aspektverhältnis, einem Durchmesser zwischen 15 und 40 nm und einer Länge bis zu 1 µm konnten auf Polyethylenterephthalat hergestellt werden. Es wurden systematische Untersuchungen durchgeführt, um den Einfluss der Plasma- und Polymerparameter auf die Strukturentstehung zu verstehen und zu kontrollieren. Dazu wurden Filme mit unterschiedlicher Kristallinität und Orientierung plasmabehandelt und anschließend mit Rasterelektronenmikroskopie, Gewichtsverlustmessungen, Dynamischer Differenzkalorimetrie und Weitwinkel-Röntgenstreuung analysiert. Durch Variation der Plasmaparameter konnte die Säulenlänge eingestellt werden, während die Mikrostruktur des Polymers die erhaltene Oberflächenstruktur bestimmte. Vermutlich sind unterschiedliche Ätzraten in Domänen mit unterschiedlicher Ordnung (entstanden durch thermische und mechanische Vorbehandlungen) verantwortlich für die Entstehung der Nanosäulen. Kombiniert man die Plasmabehandlung mit einer fluorhaltigen Beschichtung, so erhält man superhydrophobe Oberflächen mit Lotuseffekt. Die strukturierten Oberflächen zeigen eine geringe Adhäsion im Vergleich zu glatten Proben und einen steigenden Reibungskoeffizienten mit zunehmender Substratrauigkeit.

1. Introduction and Motivation

Hairy adhesive pads are found among several animal species like geckos, flies, beetles and spiders [1-5]. They enable strong but reversible adhesion when the animal is climbing steep or overhanging smooth surfaces. In an effort to mimic nature's reversible adhesion principle, different structuring methods have been applied to obtain micro- and nanostructured surfaces with similar adhesion performance [6]. Optical [7-10], e-beam [11], and soft lithography [7-10, 12] have been used to obtain regular, well-defined micron and submicron structures, but with simple geometries, reduced aspect ratio and over small areas. Arrays of carbon nanotubes have also been developed and show high adhesion forces but no reversibility [13-16]. Replication of a lithographic master with polymeric materials has also been proposed as a more efficient and less costly fabrication method [12, 17-19]. However, replication processes involving nanosized structures with high aspect ratio easily break during demoulding and require previous manufacture of costly master by lithography processes.

There is no doubt that the implementation of gecko-inspired adhesives into consumer articles requires the development of a simpler, time-saving and less costly patterning procedure that do not rely on the use of lithographic templates or highly specialized equipment. In this context, the control of surface roughness during plasma treatment of polymer surfaces seems to be an attractive alternative. During plasma treatment, the surface of a material is exposed to a broad spectrum of ions, electrons, excited neutrals, radicals, UV and VUV radiation. On a polymer surface, these species may cause melting, etching and grafting processes at the surface. As a result, the surface chemical composition and topography undergo significant changes and surface properties are modified. These changes depend on the initial chemical nature and physical state of the material, as well as on the plasma treatment conditions applied [20].

In semicrystalline polymers, crystalline and amorphous domains at the surface are expected to show different responses to plasma treatment. Amorphous domains are

generally more susceptible to plasma etching than crystalline domains and, therefore, etching preferentially erodes the amorphous domains and leaves behind the crystalline ones [21]. Such selective etching leads to surface roughening. Recently, interesting surface topographies have been reported upon plasma treatment of different semicrystalline polymers. Nanometer-sized roughness was observed on cellulose fibers after oxygen plasma treatment with a feature size consistent with the dimensions of crystalline microfibrils [22]. Hills and ridges aligned perpendicular to the final draw direction of the film, or fibrillar structures with fibrils with 20 nm in diameter and up to 300 nm in length were observed after oxidative plasma treatment of PET films [23-25]. Other geometries have been reported for amorphous materials:

- Bumpy structures with a diameter between 20 and 250 nm and a height up to several hundred nanometers in Polystyrene (PS) using CF_4/O_2 and CF_4 plasmas [26, 27]
- Pins with 70-90 nm thickness and up to 600 nm height after Ar/O_2 plasma treatment of PMMA films [28-32]
- Short and branched walls in PP [33, 34]
- Sponge-like [35, 36] and needle-like [37] topography on Teflon surfaces
- Quasi-periodic dimples with heights between 1.5 and 4.5 µm and a periodicity around 1.5 µm after CF_4-plasma treatment of PDMS [38]
- Randomly-oriented wrinkles on crosslinked PDMS with controllable periodicity in the 50–200 nm range [39-41] and controlled wrinkling on PDMS [42, 43] after O_2 plasma
- Nanohairs in PDMS after SF_6 [44-46] and CF_4/O_2 [47, 48] plasma treatment

These structured surfaces have been studied in terms of their resulting superhydrophobicity and antireflecting properties, but no attempts to study or control the mechanisms of structure formation have been made.

This thesis aims to study in detail the mechanism of pattern formation in semicrystalline polymers and to identify plasma and material parameters that allow control of pattern

geometry. Poly(ethylene terephthalate), PET, was used as semicrystalline polymer. PET samples with different thermal and mechanical treatments were plasma treated under different parameters and the mechanism of pattern formation was analysed. We expected different response of ordered and non-ordered domains to plasma treatment and this was exploited for pattern development. Nanopatterned surfaces with different and controlled geometries were obtained and the correlations between the resulting geometry and the underlying polymer crystalline morphology was investigated. Special effort was paid to identify and understand the formation of hairy structures because of their potential to generate gecko-like adhesives. Wettability, adhesion and frictional properties of the obtained surfaces were tested.

2. Theoretical Background and Literature Review

2.1 Surfaces in nature

Nature created a large diversity of rough surfaces that serve several purposes. Periodic sub-wavelength structures are found in moth eyes [49]. They are conical protuberances about 200 nm in height and spacing (fig. 1a) [50]. This nanostructured surface acts as anti-reflection layer. Light goes through the lens which improves visual faculty of the moth and simultaneously, the nocturnal moths do not reflect any light and are not visible for most natural enemies.

Nano and microstructured surfaces are also found under water. Shark skin exhibit microridge patterns in form of grooves and riblets on each scale (fig. 1b). The grooves, 200 – 500 µm in size, are directed parallel to the longitudinal body axis and match exactly to each other. By means of this pattern, flow resistance is reduced about 5 - 10 % compared to flat analogues [51].

On the skin of pilot whales a pattern of nanoridge-enclosed pores obscured by an enzyme-containing gel is visible (fig. 1c) [52]. These nanoridges are approximately 100 nm deep and 100 – 200 nm thick, surrounding pores with an average pore size of about 0.2 μm^2. Biofouling reduces hydrodynamic efficiency and may negatively affect health if not managed. According to the authors, the plane of attachment of biofoulers is restricted to the level of the margins of the pores or the tips of the nanoridges. Deeper invasion into the pores is not possible without heavy enzymatic digestion. Due to the swimming behaviour of the whales, especially jumping, biofoulers are removed if they are not attached to protected microniches. Nanoroughness of the skin in combination with an enzyme-containing gel and swimming behaviour of the whales prevents microfouling organisms to attach to the skin.

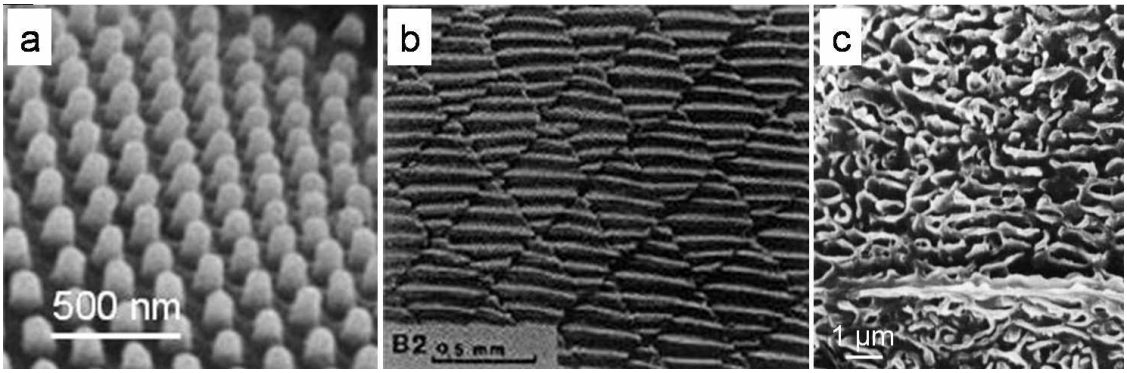

Fig. 1: Examples of structured surfaces found in nature. a) Sub-wavelength structures on moth-eyes (reprinted from ref. [53] with permission from the Royal Society). b) Shark skin surface of Galapagos shark (C. Galapagensis) (reprinted from ref. [54] with kind permission from Springer Science+Business Media). c) Nanoridge-enclosed pores on the skin of pilot whales (reprinted from ref. [52] with kind permission from Springer Science+Business Media).

Lotus plants developed micro and nano structures to keep their leaves free of dirt. The leaf surface is covered with bumps (between 10 and 20 µm in size) consisting of papillose epidermal cells coated with wax crystalloids (100 nm in diameter and more than 1 µm in length) (fig. 2a, b). Particles contaminating the leafe surface are in most cases more readily wetted than the wax components. Thus, these particles are easily removed by water droplets rolling over the surface. Additionally, the so-called lotus effect plays an important role in the defence against pathogens. Spores and pathogenic microorganisms are continuously deposited on the plant surface. For germination most of them need water. Due to the lotus effect, plant leaves are maintained dry and avoid germination on their surface [55-58].

The combination of surface roughness, reduced particle adhesion and water repellency is found in other biological surfaces, not only in plants. Wings in insects are likewise covered with wax crystallites exhibiting dimensions similar to those found in plants. Mainly insects with a big wing surface compared to their body mass like mayfly and dragonfly have very unwettable wings [59]. Dripping water drops remove particles nearly completely.

Carnivorous plants of the genus *Nepenthes* adopt pitcher-like leaves to trap insects. Inside the pitchers a slippery surface keeps insects trapped. This surface consists of a waxy double layer. The wax crystals of the upper layer (length = 1 µm, thickness = 35 nm)

contaminate the adhesive pads of the insects (fig. 2c). They are connected only through small stalks to the substrate and thus break easily when the insects make contact. Moreover, they are very brittle and break easily into tiny pieces. The entire crystals as well as the small fragments adhere well to the insect feet and contaminate the attachment organs. Thus, contact formation between adhesive pads and the surface is affected and adhesion is reduced. Crystals of the lower layer resemble foam with platelets (length = 800 nm, thickness = 40 nm) oriented at acute angles to the substrate (fig. 2d). The high microroughness of this layer decreases real contact area with the adhesive pads of the insects so that they cannot attach properly. The insects thereby slip deeper into the trap where they are digested [60].

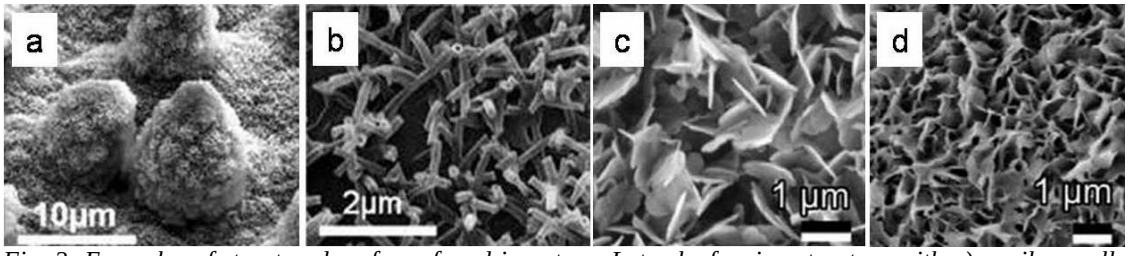

Fig. 2: Examples of structured surfaces found in nature. Lotus leafe microstructure with a) papilose cells and b) wax tubules on it. (Reprinted from ref. [61] with permission from Elsevier.) c) Upper and d) lower wax layer in pitch of Nepenthes plant. (Reproduced from ref. [60] with permission from the Journal of Experimental Biology.)

On the feet of beetles, flies, spiders, and geckos hairy structures are found (fig. 3). These hairs serve as attachment systems which enable them to adhere to and detach from any kind of surface very easily. Interestingly, the size of the hairs scales inversely with the body weight – the bigger the animals, the smaller the terminal elements. While beetles and flies segregate small drops of liquid at the tip of these hairs and adhere due to capillary forces [62-65], spider and geckos adhere mainly by van-der-Waals forces [1, 66]. Geckos are the biggest animals with hairy attachment pads. Their feet are covered by lamellae consisting of millions of setae with a length of about 100 µm. Each seta divides into branches and then terminates into hundreds of tips called spatulae with 200 – 500 nm in size [1, 67]. Adhesion experiments on all hierarchical levels were performed. For the two front feet of a living Gekko gecko an adhesive force of 20 N was measured [68], single setae can generate up to 200 µN in shear [69] and 40 µN in adhesion [70] while single spatulae adhere with 10 nN [71]. If all setae on the toes attached simultaneously, a

gecko could lift 133 kg [72]. Generating such big forces, gecko setae should be very sticky. However, this is not the case. The right orientation to the substrate as well as a small preload and a shear displacement of about 5 µm along the axis of the seta are necessary to generate large shear force. If the initial adhesion of one footstep during wall climbing is not high enough to sustain a gecko's body weight, the animal begins to slide down the wall. Initially not attached spatulae thus come in contact to the substrate through sliding until the force is great enough to support the animal's weight [73]. With this surprisingly large attachment forces it is remarkable that geckos are able to detach their feet in just 15 ms with no measurable detachment force. A simple increase of the setal shaft angle with the substrate to 30° causes detachment. It was proposed that as the angle of the seal shaft increases, sliding stops and stress increases at the trailing etch of the seta. This causes fracture of the seta-substrate bond [69]. Geckos achieve this increase of the setal angle by hyperextension of their toes.

Gecko feet do not seem to stay dirty. Contaminated toes recover their ability to cling to vertical surfaces after only a few steps. No water is involved in self-cleaning. It is suggested that the adhesion between dirt particles and substrate is higher than between dirt particles and spatulae. Thus, during movement the particles stick to the substrate. Only dirt particles which are strongly impacted by the setal surface become irreversibly attached [74].

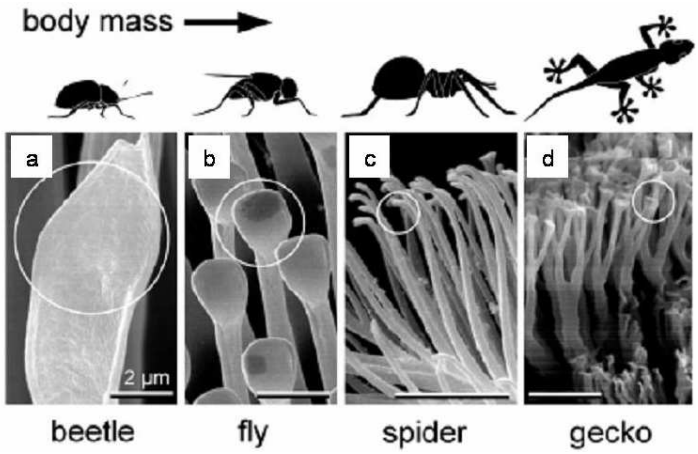

Fig. 3: Hairy attachment structures of a) beetle, b) fly, c) spider, and d) gecko. Dimensions of the terminal elements decrease with increasing body weight of the animals. Simultaneously, number of terminal elements increase. (Reprinted from ref. [75], © PNAS.)

2.2 Overview of patterning techniques for fabrication of structured surfaces

Inspired by rough surfaces in nature a great interest has developed in transferring micro and nano patterns to technical applications. Innovations in the area of micro and nano fabrication have created many different techniques for patterning surfaces in the millimeter to nanometer range. In the following, a short overview will be given about the most important methods.

Lithography is used to transfer a pattern from a mask onto a substrate by means of an etching process. In resist lithography pattern transfer is performed with an irradiation source and a photosensitive polymer material (fig. 4). First, a clean planar surface, typically a silicon wafer, is spin coated with the liquid photoresist. Then, the substrate is "soft baked" in order to remove the solvents in the resist and to improve resist-substrate adhesion. Subsequently, selected parts of the photoresist film by means of a mask are exposed to a light source (UV lamp, electron beam, or x-rays). Thus, photochemical processes in the resist are initiated which change physical and chemical properties in the exposed areas. Most commonly, the solubility of the film in an etchant is modified. Either the solubility of the exposed areas is increased, which leads to a positive image after developing, or it is decreased and a negative image is generated. Lithographic structures down to sub-100 nm dimensions can be generated [76-81]. Furthermore, it is possible to fabricate complex patterns such as high aspect ratio, tilted, suspended, curved, hierarchical, or 3D geometries (fig. 6a) [82]. Disadvantages of photolithography are the complicated structuring of polymeric or curved substrates. It needs several steps and it is not possible to pattern large areas. In addition, the chemicals involved are incompatible with many organic materials [82].

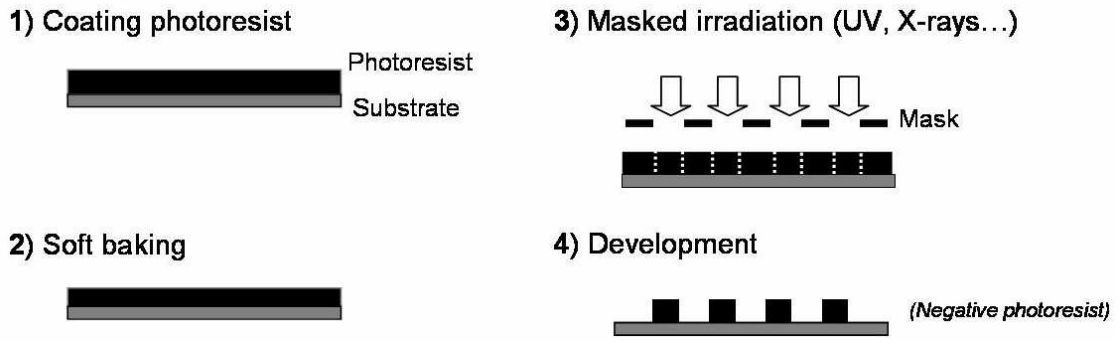

Fig. 4: Photolithographic structuring: Photoresist is spin coated on a clean substrate. After soft baking selected parts of the resist film are exposed to a light source, then the film is developed. Courtesy of A. del Campo.

Mask fabrication is difficult, time consuming, and expensive, particularly when only a small number of wafers are to be fabricated. Maskless techniques like laser prototyping present a suitable alternative. Laser prototyping scans the resist surface with UV, nanosecond pulsed, excimer, and Nd:YAG lasers (fig. 5a). Thus, larger areas can be patterned than is possible with lithography. Recently, 3D structuring was enabled by picosecond and femtosecond lasers which exhibit higher precision in a single step using two-photon polymerizable systems (fig. 5b). Since laser prototyping relies on photoactivation and development of resist layers, the same procedure of coating, development and rinsing is applied. With two-photon lithography, structures as small as 100 nm have been fabricated (fig. 6b) [83-88]. This method offers high penetration depth such that high aspect ratio structures can be generated. Laser prototyping offers high flexibility in pattern design as no mask, mould, or stamp is required. The equipment is easy to operate and maintain, and processing does not involve vacuum conditions as lithographic methods. 3D structures can be created with high precision [82].

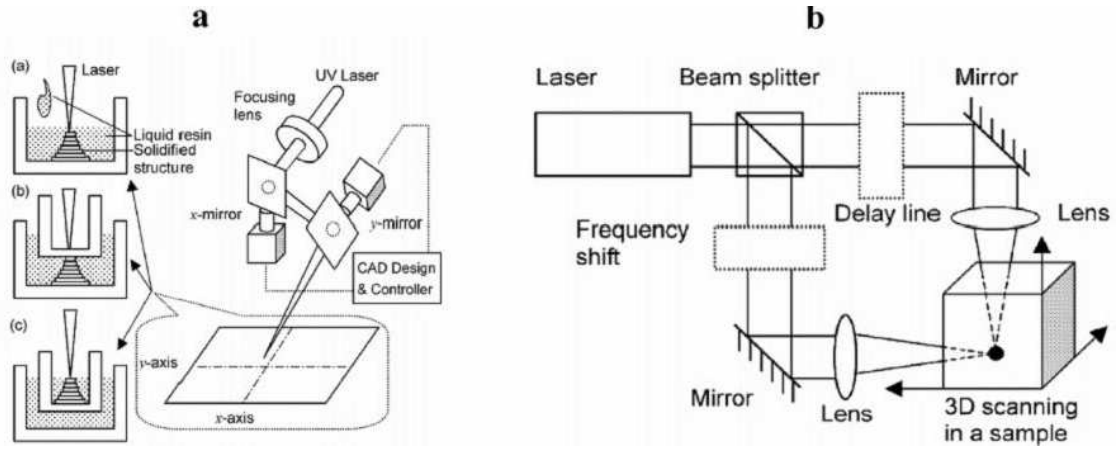

Fig. 5: a) Schematic of a laser prototyping system for stereolithography. Writing is accomplished by mirror scanning angle. b) Schematic of a two-photon lithography system based on a cross-beam two-photon two-colour scanning laser microscope. Pulses from two beams split from an identical laser output overlap in both time and temporal domains, so that absorption process can be launched by simultaneously absorbing two photons. (Reprinted from ref. [85] with kind permission of Springer Science+Business Media.)

Serial writing with charged particles is a maskless lithographic technique using either electrons or ions. In electron beam lithography an electron beam is directed to an electron sensitive resist, most frequently PMMA is used. The impinging electrons generate a cascade of secondary electrons with relatively low energy. Free radicals and radical cations are formed which cause chain scission in the exposed resist film. Subsequently, by developing the sample either the exposed or non-exposed regions are removed from the resist. Very small structures with resolutions of up to 50 nm and aspect ratios of up to 5 have been obtained [89]. The small penetration depth of the electrons restricts the use to layers below 100 nm in thickness. This method has low throughput and is suited only for small area fabrication.

Ion beam lithography, on the other hand, uses high-energy ions and protons which are able to deeply penetrate the resist material with well-defined paths. Penetration depth depends on ion energy. The higher the energy, the deeper is the penetration. Ions interact with electrons and generate low-energy secondary electrons which induce chemical reactions that lead to lithographic imaging. It is possible to fabricate high aspect ratio structures with smooth and vertical side walls and high packing density [90, 91] as well as tilted structures with submicrometer resolution [92, 93]. An example of proton lithography is shown in figure 6c.

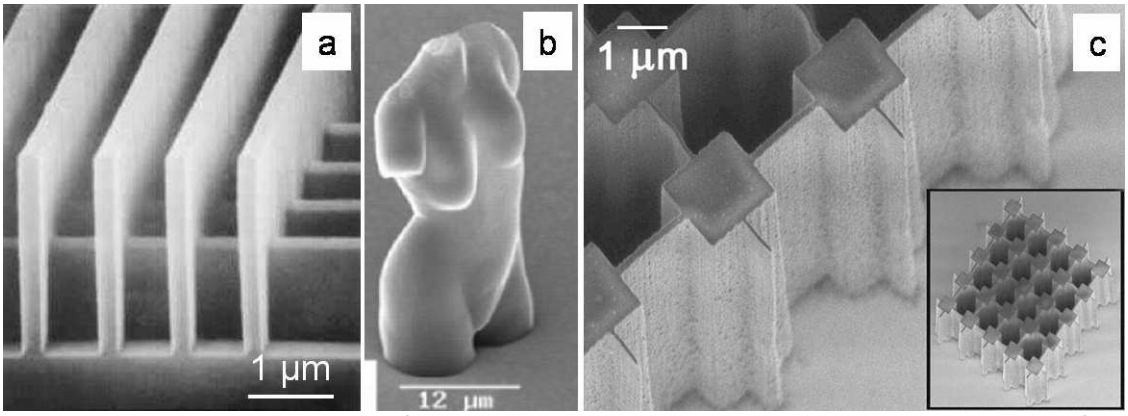

Fig. 6: Micro- and nanostructures fabricated by a) x-ray lithography (reprinted by permission from Macmillan Publishers Ltd: Nature [81], copyright 2000), b) two-photon lithography (reprinted with permission from ref. [87]. Copyright 2003 Wiley-VCH), and c) proton beam lithography. (Reprinted with permission from [94]. Copyright 2003, American Institute of Physics.)

Scanning probe microscopes move an atomically sharp tip in close proximity to or in contact with a surface with subnanometer accuracy. By applying a bias voltage, electrons can be emitted from the tip and expose the resist in a similar way as in electron beam deposition. In scanning probe resist lithography writing speed is very low, but resolution is in the low nanometer range [82, 95].

Scanning probe microscopes can also be used for nanomaching. Machining involves milling material from surfaces in a controlled way. It is a resistless patterning method that can be applied to many different materials. The tip of the scanning probe microscope is in direct contact and displaces material from desired regions of the substrate. Heating the temperature of the tip above the glass transition temperature of the polymer resist facilitates writing. Resolution of this method is very high. It varies from 0.1 nm to micrometer size and is limited by the tip size and the resist thickness. High loading forces are involved which lead to wear of the tips. Wear and contamination of the tips degrade edge resolution with time [82].

Focused ion beam is also used for nanomachining (fig. 8a) [96]. Emitted gallium ions are focused by an electrical field and impinge on the polymer surface. Redeposition of the material is avoided by reaction with a reactive gas and then evacuation from the chamber by a vacuum pump. Secondary electrons generated by collisions of ions with the sample

surface can be detected and enable simultaneous imaging during machining. Rotation and tilt of the sample allows the generation of 3D shapes as well as tilted patterns [97, 98]. The method has a high spatial resolution but is very slow [82].

Direct writing fabrication methods employ a computer-controlled translation stage which moves a material delivery tool (ink-jet print heads or filament microextruders) across a substrate. 3D patterns with controlled architecture and compositions are generated by sequential, layer-by-layer deposition of a fluid (fig. 8b). Subsequently, the fluid is solidified. Rheological properties of the ink like viscosity and viscoelastic proprties are the main restrictions of this method. A wide range of materials can be used. Feature sizes from hundreds of micrometers down to the submicrometer scale can be fabricated [82, 99-101].

One of the oldest and simplest forms of plastic processing is moulding. The surface relief of a hard master tool, which is named mould, template or stamp, is transferred into a softer material. Different methods have been developed for moulding. Thermoplastic polymers are shaped by hot embossing (also called nanoimprint lithography) (fig. 7a) or thermal injection moulding. Pattering occurs by conformal contact of a nanostructured mould using heat and pressure [102]. Heat reduces viscosity of the polymer and the applied pressure causes the polymer melt to flow into the cavities of the mould. Then the melt is hardened by cooling and can be separated from the mould. In injection moulding polymer melts with relatively low viscosity are injected with high pressure through a nozzle into a closed cavity while during hot embossing whole polymer sheets are compressed between the plates of an embossing press against the mould. Pattern up to 25 nm in size were reported [103].

UV nanoimprint lithography makes use of UV-curable polymeric precursors for imprinting. The polymer is coated onto a substrate and pressed against a UV-transparent mould [104-107]. Hardening occurs via UV-irradiation, and then the patterned film can be demoulded.

Soft lithography relies on the use of an elastomeric mould replicated from a micro or nanostructured hard master (fig. 7b) [108]. Usually PDMS is applied. The PDMS mould can be considered as the final moulded structure (fig. 8c), or it can be used as a mould in a subsequent moulding process. It can be easily released from the master or the moulded polymer even in the presence of complex structures. Moreover, its low interfacial free energy and chemical inertness reduce irreversible adhesion. Soft lithography can be applied to large area and high throughput processing, is relatively cheap, very flexible in terms of geometry and curvature of the surfaces, and a range of materials can be moulded [82].

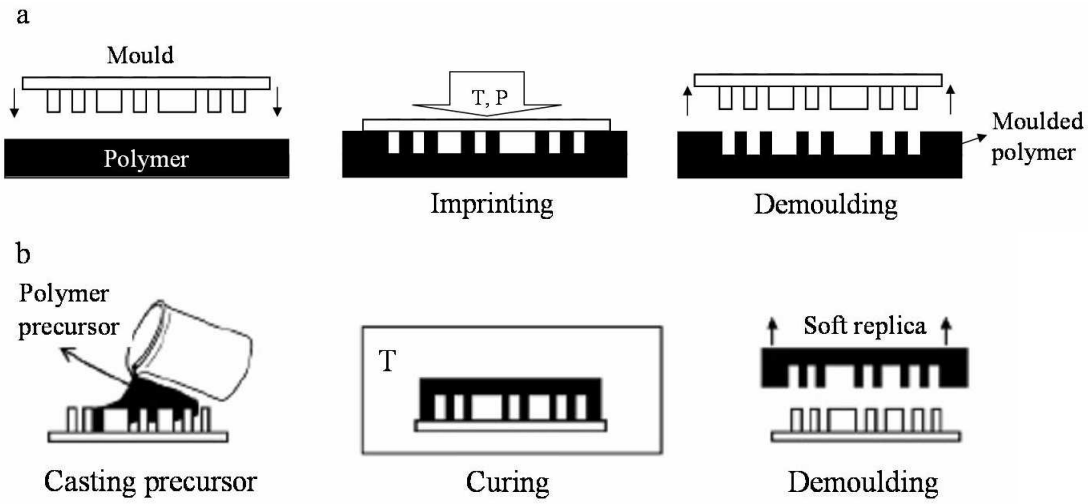

Fig. 7: Soft moulding processes. a) Hot embossing, and b) soft lithography. Courtesy of A. del Campo.

Solvent-assisted moulding relies on the use of solvents for softening polymer films. By placing the spin-coated film and the soft PDMS mould in contact, the polymer solution fills the cavities of the mould due to capillary forces. The solvent is then removed by diffusion into and evaporation through the mould [109-114].

In the whole process, mould fabrication is the most time- and cost-consuming step [115]. It constitutes the biggest limitation in the industrial application of moulding to patterning surfaces. Therefore, a master is usually fabricated and copies of this master in other hard materials are used as moulds for imprinting. Thus, the risk of mould damage and loss is reduced. After the mould is imprinted, demoulding has to be performed very carefully to

avoid pattern damage, especially in high aspect ratio structures. Damage can occur due to adhesion and friction between mould and polymer because of surface roughness, trapping of the polymer or mechanical stress. To avoid this, moulds with low sidewall roughness, tapered geometries and antisticking surface coatings should be used [82, 116].

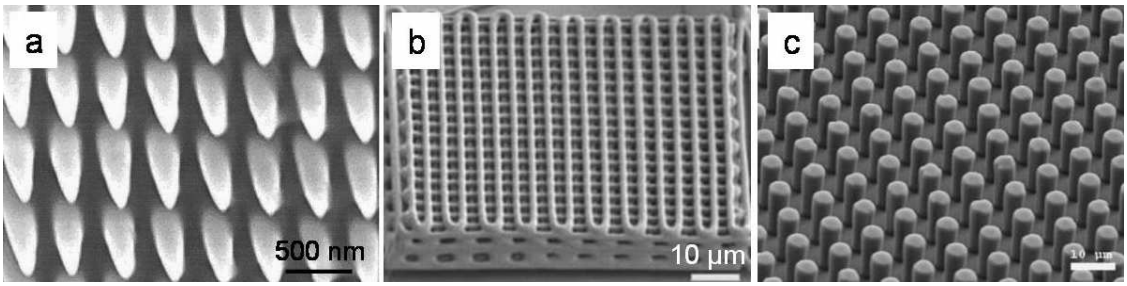

Fig. 8: Micro- and nanostructures fabricated by a) focused ion beam (Reprinted with permission from [97]. Copyright 2005, American Institute of Physics.), b) direct writing (Reprinted by permission from Macmillan Publishers Ltd: Nature [99], copyright 2004), and c) soft lithography. (*Reprinted with permission from [117]. Copyright 2007 American Chemical Society.)*

Transfer printing is a method to transfer negative replicas from a soft mould to a different substrate. A polymer layer is spin coated onto the mould instead of onto the substrate. After solvent evaporation the thin polymer film can be transferred to the substrate by "bonding" them under suitable temperature and pressure (fig. 10a) [118-123]. Transfer printing is applied on substrates which cannot be easily spin coated with a polymer film [82].

Electric field-induced instabilities can also change surface topography. Placing polymer films onto a plate capacitor and raising the temperature above the glass transition leads to liquid cylindrical bridges spanning the two capacitor plates upon application of an external electrical field. Cooling down below the glass transition temperature while keeping the electrical field on leads to hardening of the polymer and the film retains the surface pattern (fig. 9, 10b) [124, 125]. The resulting pattern on the film surface can be influenced by using a structured upper electrode. With bilayers even hierarchical structures can be generated [126]. Electric field-induced instabilities develop on each interface in different characteristic time constants. This leads to a lateral redistribution of both materials under the electric field. It is also possible to pattern films of block

copolymers [127]. The interface between the different blocks respond in a different way to the applied electrical field than the polymer-air interface.

Film instabilities were explained by a balance of forces on the polymer-air interface. Surface tension minimizes the surface area and stabilizes the homogenous polymer film while the electrical field polarizes the dielectric film. This results in an effective displacement charge density at the liquid-air interface. A local perturbation in the film thickness results in a pressure gradient. This gradient drives a flow of the dielectric liquid in the plane of the film and starts structure formation [82, 125].

A polymer film confined between two close surfaces and a small air gap also generates surface instabilities when heated above the glass transition temperature without applying an electrical field. This process is named lithographically induced self-assembly [82].

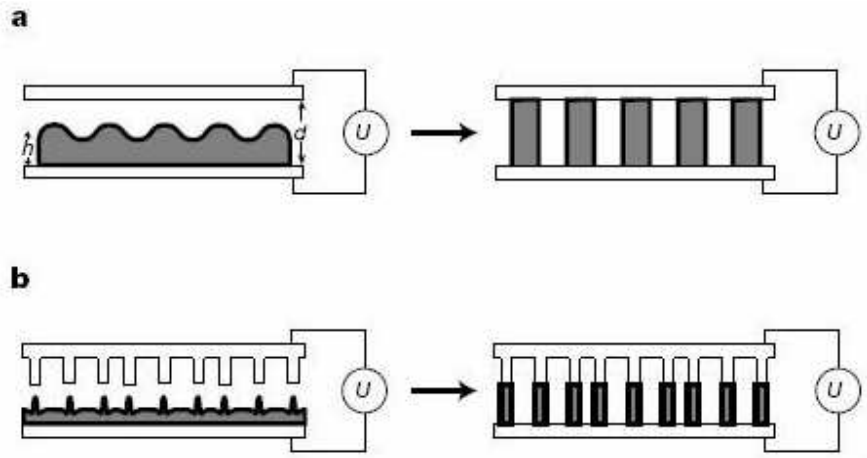

Fig. 9: Patterning through electric field-induced instabilities in a capacitor device. a) The electrostatic pressure acting at the polymer-air interface causes surface instabilities with well-defined wavelength. Polymer columns span the gap between the two electrodes after a certain time. b) A topographical pattern of the top electrode is replicated by the polymer film. (Reprinted by permission from Macmillan Publishers Ltd: Nature [124], copyright 2000.)

Plasma etching can also generate surface structures. Prior to plasma treatment polymer films are patterned with a protective metallic mask by means of lithography. Different etching rates of polymer and metal permits the metal to act as etching mask. Polymer material is removed during plasma treatment while the metal layer remains intact (fig. 10c) [11, 128].

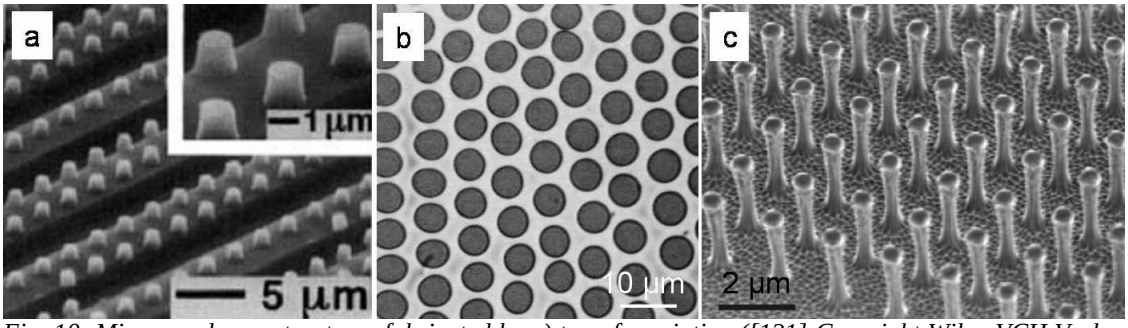

Fig. 10: Micro- and nanostructures fabricated by a) transfer printing ([121] Copyright Wiley-VCH Verlag GmbH & Co. KGaA. Reproduced with permission), b) electrically induced pattern formation (reprinted by permission from Macmillan Publishers Ltd: Nature [124], copyright 2000), and c) plasma etching of a masked polymeric substrate. (Reprinted by permission from Macmillan Publishers Ltd: Nature materials [11], copyright 2003.)

Recently, controlled wrinkling was introduced as a novel method for fabrication of patterned surfaces [42, 43]. An elastomeric substrate, usually PDMS, is stretched and then coated with a thin hard layer. This can be done by spin coating or by oxidation of PDMS either by exposing to UV-ozone or to oxygen plasma. Ozone and plasma treatments create a stiff silica-like material. Applying a tension during ozone or plasma treatment to stretch the PDMS film generates wrinkles in the surface layer after relaxation with a well-defined wave length (fig. 11a, b). The wave length can be tuned by film thickness (depends on plasma intensity) and treatment time. Applying biaxial stretching during plasma treatment generates more complex patterns. After sequential release a herringbone pattern (fig. 11c) is visible while simultaneous release results in disordered wrinkling. Hierarchical structures can be fabricated by plasma treatment and subsequent coating and an embossing step (fig. 11d). The generated patterns can be used for ordered particle deposition in wrinkles by dip coating or for micro contact printing. Wrinkling is a quick and cheap patterning method generating patterns from several hundred nanometers up to about 100 micrometer, which can be applied to big areas. Unfortunately, surface defects and cracks cannot be avoided.

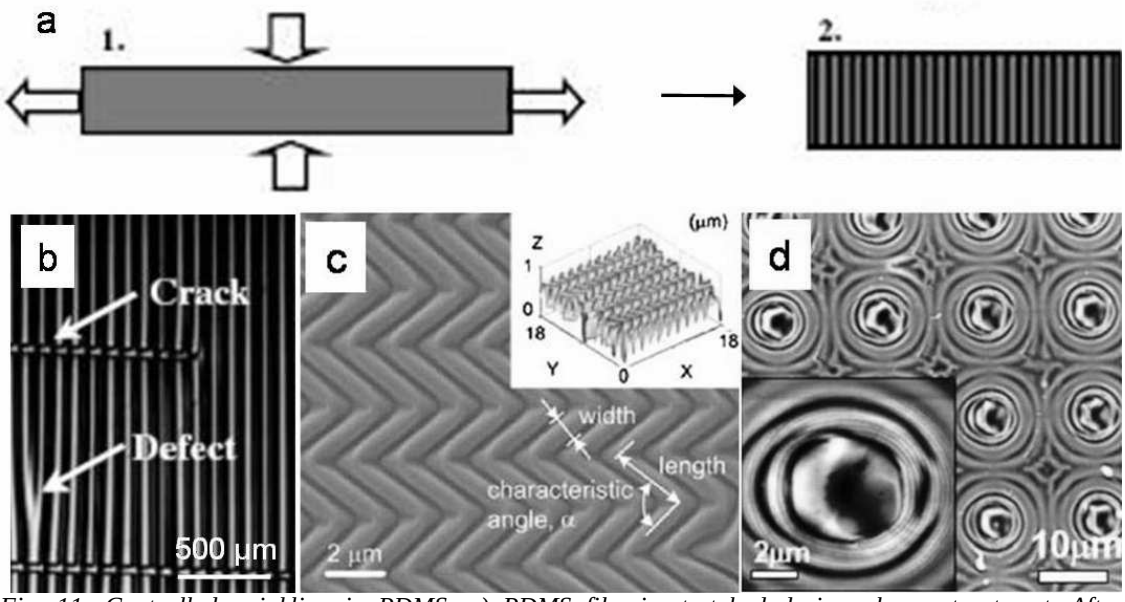

Fig. 11: Controlled wrinkling in PDMS. a) PDMS film is stretched during plasma treatment. After relaxation of the tension the generated silica-like film shows wrinkles with defined wave length. b) PDMS film after uniaxial stretching during plasma treatment. Cracks and defects can be found on the surface. c) PDMS film after biaxial stretching during plasma treatment and sequential release led to herringbone buckling pattern. d) Hierarchical structure generated by plasma treatment of PDMS, coating with PEM, and an embossing step. (With kind permission from Springer Science+Business Media: [42].)

In table 1 the different patterning methods are compared regarding structuring capability and application feasibility in an industrial context [82]. Cost, flexibility, and throughput are the most relevant issues when it comes to manufacturing. There is a big variety of structuring methods but it is evident that none of the techniques satisfies all criteria.

Tab. 1: Capability of high aspect ratio and 3D patterning techniques for industrial and large-area manufacture application (++ high; + medium, - low). (*Adapted with permission from [82]. Copyright 2008 American Chemical Society.)*

Technique	**HAR capability**	**3D capability**	**wet processing**	**mask or mould**	**flexible design**	**cost**	**large area throughput**
UV	++	+	yes	yes	-	+	++
X-ray	++	+	yes	yes	-	++	+
modulated	+	++	yes	yes	-	++	+
interference lithography	+	++	yes	No	+	+	+
laser prototyping	++	++	yes	No	++	+	+
serial writing	+	+	yes	No	-	++	-
machining	+	+	no	No	+	++	-
material deposition	++	++	no	No	++	+	+
moulding	++	+	no	yes	+	-	++
filling membranes	++	-	yes	yes	-	+	-
surface instabilities	+	-	no	optional	-	-	+

The literature review demonstrates that there is a big variety of surface structuring techniques. Nevertheless, all these techniques have limitations. Some need special equipment like clean rooms, masks or templates, the fabrication process is slow, expensive or complicated, and often it is possible to structure only small areas. Plasma etching of polymer surfaces seems to be a promising technique for quick, easy and cheap nanostructuring of big areas. The aim of this work is to investigate if plasma etching of polymer surfaces can serve as a nano patterning technique. The influence of plasma parameter and polymer morphology on resulting nano structures was analysed. Poly(ethylene terephthalate) (PET) was chosen as sample material because it is widely used for several purposes, e.g. packaging, purposes, in the electronics and electrical industry because of excellent electrical properties, or as synthetic fibres in the textile industry. PET is chemically very stable, non-toxic, and exhibits a low crystallization rate, which enables fabrication of samples with adjusted crystallinity. In the following basic information is given about history and fabrication methods of PET as well as plasma state, plasma treatment, and interactions of plasmas with polymer surfaces.

2.3 Poly(ethylene terephthalate) (PET)

At the beginning of this thesis, PET was the only commercial polymer mentioned in literature, which showed the desired fibrillar nanostructures after plasma treatment [24]. Therefore, PET was chosen as material for the experiments. In the following section, the polymer is introduced.

2.3.1 History

Around 1930 a group led by W. H. Carothers at Du Pont developed the first synthetic fiber made of trimethylene glycol and hexadecamethylene dicarboxylic acid. The low melting point of this aliphatic polyester limited its usefulness. About two years later, they also prepared PET for the first time, but the polymer was a sticky resin and not spinnable.

Probably the polymerization was incomplete and excess glycol had not been driven off. At the same time, a polyamide fiber, PA66, was discovered which became the first successful synthetic fibre. A few years later Whinfield and Dickson, unaware of the unsuccessful Du Pont trial, selected the same system. They forced the polymerization to completion and PET, which is the source of the most successful synthetic fiber, was developed [129]. In the 1950s, the polyester fiber industry was born when the process of stretching and uniaxially orienting the fiber was perfected to improve physical properties. The technology of biaxial orientation was developed in the 1960s. The PET sheets were first stretched in one direction and then again perpendicular to this direction. This resulted in a polyester film with enhanced mechanical properties and low gas permeability which was widely used for food packaging, film stock, videotapes, and computer floppy disks [130]. In the 1970s, the production of PET bottles started [129].

2.3.2 Synthesis

PET is produced by using the educts terephthalic acid and ethylene glycol. Two methods are used in industrial manufacture of PET, the preparation from dimethylterephthalate (DMT) and ethylene glycol (EG) or from terephthalic acid (TPA) and EG.

The polymerization of DMT and EG proceeds in two steps: transesterification (1) and polycondensation (2). The two polymerization steps are easily differentiated. The by-product of the transesterification step is methanol, while that of the polycondensation step is EG. In both steps catalysts are used. The polycondensation reaction rate is accelerated by increasing the temperature to around 270°C. EG is removed during the reaction by application of a moderate vacuum [131].

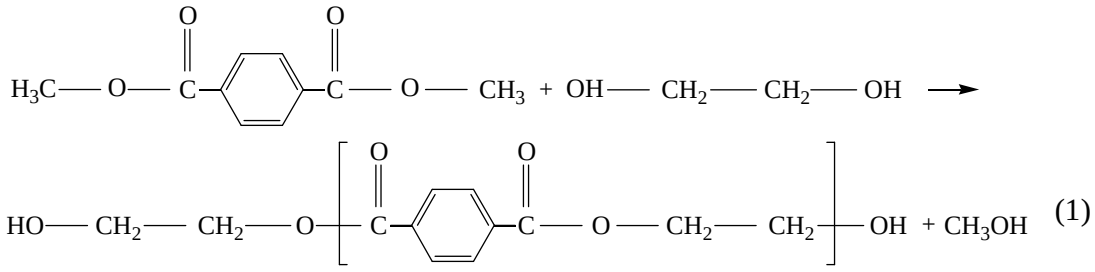

(1)

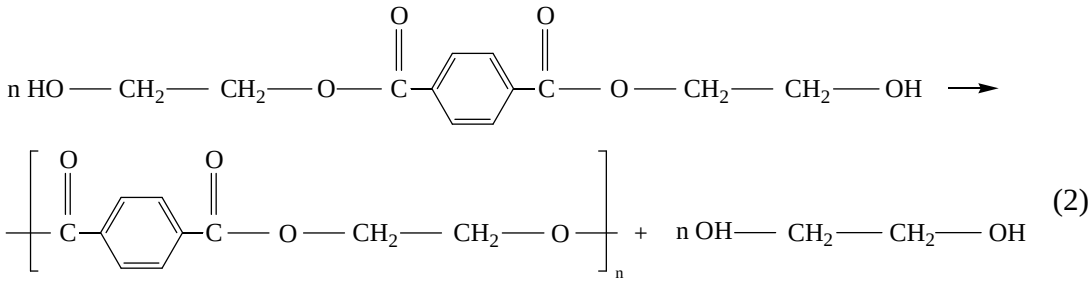

(2)

Preparing PET from TPA and EG requires a catalyst, temperatures between 250 – 300°C and pressure (3). The esterification by-product is water which imposes severe restrictions in the choice of catalysts. Thus, insoluble metal oxides such as TiO_2 are used.

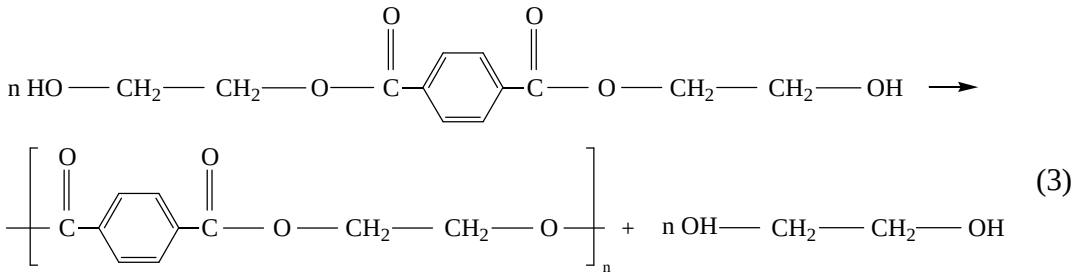

(3)

2.3.3 Properties and processing

PET is a semicrystalline polymer with a triclinic unit cell [132]. The thermoplastic polymer readily crystallizes and can be oriented into highly ordered structures. Heat setting increases dimensional stability at high temperatures (≥ 80°C). In this work mainly biaxial stretched commercial PET films as well as PET fibres are used. Therefore, the manufacturing processes are introduced (fig. 12, 13).

The sequential drawing process consists of four steps (fig. 12), (i) melt extrusion through a slot die and quenching to form an amorphous precursor film, (ii) on-line drawing in the extrusion direction (machine direction, MD), (iii) on-line drawing in the transverse direction (TD), and (iv) on-line heat-setting [133]. Typical values for biaxial stretched films are a melting point around 255°C, a Young´s modulus between 3.6 and 5.2 GPa, and a tensile strength between 150 and 265 MPa [134].

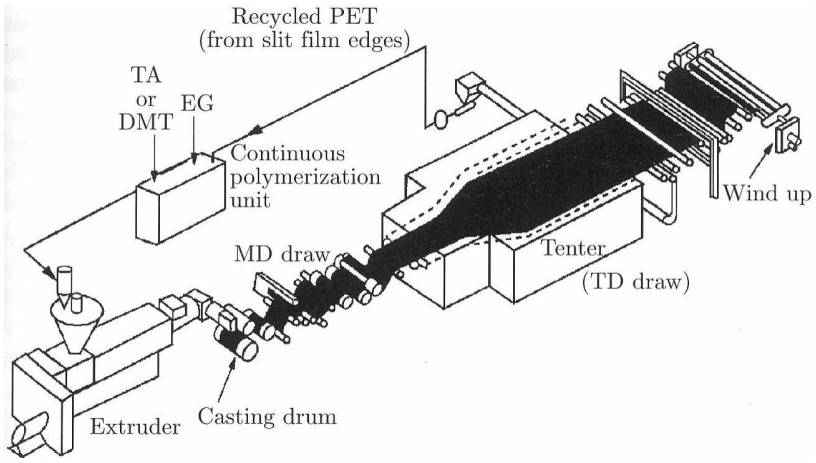

Fig. 12: A typical film manufacturing process (tenter process) showing a sequential drawing combination used to fabricate biaxially oriented PET films [133]. (Copyright Wiley-VCH Verlag GmbH & Co. KGaA. Reproduced with permission.)

PET fibres are produced by melt spinning (fig. 13). A polymer melt, either directly produced by polycondensation or from textile chips fed to an extruder, emerges from the spinneret orifice as molten filament. Within the confined walls of the capillary, the molecules become aligned to some extend during shear flow. As soon as they exit the spinneret into an unconstrained environment, disorientation occurs. A transversely directed quench air stream cools the filament. It solidifies at some distance from the spinneret, called freeze line. The cross-sectional area of the solidified filament is about 100 to 200 times smaller than the initial area close to the spinneret exit. The extrusion velocity of the molten polymer is much lower than the winding speed, which is between 200 and 8000 m/min. Winding speeds of around 1000 m/min result in amorphous filaments with little orientation, an increase to about 3000 m/min generates significant molecular orientation in the amorphous filaments, which enhances storage stability as well as thermal resistance and crystallizability. At speeds higher than 3500 m/min the orienting influence of the uniaxial stress field overcomes to a significant extent the disorienting influence of the thermal relaxation process. Fibres with a high degree of crystallinity and high molecular orientation are generated. Conventional fibres obtain a Young´s modulus between 7 and 10 GPa. High modulus and high strength fibres can be produced via zone drawing and zone melting, two-step drawing or gel spinning. Young´s

moduli up to 39 GPa were reported as well as fibres with a modulus of 29.7 GPa and a tensile strength of 1.7 GPa [135].

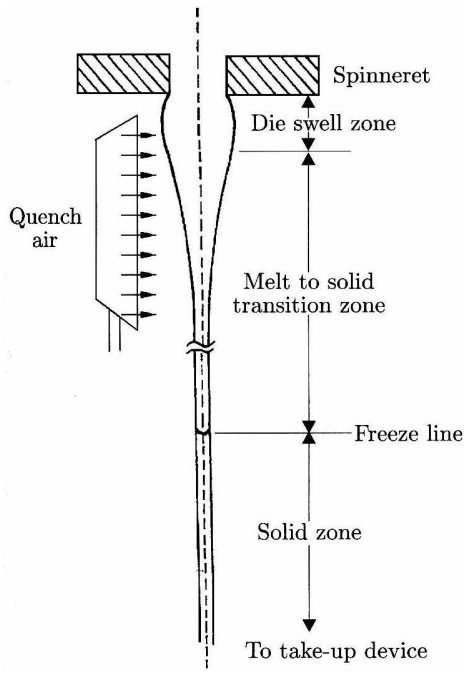

Fig. 13: Schematic representation of the spinline in the melt spinning process of PET fibers [136]. (Copyright Wiley-VCH Verlag GmbH & Co. KGaA. Reproduced with permission.)

2.4 Introduction to plasma etching

2.4.1 Plasma state

Heating up a solid turns it into a liquid, then into a gas. Further heating turns the gas into the plasma state. Therefore, plasma is called the forth state of matter. The plasma state can be considered to be a gaseous mixture of positively and negatively charged particles with approximately equal charge density. Plasmas can be created by increasing the energy content of matter, for example by high-energy radiation, electric fields or thermal energy. Because plasmas lose energy to their surroundings through collision and radiation processes, energy must supplied continuously to the system.

2.4.2 Plasma types

Plasmas can be divided into two broad categories: “hot” and “cold” plasmas. Totally ionized gases are termed hot plasmas or equilibrium plasmas. The temperature of all charged species is extremely high. In cold plasmas (nonequilibrium plasmas) the degrees of ionization are small (0.1 to $5 \cdot 10^{-3}$ %) and the atomic and molecular charged and neutral species have low energies while the electrons have relatively high energies [137].

Only cold plasmas are suitable for lab applications like modification of organic matter. Energy is provided by means of a high frequency field, either inductively or capacitively coupled. In capacitive coupled plasma machines one of the two electrodes is connected to the power supply and the other electrode is grounded. When the upper electrode is grounded it is called plasma etching, the other way round it is called reactive ion etching. The electrodes can be placed either in the plasma chamber or outside. The advantage of outside electrodes lies in the fact that they remain unaffected by erosion or deposition during plasma reactions. Inductively coupled plasmas do not have electrodes. Energy is supplied by electrical currents which are produced by electromagnetic induction.

Because there are a large variety of plasma systems it is very difficult to compare experiments even if the starting conditions are identical. The nature of plasmas, the modalities of transferring electric or electromagnetic field intensities to the reaction system, the geometry of reactors and the selected experimental conditions like pressure, power or processing gas crucially influence the gas phase and surface related chemistry [137]. Thus, for every sample the ideal conditions must be established.

2.4.3 Plasma processes

In a high frequency field, electrons gain energy for ionization processes. Thus the plasma gas contains atoms/molecules, free electrons and ions. Interactions of these particles with each other and with molecules of the sample surface lead to excitation, ionization and

dissociation processes. Many different kinds of particles are generated, a variety of ions, molecular fragment ions, free radicals, ablated volatile molecular fragments and photons. Simultaneously, surface functionalities are altered (Fig. 14). An overview on the main plasma polymer interaction processes and the penetration depths of the generated particles is given in table 2.

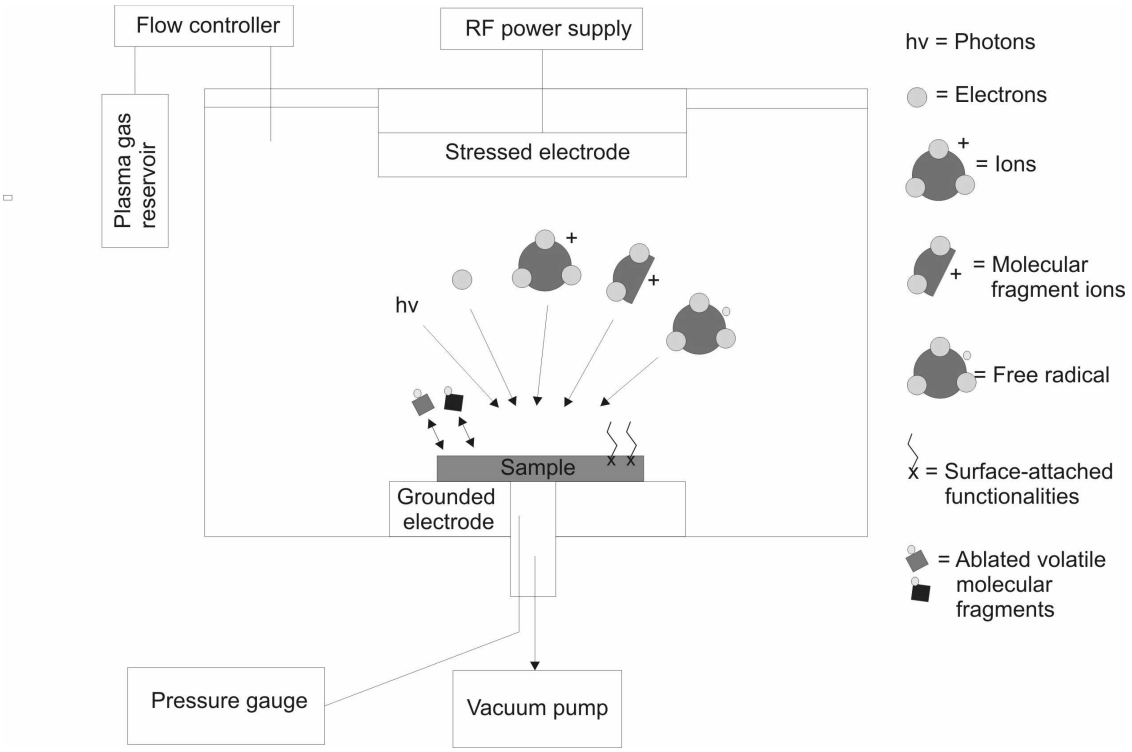

Fig. 14: Schematic diagram of capacitively coupled RF-plasma reactor. The interaction of particles in the plasma with the sample surface is illustrated symbolically. Modified from [137].

Tab. 2: Plasma - polymer interaction processes relevant to surface modification. Modified from [138].

Plasma component	**Energy**	**Main process**	**Penetration depth**
Ions, fast neutrals	ca. 100 eV ca. 10 eV	Elastic collisions: displacement, implantation, sputtering Adsorbate sputtering	2-5 nm Monolayer
Electrons	>5 eV	Inelastic collisions (dissociation, ionization)	Few nanometers
Photons	>5 eV	Photochemical dissociation, ionization	Some 10 nm
Neutrals, radicals	Thermal	Adsorption (chemical reactions) Diffusion (chemical reactions)	Top monolayers Bulk

Plasmas are widely used because of their unique ability to modify polymer surfaces without affecting their bulk properties. Four major effects on surfaces are normally observed [139]. Depending on treatment parameters, one effect may be favoured over another but each effect is always present.

Cleaning: Molecular layers from polymers and all organic contaminations from inorganic surfaces can be removed. The resulting surfaces are extremely clean which results in enhanced bonding of plasma treated surfaces. Most other types of cleaning procedures leave a layer of organic contamination [139].

Ablation: It is possible to clean badly contaminated surfaces, remove weak boundary layers which are formed during the fabrication of a part or to treat filled or semicrystalline materials. Surface topography can be generated because amorphous polymer is removed many times faster than crystalline polymer or inorganic material [139].

Crosslinking: Free radicals are created in the polymer surface which can react with other radicals. This leads to recombination, unsaturation, branching, or crosslinking [139].

Surface chemistry modification: The surface layer of a polymer is altered to create chemical groups. Different gases or gas mixtures are used depending on the type of surface modification that is desired. For example oxygen is used to remove organics by oxidation and to leave oxygen species in the surface. Due to plasma treatment the wettability of polymer surfaces can be altered and adhesive properties can be improved. In table 3 different plasma gases and their applications are listed [139, 140]:

Tab. 3: Plasma gases and their applications

Plasma gas	**Application**
Oxidizing gases (O_2, air, H_2O, N_2O)	Removal of organics by oxidation and to leave oxygen species in the polymer surface
Reducing gases (H_2, mixtures of H_2)	Replacement of F or O in surfaces, removal of oxidation-sensitive materials, conversion of contaminants to low molecular weight species that do not polymerize or re-deposit on adjacent surfaces
Noble gases (Ar, He)	To generate free radicals in surfaces to cause cross-linking or to generate active sites for further reaction
Active gases (NH_3)	To generate amino groups
Fluorinated gases (CF_4, SF_6 and other perfluorinated gases)	To make the surface inert and hydrophobic
Polymerizing gases (monomer gases for direct polymerization, Ar or He pretreated)	Polymerization of layers onto substrates by direct polymerization or by grafting on Ar or He pretreated polymer surface

Plasma etching of polymer samples involves degradation of the chains due to ion bombardment (physical etching) and chemical surface reactions due to radical reactions (chemical modification). Both physical and chemical processes are always present during plasma treatment and never isolated from each other. The balance between the two processes depends on the kind of plasma, plasma operation conditions and material of choice.

When using plasmas for etching surfaces and generation of patterns, there are three important properties to consider: uniformity, selectivity and directionality of the etching process. Uniformity describes the distribution of etch rates across the sample surface. Selectivity is the ratio of etch rates for two materials (or two morphological states of the same material) present in the same sample. Directionality describes the relative etch rates in the vertical and horizontal directions. An isotropic process etches at the same rate in the vertical and horizontal direction. Directional processes are those that etch faster vertically than horizontally. A perfectly anisotropic process etches only in the vertical direction. Fig. 15 contains sketches of representative profiles created by etches of varying directionality. In general, ion-assisted etching leads to anisotropic etching, while etching

mechanisms based on neutral sources (chemical etching) usually lead to isotropic ablation [141].

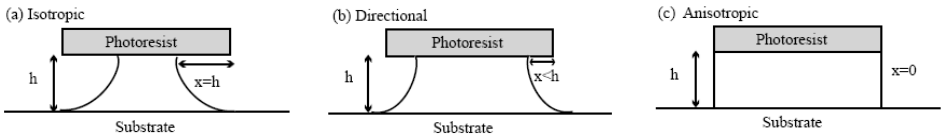

Fig. 15: Possible etching profiles depending on etching mechanisms. a) Isotropic etching, b) directional etching, and c) anisotropic etching. (Reprinted from [141], Copyright 2002 with permission from Elsevier.)

2.5 Fabrication of micro and nanostructures by plasma etching

In the case of semicrystalline polymers, crystalline and amorphous domains at the surface are expected to show different response to plasma treatment. Amorphous domains are generally more susceptible to plasma etching than crystalline domains and, therefore, etching preferentially erodes the amorphous domains and leaves behind the crystalline ones [139]. Such anisotropic etching leads to roughening of the polymer surface. It seems to be a promising method for fabrication of nanostructures on polymeric surfaces because it is a simple, time-saving and less costly patterning procedure that does not rely on the use of lithographic templates or highly specialized equipment. In the following a detailed literature overview is given about plasma structuring of polymer materials.

2.5.1 Semicrystalline polymers

PET films with a crystallinity of 50 % were structured via sputter etching using a 13.56 MHz rf power supply [142]. Although the quality of the SEM pictures is poor and the resolution is quite low, nanostructures are distinguishable after a plasma treatment of 5 and 20 minutes, respectively (fig. 16). Feature size was estimated to be 50 nm in depth and width. Structure formation was explained by differences in the etching rates of crystalline and amorphous regions.

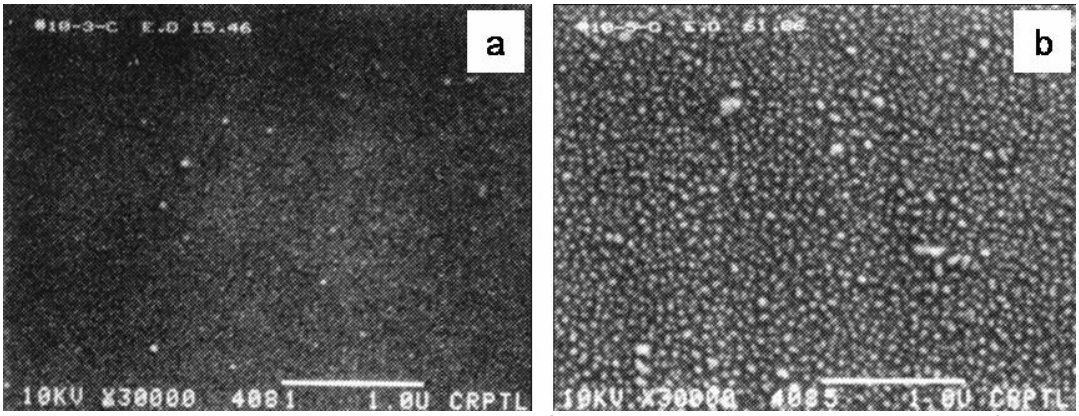

Fig. 16: PET etched with oxygen plasma at 100 W for a) 5 minutes and b) 20 minutes. Small features with a size of 50 nm were generated. (Reprinted with permission from [142]. Copyright 1985, American Institute of Physics.)

Thermanox coverslips (Nalgene Nunc International, Naperville, IL) fabricated of PET were plasma etched with a mixture of 25 % oxygen and 75 % argon gas for 7.5 minutes under a pressure of 0.013 mbar [143]. A high-frequency oscillating power supply created a low energy plasma in the chamber, frequency and plasma power were not specified. Then the samples were rinsed with 70 % ethanol. This cycle was repeated three times. The surface topography was examined by SEM and AFM. The untreated coverslip was very flat (fig. 17a, c), while plasma treatment produced randomly located peaks, ranging from 12 to 170 nm in height (fig. 17b, d). Most of the peaks (70-80%) were approximately 50 nm in height.

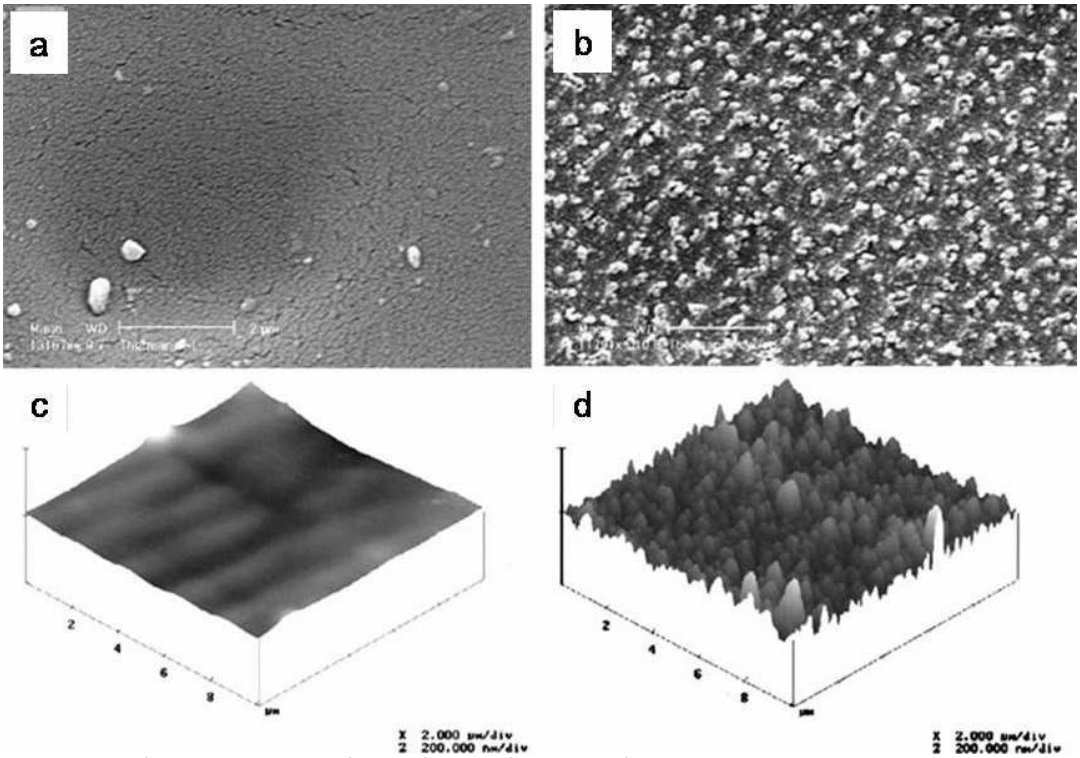

Fig. 17: Surface morphology of PET films before and after plasma treatment. SEM micrographs of a) untreated and b) plasma treated surfaces, and AFM micrographs of the c) untreated and d) plasma treated surface. Randomly located peaks with a height of about 50 nm were generated [143]. (Reprinted with permission from John Wiley & Sons, Inc.)

Thermanox samples were also treated with reactive ion etching using different gas compositions (Ar, N_2, O_2 and 1:1 mixtures of these gases) [24]. The plasma machine operated at 30 kHz, gases were supplied to the system with a rate of 25 sccm under 50 W of power with a pressure of 0.18 mbar in the chamber. Gas mixtures produced topographies intermediate to those of the pure gas morphologies. While argon and nitrogen treatment produced a polygonally patterned surface made up of many small protrusions, oxygen etching produced a distinctive fibrillar structure after a time interval of 10 minutes. The fibrils were 65 to 100 nm long and 20 nm in diameter. Increasing the etching time increased fibril length up to 300 nm and decreased fibril density (fig. 18). Examination of very short treatment times (30 and 60 seconds) revealed a polygonal pattern displaying a relatively large cell size of about of about 200 nm in a transient display of rimtype instabilities (fig. 18a). Additionally, fine scale features in a range of 15 to 20 nm were visible. When treatment time was increased to several minutes, the

polygonal pattern disappeared, the density of the fine scale feature decreased, and nanofibrillar peaks began to form as localized rimtype instabilities (fig. 18b-d).

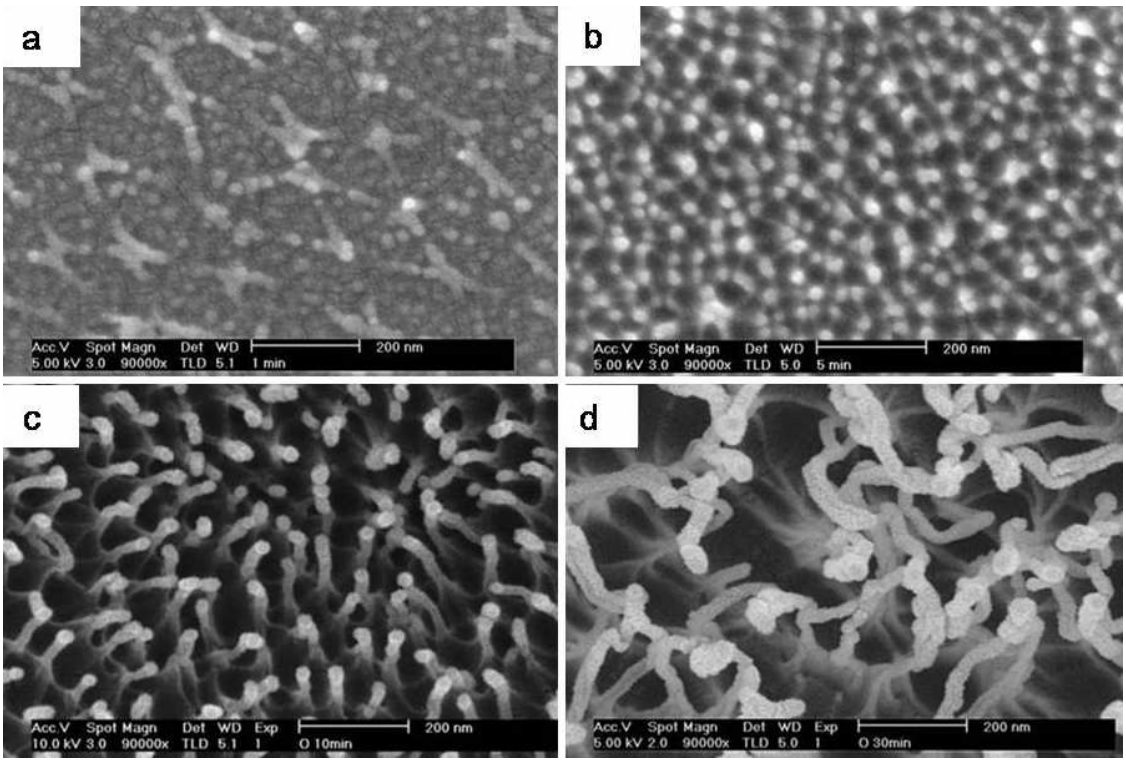

Fig. 18: Reactive ion etching with oxygen plasma led to the formation of nanostructures on PET surface. a) One minute plasma treatment led to a polygonal pattern of fine protrusions and fine scale features. b) After 3 minutes the polygonal pattern disappeared and the fine scale features grew. c) After 10 minutes nanofibrils appeared. d) They increased in size after 30 minutes of plasma treatment. (Reprinted with permission from [24]. Copyright 2003 American Chemical Society.)

Fibril growth was explained as follows. The untreated PET film was a homogenous, single-phase material (fig. 19a). Plasma etching cracked molecule chains, which resulted in a thin film of low molecular weight fragments (LMWF). These relatively polar LMWF formed an unstable nonwetting liquid film on the PET substrate (fig. 19b). Rayleigh instabilities then developed at two different levels. One was locally, with a size of about 20 nm, and the other at a length scale defined by the observed polygons (fig. 19c). In the final morphological stage the smaller scale instabilities were no longer apparent and only the rim and nanofibrillar features, which collected the products of dewetting, were evident (fig. 19d). However, no experimental evidence was provided of the growing mechanism.

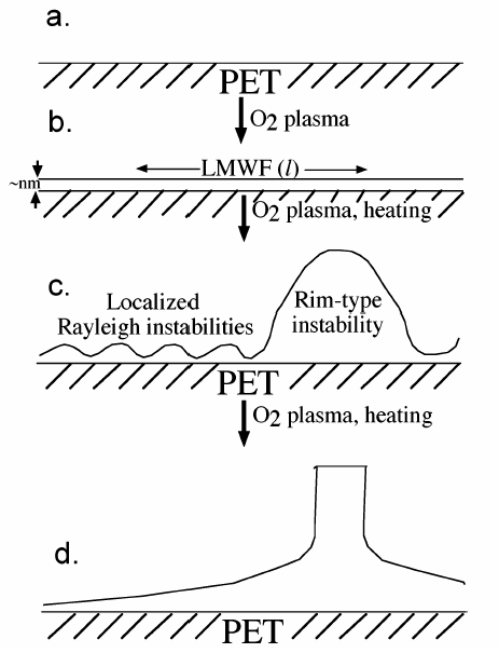

Fig. 19: Proposed mechanism for pattern formation: a) Initial flat PET surface. b) The beginning of plasma etching led to the formation of a thin continuous film of relatively polar low molecular weight fragments (LMWF). c) During the etching process large scale polygonal instabilities nucleated while smaller scale instabilities continued to exist. d) In the final morphological state smaller scale instabilities were no longer apparent, only the rim and nanofibrillar features were evident. (Reprinted with permission from [24]. Copyright 2003 American Chemical Society.)

Teshima and coworkers fabricated an ultra-water repellent PET substrate by first performing plasma etching on PET substrates and subsequent chemical vapour deposition of organosilane precursors [144-146]. The samples were etched for 10 min (13.56 MHz, 0.05 mbar, 100 W) with oxygen plasma. The initial surface was flat (fig. 20a). After 10 min plasma treatment protrusions greater than 10 nm in height could be observed (fig. 20b). The authors explained the appearance of the nanostructures by a higher etching rate in the amorphous parts compared to the crystalline parts in the semicrystalline biaxial stretched PET foil. They also noticed that the protrusions were orderly formed on the surface. The origin of this arrangement is considered to be the orientation and sectional crystallinity of the biaxially stretched PET substrate [144]. It must be commented that AFM cannot image high aspect ratio structures in detail because the tip cannot enter narrow valleys. SEM pictures are more suited for this kind of samples.

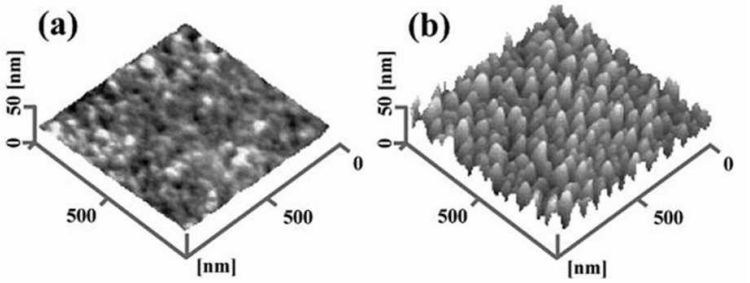

Fig. 20: AFM images of PET surfaces a) before and b) after plasma treatment with oxygen plasma for 10 minutes. (Reprinted with permission from [144]. Copyright 2003 American Chemical Society.)

Biaxially oriented Polyethylene (PE) treated with argon plasma at 13.56 MHz and 100 W generated short and branched walls on the surface. Walls became smaller, closer, and more contorted with increasing treatment time [33].

Superhydrophobic cellulose surface was fabricated by oxygen plasma etching and subsequent fluorocarbon deposition [22]. Each cellulose fibre consisted of several microfibril bundles which in turn were composed of microfibrils. These were 3 to 30 nm in diameter and contained mostly crystalline cellulose moieties while the matrix surrounding the microfibrils was predominantly amorphous. According to the authors roughness in the nanoscale was fabricated on the initially smooth surface because the amorphous parts were etched more strongly than the crystalline regions. The resulting surface exhibited nanoscale features with fibril-like shape.

2.5.2 Amorphous polymers

To decrease surface reflection of Polymethylmethacrylate (PMMA), the polymer was treated with glow discharge argon oxygen plasma at a pressure of $5 \cdot 10^{-4}$ mbar [28, 29, 31, 147, 148]. Thus, moth eye structures were generated on the surface which served as an antireflective layer. After 300 to 400 s, fibrillar structures with depths of about 200 to 500 nm were formed which show a homogenous distribution with uniform size (fig. 21a). After oxygen plasma treatment the surface showed hydrophilic behaviour. Subsequent coating of the surface with organic fluorine compounds achieved superhydrophobic behaviour [29]. By transferring the technique to other polymers nanofibrillar structures

on the surface of Polycarbonate, Polyamide, PET, Polyolefin, and Tri-acetyl cellulose could be generated [149]. The authors proposed the following theory about nano structure formation: Chemical modification of PMMA caused by plasma emissions could play an important role in forming a self-organized etching mask that promoted these deep structures. To improve nanostructure generation, artificial etching masks were created. Thin layers between 0.5 and 2.5 nm were deposited by electron beam deposition followed by an etching step. It was found that different dielectric materials worked well as an initial layer whereas metallic layers did not show a useful effect. The authors assumed that the deposited material grew as a non-continuous film forming island. Another possibility was that the continuous initial layer dispersed into pieces during the plasma treatment caused by the much higher thermal expansion of the substrate compared with that of the initial layer material. Thus, mask formation could take place when the sample was heated by the plasma. However, both ideas could not be proved up to now. AFM images did not indicate an island growth.

Plasma etching of PMMA was also performed in a rf plasma using 2000 W, 0.0075 mbar, 100 sccm oxygen and 10°C [150]. This treatment generated nanostructures on the surface with high aspect ratio topography (fig. 21b). In a second step, the gas chemistry was altered into a fluorocarbon one which led to the deposition of a Teflon like surface layer. Thus, surface chemistry was changed and a superhydrophobic surface could be fabricated.

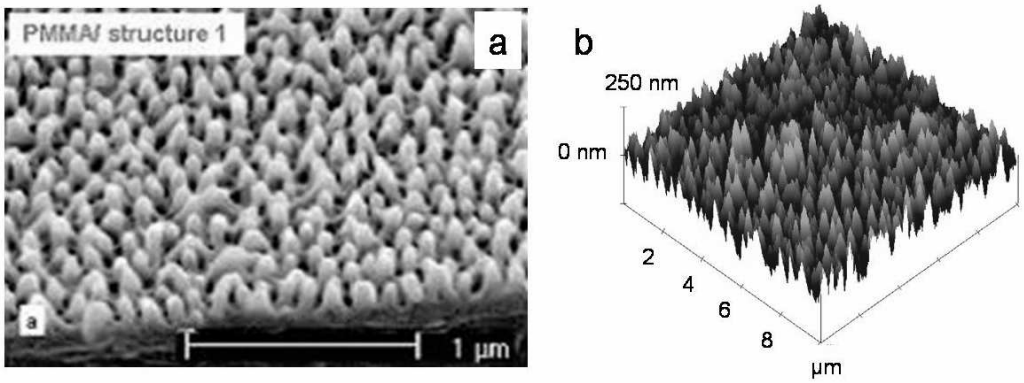

Figure 21: Nanostructures in PMMA after a) 3 min of O_2/Ar plasma (SEM image) (reprinted from [31] with permission of the Optical Society of America), b) 2 min of oxygen plasma (AFM image). (Reprinted from [150] with permission from IOP Publishing Ltd.)

Poly(tetrafluoroethylene) (PTFE) was plasma etched with oxygen (13.56 MHz, 100W, 0.02 mbar) to analyse the wetting behaviour as a function of plasma treatment time [35, 36]. The resulting surface was described as spongelike by the authors (fig. 22a). Another group performed a similar treatment in a different plasma chamber (13.56 MHz, 200W, 0.02 mbar) and generated needlelike micro structures (fig. 22b) [37, 151]. By grafting a mixture of different polymer brushes onto the needles a two-level structure was fabricated. By exposing the surface to solvents that are selective to one of the components of the brush, the surface properties (e.g. wettability, adhesion) could be tuned reversibly. Plasma treatment of PTFE with different gases was used to improve the bonding properties. By applying argon plasma a honeycomb structure was generated, in air plasma nanostructures described by the authors as stone forest were observed, and oxygen plasma treatment (13.56 MHz, 30-500 W, $4.5 \cdot 10^{-3}$ mbar, 1-60 min) resulted in high aspect ratio protrusions (fig. 22c) [152].

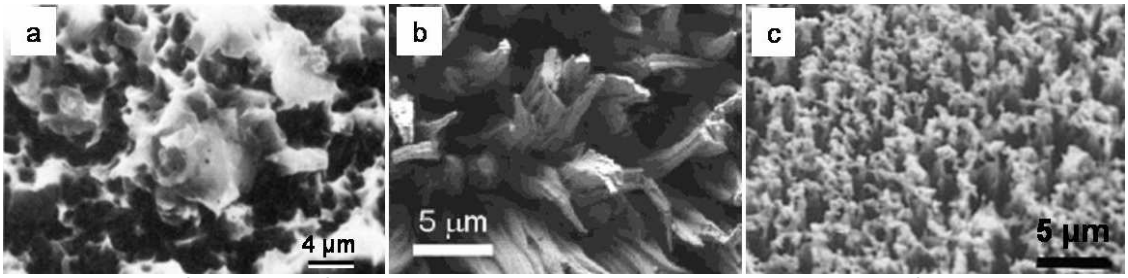

Fig. 22: PTFE after 10 min of oxygen plasma etching generated a) a sponge-like surface (Reprinted with permission from [36]. Copyright 1989 American Chemical Society.), b) a needle-like microstructure (Reprinted with permission from [37]. Copyright 2003 American Chemical Society.) c) PTFE after 5 min oxygen etching at 200 W. (Reprinted from ref. [152], Copyright 2000 Maney Publishing.)

Using microfabrication methods and a two step plasma etch process, nanofibrils on platforms were generated [153-155]. First, the BOSCH process was applied to build 2 µm thick and 100 to 150 µm long quadratic silicon platforms. The platforms were supported by single silicon pillars which were up to 50 µm in height and down to 1 µm in diameter (fig. 23a). Afterwards a photoresist layer (Shipley SPR 220-7) was coated. Placing the sample for 5 minutes into an inductively coupled oxygen plasma with a power of 100 W resulted in generation of fibrillar structures which were 2 µm long and about 200 nm in diameter (fig. 23b and c). The fibrils were not freestanding but condensated. This was probably caused by the high aspect ratio.

The generation mechanism of the fibrils was explained by electrohydrodynamic instabilities of polymer films in an electrical field according to Schäffer et al. [124, 125]. The authors assumed that the electric field gradient exceeded the surface tension of the polymer and created surface undulations which transformed into the fibrils. Additionally, the oxygen plasma broke C-H bonds at the surface and generated dangling –OH bonds which reduced the surface tension of the photoresist. Thus, fibril formation was accelerated [153]. However, a theoretical understanding of the fibril formation process is still lacking. Adhesion tests with fibrils coated on the silicon platforms showed an increase in adhesion compared to fibrils on solid substrates. However, the absolute adhesion values are very low. Changing the fibril surface from hydrophilic (contact angle 42.5°) to hydrophobic (145°) using a CF_4 plasma for 30 s, which created a fluorocarbon coating, led to a further increase in adhesion. Since the fibril size increased due to the coating to about 350 nm, the increase in adhesion could be explained with a bigger contact area.

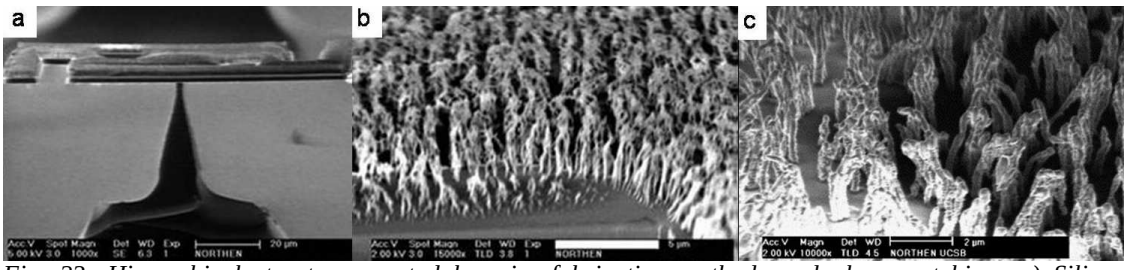

Fig. 23: Hierarchical structure created by microfabrication methods and plasma etching: a) Silicon platform supported by a pillar. b) and c) Nanofibrils were generated on top of the pillars using different plasma conditions. (a) and b) reprinted from [153] with permission from IOP Publishing Ltd. c) Reprinted from ref. [154], copyright 2006, with permission from Elsevier.)

Polymer nanowires and ring patterns on the following polymer films were generated by reactive ion etching with a mixture of argon, oxygen and CF_4 (fig. 24) [156]: Poly(methylmethacrylate) (PMMA) , PS (polystyrene), 1-methoxy-2-propylacetate (SU8), polyvinylidene difluoride (PVDF), (poly(3,4-ethylenedioxythiophene) poly(styrenesulfonate) (PEDOT:PSS), polypyrrole (PPY), and poly(2-methoxy-5-(20-ethylhexyloxy)-1,4-phenylenevinylene) (MEH-PPV). According to the authors, the structures emerged only on roughened surfaces. Roughening occured by scratching (e.g. with a needle) or by stamping/touching a copper TEM grid on a uniform PS film and then

peeling it off. Generation of the polymer-nanowires is explained with the Bradley-Harper model [157]. Here, the local sputtering yield depends on surface curvature. This leads in uneven surfaces to larger sputtering yields at the bottom of valleys than on top of hills which results in a ripple topography. From surface protrusions either polymer nano wires or tubes are generated due to ion bombardment in a reactive ion etcher. In contradiction, at the beginning of the paper the authors showed a Si wafer covered completely with the polymer nanowires but no roughening was mentioned.

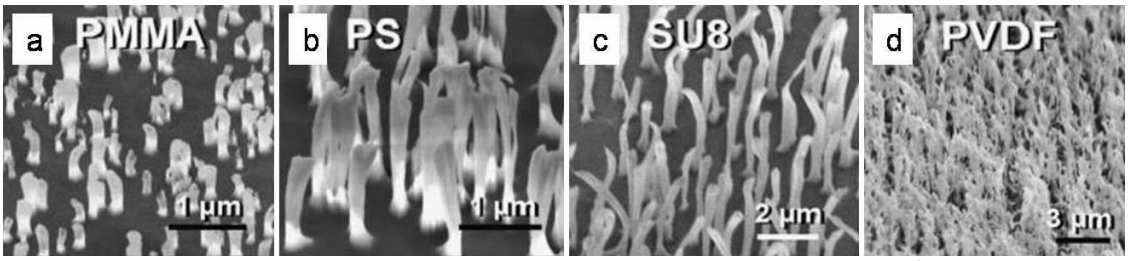

Figure 24: Polymer nanowires generated by reactive ion etching with a combination of CF_4, O_2, and Ar on a) PMMA, b) PS, c) SU8, and d) PVDF. ([156]. Copyright Wiley-VCH Verlag GmbH & Co KGaA. Reproduced with permission.)

Using CF_4/O_2 plasma nanostructures with a fibrillar shape in Polystyrene (PS) were generated (13.56 MHz, 60 sccm CF_4 and O_2, 0.78 mbar, 50 – 300 W). Increase in treatment time as well as increasing power increased height but decreased density of the resulting structures [158].

2.5.3 Filled polymers

PDMS is an amorphous polymer, which always contains silica filler particles. Therefore, it is classified as filled polymer.

Oxygen plasma treatment of PDMS led to wavy structures [40-42, 159, 160]. The surface of PDMS was oxidised and a silica-like layer was generated. Plasma treatment increased sample temperature. As PDMS and the silica-like layer have different heat expansion, after plasma treatment the silica-like layer was wrinkled due to different thermal shrinkage [42]. Plasma treatment generated wrinkles with a well-defined wave length

which could be tuned by film thickness (depends on plasma intensity and treatment time) (see also chapter 2.2 where controlled wrinkling is described as patterning method).

Fluorine-based plasma treatment at a frequency of 13.56 MHz, however, created nanofibrillar structures. Etching silicon elastomer with CF_4 or SF_6 plasmas generated fibril like nanostructures on the surface (fig. 25) [45-48, 161-166]. A subsequent treatment with Ar plasma created stable free radicals at the polymer surface which accelerates the fluorination [163-165] but the nanostructures obtained looked similar. After CF_4 plasma treatment, the resulting nanostructured surfaces were antiadhesive and superhydrophobic.

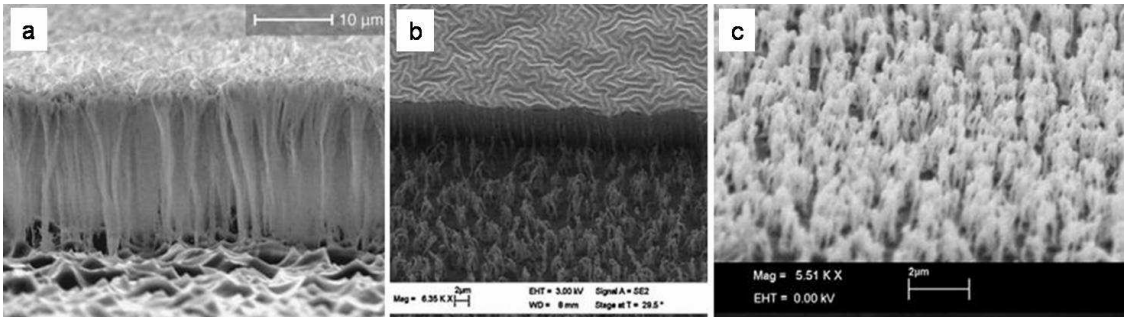

Fig. 25: PDMS surface after fluorine-based plasma treatment. a) Columnar layer after CF_4 + O_2 plasma treatment. (Reprinted from ref. [47], copyright 2006, with permission from Elsevier.) b) Fibril like structures after SF_6 plasma treatment ([46]. Copyright Wiley-VCH Verlag GmbH & Co. KGaA. Reproduced with permission.) c) Nanofibres generated by 6 minutes SF_6 treatment. (Reproduced from ref. [162] with permission from IOP Publishing Ltd.)

Structure formation was explained by preferential etching of certain components of the polymeric material in the plasma. PDMS contains organic methyl groups attached on an inorganic siloxane backbone. These organic groups are expected to etch much more quickly than their inorganic etch-resistant counterparts, which contribute to the formation of non-volatile products on etched surfaces and thus behave as masking materials to etching. Those parts of the surface that are covered by inorganic polymer components are etched much more slowly than the organic parts. Anisotropic etching leads to the formation of columnar structures. Additionally, deposition from of sputtered material from the reactor walls cannot be excluded which may contribute to preferential surface etching [45, 162]. The columnar structures were not created by silica fillers in PDMS because the same topography was generated in PDMS containing no fillers [162]. Surface

topography could be influenced by proper choice of solvent and subsequent spin coating. Column spacing was varied for 50 % and rms roughness for 30 % [166].

In table 4, all papers using plasma structuring are summarized. Depending on plasma treatment conditions and polymer parameters, different nano and microstructures were generated. All these structured surfaces have been studied in terms of their resulting adhesion, superhydrophobicity or antireflecting properties, but no attempts to study or control the mechanisms of surface structure formation have been made. It is not understood how plasma and material related parameters influence the nanostructure generation.

Tab. 4: Literature overview of plasma structuring of polymer surfaces.

Polymer	**Morphology**	**Plasma conditions**						**Structure**	**Reference**
		Gas	**Frequency**	**Pressure**	**Bias voltage**	**Power**	**Time**		
				[mbar]	[V]	[W]	[min]		
PET	Crystalline (50%)	Oxygen	13.56 MHz	0.04	200	200	5-20	Grains, 50 nm in height and width	[142]
PET	Crystalline (50%)	Argon	13.56 MHz	0.04	200	200	5-20	Grains, 50 nm in height and width	[142]
PET (Thermanox)	Crystalline	25% O_2, 75% Ar	high frequency	0.013			7.5	Peaks ≈ 50 nm in height	[143]
PET (Thermanox)	Crystalline	Oxygen	30 kHz	0.18		50	0.17 - 0	Fibrils, 65-100 nm length, 20 nm diameter (after 10 min)	[24]
PET	Crystalline	Argon, nitrogen	30 kHz	0.18		50	0.17 - 30	Protrusions, diameter 10-20 nm and 20-40 nm, respectively, after 10 min	[24]
PET	Crystalline	oxygen	13.56 MHz	0.05		100	10	Protrusions, height greater than 10 nm	[144-146]
PMMA	Amorphous	Ar + O_2	DC	10^{-4}	70-150		3.3 – 6.6	Fibrils	[28, 29, 147, 167]
Polycarbonate Makrolon)	Crystalline	Ar + O_2	DC	≈10^{-4}	70-150			Fibrils	[31, 168]
Tri-acetyl Cellulose	Crystalline	Ar + O_2	DC	≈10^{-4}	70-150			Fibrils	[31, 168]
Polyamide (Trogamid)	Crystalline	Ar + O_2	DC	≈10^{-4}	70-150			Fibrils	[31, 168]
PET (Teonex)	Crystalline	Ar + O_2	DC	≈10^{-4}	70-150			Fibrils	[31, 168]
Cycloolefine (Zeonex)	Amorphous	Ar + O_2	DC	≈10^{-4}	70-150			Fibrils	[31, 168]
PDMS	Amorphous, filled	Oxygen	13.56 MHz	0.013		400	0.5 -10	Wavy structures, amplitude and periodicity 50-300 nm	[40, 41, 159, 160]
PDMS	Amorphous, unfilled + filled with silica particles	SF_6	13.56 MHz	0.013	-100	1900	1-15	Columnar-like structures, length: few hundred nm - 6 µm	[162]

PDMS	Amorphous, filled with silica particles	$CF_4 + O_2$	13.56 MHz	0.2		150	60	Fibrils; height 1,8 µm, average diameter 235 nm	[48]
PDMS	Amorphous, filled with silica particles	CF_4 (subsequent Ar plasma)	13.56 MHz	0.026		200		Columnar-like micro structures	[165]
PDMS	Amorphous, filled with silica particles	CF_4 (subsequent Ar plasma)	13.56 MHz	0.052		150		Submicron features	[164]
PDMS	Amorphous, filled with silica particles	Oxygen						Wavy structures, wavelength between several 100 nm and 1 µm	[42, 43]
PMMA	Amorphous	Oxygen	13.56 MHz	0.0075	-100	2000	1-5	Nano-needles (1 min), HAR pyramid-like structures (2 and 5 min)	[150]
Cellulose	Crystalline	Oxygen	13.56 MHz	0.13		150	30	nm scaled features with fibril-like shape	[22]
PTFE	Amorphous	Oxygen	13.56 MHz	0.02		100	1 - 15	Spongelike structures	[35, 36]
PTFE	Amorphous	Oxygen	13.56 MHz	0.02	≈ 1000	200	10	Needles, diameter ≈ 1µm, more than 5 µm	[37]
PE	Crystalline	Argon	13.56 MHz			100	0 - 240	Short and branched walls	[33]
PS	Amorphous	CF_4/O_2	13.56 MHz	0.08		50-300	0.5 - 20	Nanotexture, at longer treatment times fibrillar shape	[158]
Shipley SPR 220-7	Amorphous	Oxygen	13.56 MHz			100	5	Organic nanorods, fibrils diameter 200 nm, length 2 µm	[153-155]
PMMA, SU8, PS, PEDOT, PPY, PVDF, MEH-PPV		Mixture of Argon, Oxygen and CF_4	13.5 MHz	0.013		100		Nano wires and nano tubes, diameter ≈ 400 nm, length ≈ 2 µm	[156]

2.6 Surface wettability

When a drop of liquid is placed on a solid surface, either it remains as a drop of finite area or it spreads indefinitely over the surface. The contact angle depends on several factors like surface energy, roughness, the manner of surface preparation, and surface cleanness. On a flat and smooth solid surface the equilibrium angle of contact θ_e is determined by the Young equation [169]:

$$\gamma_{sv} - \gamma_{sl} = \gamma_{lv} \cos\theta_e \qquad (4)$$

Here γ_{sv}, γ_{sl} and γ_{lv} are the interfacial free energies per unit area for the solid-vapour, solid-liquid and liquid-vapour interfaces (fig. 26).

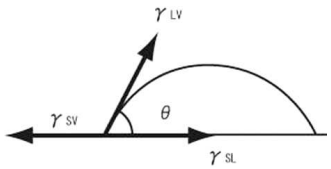

Fig. 26: A drop of liquid on a solid surface provides three different interfacial free energies per unit area for the solid-vapour (sv), solid-liquid (sl) and liquid-vapour (lv) interfaces.

On rough surfaces, the liquid can either fill up the grooves or drops settle on the peaks of the roughness geometry leaving unfilled grooves. In Wenzel's approach of a wetted contact the apparent contact angle θ^W is given by

$$\cos\theta^W = r\cos\theta_e \qquad (5)$$

where r is the ratio of the true area of liquid-solid contact to the projected area and θ_e is the equilibrium contact angle of the liquid drop on the flat surface [170]. According to Wenzel's equation, surface roughness further decreases the contact angle if the contact angle is < 90°, whereas contact angle further increases if θ_e > 90°.

If drops settle on the peaks of the roughness geometry, air is trapped into the grooves under the droplet. Here, the droplet is in contact with a composite surface (solid and air), which is attributed to the Cassie-Baxter model [171]. The apparent contact angle θ^{CB} can be calculated as:

$$\cos\theta^{CB} = \varphi_s \cos\theta_s + \varphi_{air} \cos\theta_{air} \quad (6)$$

By considering the air area fraction as $\varphi_{air} = 1 - \varphi_s$, $\theta_{air} = \pi$, and assuming that the water contact angle of the solid fraction, θ_s, corresponds to that of the flat surface, θ_e, the equation can written as:

$$\cos\theta^{CB} = \varphi_s \cos\theta_e - (1 - \varphi_s) \quad (7)$$

with φ_s is the area fraction of the liquid-solid contact. For water, a wettable surface ($\theta_e <$ 90°) may also be termed hydrophilic and a non-wettable surface hydrophobic ($\theta_e >$ 90°). A combination of hydrophilicity and surface roughness can lead to superhydrophobic surfaces with contact angles greater than 150°. Here, water droplets show almost no contact to the surface.

Besides the water contact angle the water contact angle hysteresis has to be considered. The water contact angle hysteresis is defined as the difference between the advancing contact angle (while a droplet is increasing its volume) and the receding contact angle (droplet is decreasing its volume) measured in a dynamic mode on a horizontal plane. Differences originate by the presence of surface roughness or chemical inhomogeneities which induce fluctuations in surface tension [169]. A drop on a tilted plane exhibits a larger contact angle at the front than at the rear. Front and rear contact angles are generally considered equal to the advancing and receding contact angles. The difference generates a force opposing the weight of the drop. If the drop is small enough this force will be able to balance it. The drop will stick to the surface if the water contact angle hysteresis is high while a drop can slip down the surface when it is low. Since hysteresis originates from defects, a high water contact angle hysteresis is expected for all rough

surfaces. A completely wetted rough surface (Wenzel's approach) shows a high water contact angle hysteresis because the surface structures act as obstacles to water motion and make drops stable on the surface. If the surface is partial wetted (Cassie-Baxter's approach) water drops touch only the top surface and therefore, the structures cannot hinder water motion. The lower the contact with the surface (φ_s), the lower is the water contact angle hysteresis and the less stable is the drop and it can move over the surface. This is sometimes referred to as the "lotus effect" [56].

2.7 Adhesion

Adhesion is an attraction between two substances which, after they have been brought together, requires work to be done to separate them [172]. Different attractive forces are responsible for adhesion, e.g. van-der-Waals forces, electrostatic forces, and capillary forces.

Van-der-Waals forces are caused by fluctuations of charge density in the electron shell. Instantaneous dipole moments cause dipole moments in neighbouring atoms, which interact with each other and lead to attraction forces. Van-der-Waals forces occur in all atoms and molecules and thus, between all macroscopic bodies. The van-der-Waals energy E_{VdW} between to atoms is

$$E_{VdW} \propto d^{-6} \tag{8}$$

where d is the distance of the atoms [173]. By integration of all interactions between atoms in a macroscopic body, the van-der-Waals energy between two macroscopic bodies can be calculated. The van-der-Waals force between a flat surface and a sphere is given by:

$$F_{VdW} = \frac{H \cdot R}{6d^2} \tag{9}$$

with radius R of the sphere, Hamaker constant H, and distance d between flat surface and sphere. The Hamaker constant reflects the strength of the van-der-Waals interaction for two bodies in a third medium at a temperature T. A negative Hamaker constant means a repulsive van-der-Waals force.

Electrostatic forces are caused by charges. If the charges have the same sign, the forces are repulsive, and attractive if the charges have the opposite sign. The force of two spherical charges q_1 and q_2 at a distance d is defined as:

$$F_{el} = \frac{k|q_1 \cdot q_2|}{d^2} \tag{10}$$

where k is an experimentally determined constant called Coulomb constant [174].

Capillary forces appear only when a liquid phase is present (fig. 27). This liquid phase can be water or an organic liquid. The liquid should wet the surfaces and be present at the contact area of the two contacting bodies. Due to the Laplace pressure of curved menisci between and around two adhering surfaces, capillary forces emerge. The Laplace pressure inside a liquid is given by:

$$\Delta p = \gamma_{lv}\left(\frac{1}{r_1} + \frac{1}{r_2}\right) \tag{11}$$

where γ_{lv} is the liquid-vapour surface tension, r_1 and r_2 are the principal radii of surface curvature of the meniscus (fig. 26). The capillary force between a flat surface and a sphere can be calculated using following simplification, $r_1 << r_2$, and contact angle on both bodies is similar ($\theta_1 = \theta_2 = \theta$), and simple geometrical correlations [175]:

$$F_{cap} = 4\pi R\gamma_{lv}\cos\theta \tag{12}$$

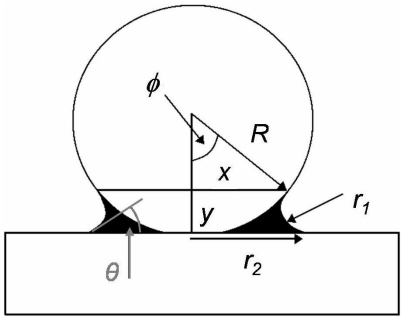

Fig. 27: Schematic capillary bridge between flat surface and sphere.

3. Aims and Objectives

This work focused on the understanding of fibril formation at the surface of PET samples upon oxidative plasma treatment. A detailed screening of plasma and material related parameters influencing the formation and dimensions of the fibrils was performed in order to clarify the potential of plasmas for controlled patterning of surfaces. The properties of the resulting surfaces in terms of wettability, adhesion and friction were also characterized. The particular objectives of the work were:

- Identification of plasma experimental conditions for obtaining freestanding fibrillar structures in PET films
- Systematic variation of the experimental parameters in order to control fibril density, diameter and length. For this purpose the type of process gas, gas pressure, power, plasma treatment time and sample temperature were varied.
- Analysis of the influence of processing conditions during film preparation (thermal and mechanical treatment) in the polymer microstructure and correlation with the observed topography after plasma treatment. Establishment of the relationship between observed topography and underlying microstructure.
- Elucidation of the mechanism of fibril formation: to what extent is differential etching of domains with different order responsible for the fibrils?
- Analysis of other polymers under similar plasma conditions to clarify the flexibility of the plasma treatment for patterning other materials.
- Study of the surface properties: wettability, adhesion and friction.

4. Experimental methods

4.1 Materials

The following polymer samples were used in this work

Tab. 5: Polymer samples

Polymer	Trade name	Company	Shape	Thickness
Poly(ethylene terephthalate), PET	Thermanox	Nunc	Film	200 µm
	Hostaphan RN 350	Mitsubishi	Film	350 µm
	Mylar A	DuPont	Film	190 µm
		Goodfellow	Film	350 µm
		Goodfellow	Fibre	100 µm
		Polysciences	Granulate	
Poly(ethylene naphthalate), PEN		Goodfellow	Film	25 µm
Poly(buthylene terephthalate), PBT		Goodfellow	Film	300 µm
Poly(tetrafluoro ethylene), PTFE	Teflon FEP	Du Pont	Film	80 µm
	Teflon PFA	Du Pont	Film	80 µm
Polyethylene, PE	UHMW PE	Goodfellow	Film	200 µm
Polystyrene, PS		Goodfellow	Film	250 µm
Poly(methyl methacrylate), PMMA		Goodfellow	Film	50 µm

Perfluorodecyltrichlorosilane was purchased from ABCR GmbH & Co. KG (Karlsruhe, Germany). Lithographic SU-8 patterned wafers were provided by L. Boesel and D. Drotlef (MPI for Metals Research, Stuttgart). Sylgard 184 prepolymer and crosslinker were purchased from Dow Corning (MI, USA). EpoFix Kit was provided by Struers (Willich, Germany). N-propylamine was purchased from Aldrich.

4.2 Equipment

Compression moulding was performed using a Collin press or a manual lab press PW 10 H (P/O/Weber, Remshalden, Germany). Hot embossing was performed on a Präzitherm PZ 20 ET precision hot stage (Gestigkeit, Düsseldorf, Germany) with a 350°C ± 1°C temperature range.

Thermal analysis of the films was performed by Differential Scanning Calometry using a DSC 822 (Mettler Toledo). Quantitative analysis of the recorded data was carried out with the software Leica QWin V3.

Uniaxial tensile tests were performed with a home-built tensile device at Instituto de Ciencia y Tecnología de Polímeros (Madrid, Spain) [176]. Wide-angle X-ray diffraction (WAXS) of the oriented fibers was performed with a Siemens flat-plate camera attached to a Phillips 2 kW tube x-ray generator using nickel-filtered Cu-Kα radiation. The orientation of the polymer chains in the uniaxial stretched samples was analyzed with the software fit 2D.

Plasma experiments were performed with a Plasma Activate Statuo 10 USB (plasma technology GmbH, Rottenburg, Germany). The characterisation of the surface topography was performed using a Hitachi S-4800 or a LEO 1530 VP (Zeiss) Scanning Electron Microscope. Samples were sputter-coated with gold-palladium using a BAL-TEC, SCD 500 Sputter Coater or carbon coated with MED 010, Balzers Union. White light interferometry was carried out with ZYGOLOT New View 5000. Transmission Electron Microscopy (TEM) characterisation was performed with a Joel 4000 EX. Cross sections for TEM analysis were cut with a Leica EM UC6 Ultramicrotome (Wetzlar, Germany) using an oscillating knife ultrasonic 35° from Diatome AG (Biel, Switzerland). A surface profilometer Dektak 8 (Veeco Instruments GmbH, Mannheim, Germany) was used for measuring the surface roughness R_a. Weight of the films was determined with the balance XP205 DeltaRange from Mettler Toledo. Contact angles of polymer films to water were measured with a Kruess Instrument, model DSA10-Mk2.

For adhesion measurements a home-built indentation apparatus was used consisting of a piezoelectric crystal (P-611 NanoCube, Physik Instrumente, Karlsruhe, Germany), a hexapod nanopositioning stage (F-206, Physik Instrumente, Karlsruhe, Germany), and a laser interferometer (SP 120, SIOS, Ilmenau, Germany) [117, 177]. Data were collected with a Labview software package.

4.3 Preparation of polymer samples

4.3.1. PET films by compression moulding

PET films with controlled thermal histories were prepared by compression moulding at 270°C and 1 kN from granulate using a manual lab press. The granulate was melted between Teflon sheets and the melt film was left at 1 kN for 3 minutes. Amorphous films were prepared by quenching the molten film in ice water. Semicrystalline films were obtained by slowly cooling the melt at 10°C/min between the plates of the press at pressure between 0.5 and 1 kN. Film thickness was in the range of 100 to 250 µm.

PET films for uniaxial stretching were obtained by compression moulding PET granulate in a hydraulic press. The granulate was first melted on the hot plate at 270°C and then a pressure of $2 \cdot 10^6$ N was applied for 1 minute. An intermediate polyimide film between the metallic plates of the press and the PET melt was used to avoid sticking of the melt to the metal plates. Amorphous PET films were obtained by placing the polyimide-sandwiched PET melt between water-cooled plates under a pressure of $2 \cdot 10^6$ N.

4.3.2 Gold-masked PET micropatterns

Thermanox films were covered by TEM copper grids and sputter coated with 20 nm AuPd (fig. 28a). The gold patterned sample was plasma treated and subsequently sputter coated with 5 nm AuPd. Small pieces with triangular shape were cut (fig. 28b) and embedded into epofix resin for ultramicrotomy and carbon coated for SEM imaging.

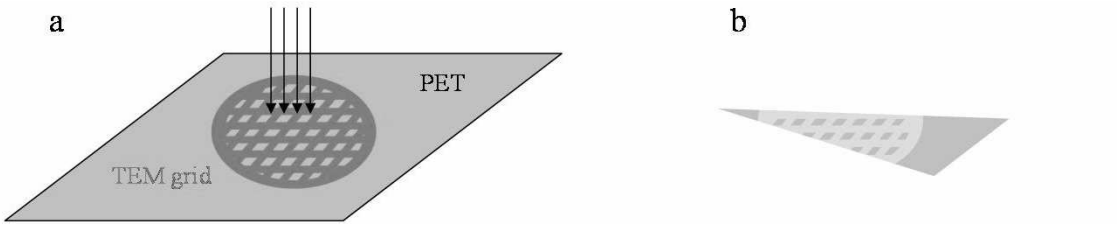

Fig. 28: a) Micro patterning of PET surface via sputter coating using TEM grids as mask. b) Cutting samples with triangular shape containing the patterned surface.

4.3.3 Microstructured PET films by soft moulding

Lithographic wafers containing holes of diameters between 2 and 50 mm and heights of 5, 10, and 20 mm were cast with a 10:1 ratio of Polydimethylsiloxane Sylgard 184 prepolymer (PDMS) and crosslinker after degassing [117]. The PDMS was cured during 14 h at 65°C in a vacuum oven (200 mbar) and peeled-off from the wafer carefully. A PDMS stamp containing holes of defined dimensions was obtained and used for soft-moulding PET films.

PET granulate was melted on a hot plate at 270°C and a tempered PDMS stamp was carefully pressed against it. The stamp was left between 3 and 30 minutes on the PET in order to allow mould filling without further pressure. Then the sample was cooled to room temperature and the PDMS stamp was carefully peeled off from the PET film. The dimensions (diameter and height) of the PET micropillars and the homogeneity of the pillar pattern were checked by white light interferometry.

4.3.4 Chemically etched PET

Thermanox samples were chemical etched by placing the sample in a Petri dish with n-propylamine at room temperature for 1 to 24 hours [178]. After etching the sample was rinsed with fresh n-propylamine and with water.

4.3.5 Uniaxial stretching of PET samples

Samples for uniaxial tensile tests were cut rectangular (width 3.43 or 6.43 mm, length 50 mm) or waisted (width 4.0 mm, length 50 mm) using a cutting die. Samples were stretched either directly or after annealing. For stretching, the samples were fixed with clamps at the tensile tester (fig. 29). The distance between the clamps was adjusted to 10 mm. Tensile tests were performed at 100°C with stretching rates between 2 – 30 mm/min. Samples which broke at the beginning of the test were discarded. After stretching, samples were removed from the device within one minute except those that recieved a post-stretching annealing at 100°C.

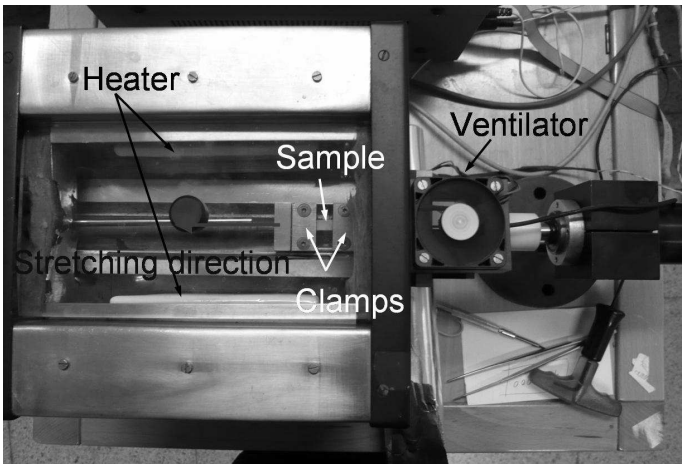

Fig. 29: Home-built uniaxial tensile tester. Rectangular sample is clamped at the ends with a distance of 10 mm between the clamps. A ventilator cares for uniform heat distribution during the tensile test.

The degree of orientation was determined from X-ray experiments (WAXS) as explained in section 4.7.2. Table 6 resumes the experimental parameters of the tensile test performed for the three selected samples discussed in following sections. The optical appearance, shape, width and length l_0 of the samples prior to stretching, as well as the stretching rate v, elongation after stretching ε, and annealing time at 100°C t_{ann} are listed.

Tab. 6: Experimental details of uniaxial tensile test

Sample	Appearance	Shape	Width [mm]	l_0 [mm]	v [mm/min]	ε [%]	t_{ann} [min]
1	transparent	rectangular	6.43	10	30	402	no
2	transparent	rectangular	3.43	10	10	400	75
3	white	waisted	4.0	30	6	240	no

4.3.6 Perfluorinated PET

The surface of PET films was perfluorinated by gas-phase silanisation using 1H,1H,2H,2H-perfluorodecyltricholorosilane in an evacuated desiccator for 2 hours. Subsequently, the films were placed in an oven at 75°C for 1 day under vacuum for improving the stability of the coating.

4.4 Plasma treatment

Fig. 30: Plasma chamber Plasma Activate Statuo 10 USB (Plasma Technology).

The plasma equipment *Plasma Activate Statuo 10 USB* is a low pressure capacitively coupled plasma reactor operating at 24 kHz, pressure between 0.05 and 1 mbar, and power between 10 and 100 W (fig. 30). The plasma chamber was initially connected to a vacuum pump 2Z-12 (Qianjing World, Wenling city, China) (free air displacement 4.55 l/s, ultimate vacuum 0.016 mbar) and later to a Duo 5M from Pfeifer (Berlin, Germany) with higher performance. The etch gas is injected in the chamber regulated with a mass

flow controller (Iq$^+$flow, Bronkhorst High-Tech BV, AK Ruurlo, Netherlands). The electrode was a perforated aluminium foil and was exchanged for some experiments by a temperature-controlled electrode. This consisted of a hollow metallic plate where tubes go through. The tubes are filled with silicon oil and connected to an external cooling thermostat that allows working at temperatures between -10°C and 80°C.

The chamber was connected to a computer that allows selection of the plasma conditions (pressure, power, and time) before the experiment. Once the sample (size was typically 22×20 mm) was placed on the electrode, the chamber was evacuated and the operator initialized the plasma when the desired vacuum has been reached. During the experiment, the real-time profiles of the pressure in the plasma chamber and temperature at the electrode were monitored.

In order to check the homogeneity of the plasma treatment across the whole electrode, we analyzed the surface structure of samples placed at different sites of the electrode. No significant difference in the surface structures was detected. Therefore, the samples were randomly positioned on the electrode in the following experiments.

For the characterisation of weight variations after plasma treatment, squares with an area of 4 cm^2 were cut from compression moulded amorphous and semicrystalline PET films. The sample was weighted before and immediately after the plasma treatment with a micro balance.

Plasma etching was also performed for polymer films that were tilted at 30°, 45°, and 60° with respect to the electrode by placing the sample on a metallic block (fig. 31).

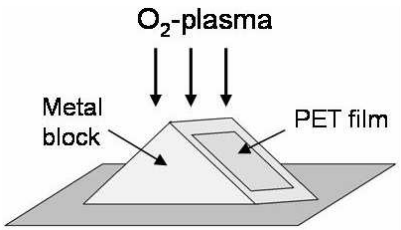

Fig. 31: Plasma treatment of tilted samples. PET film was fixed to a pyramidal metal block placed on the electrode.

4.5 Preparation of samples for electron microscopy

4.5.1 Cutting thin PET slices via ultramicrotomy

A triangular shaped piece of the PET sample was embedded into an epoxy matrix, and then trimmed to generate a pyramidal block (fig. 32a). The block was clamped in the ultramicrotome and thin slices were cut with an oscillating knife with 0.6 mm/s (fig. 32b). Slices with a thickness of 70 – 100 nm were obtained. They were connected at one point forming a band that slipped into a water basin which was attached behind the diamond knife. Then the slices were caught from the water bath using a TEM copper grid (fig. 32c).

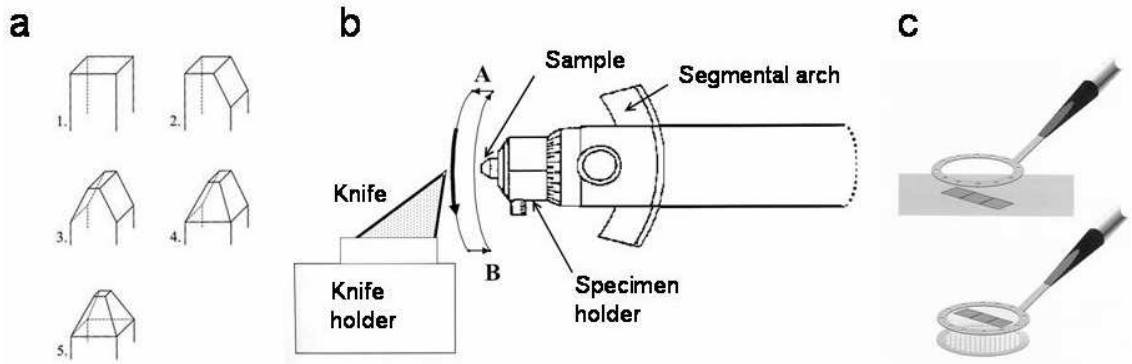

Fig. 32: Sample preparation for TEM: a) Trimming of the embedded sample to form a pyramidal tip shape. b) Cutting of thin slices with ultramicrotomy. c) Transfer of the sections from the water bath to a TEM grid. (Reprinted from ref. [179] with permission from Carl Hanser Verlag.)

4.5.2 Preparation of samples for SEM

Plasma treated films were placed on SEM pin stubs (Agar scientific, Essex, GB) and sputter-coated with a 5 nm thick layer of AuPd or a carbon layer.

4.5.3 Preparation samples for TEM

Cross sections of PET films obtained by ultramicrotomy were placed on copper grids. To enhance contrast between PET and embedding resin some samples were coated with AuPd prior to embedding. Some embedded and trimmed samples were stained with ruthenium tetraoxide vapour (RuO_4) for 17 hours at room temperature.

4.6 Topographical characterisation

SEM analysis was performed at 10 keV accelerating voltage. To obtain a better three dimensional impression of the features plain view as well as tilted view (30° or 45°) of every sample was taken. Different images were taken on the same samples to check the homogeneity of the surface structures. Samples containing tilted nano fibrils were analysed under 40° tilt angle. In this case, not the complete area but only the ridge of the sample was investigated to reveal the tilt angle of the structures.

Selected SEM pictures were analysed quantitatively to determine fibril diameter, fibril length, interfibril distance, fibril or fibril bundle density and size. Fibril diameter was estimated from tilted SEM pictures. Measurements were performed in the middle of 20 isolated fibrils. The distance between single fibrils or fibril bundles was measured manually in at least 20 neighbouring fibrils (random selection). Fibril length was measured from SEM pictures of cross sections. To determine the area percentage of fibrils or fibril bundles, black and white images were prepared manually for four different areas ($\geq 0.6\ \mu m^2$). These images were analysed with the software Leica QWin V3. The number of fibrils or fibril bundles were counted manually. Fibril or fibril bundle size was measured manually in at least 20 neighbouring fibrils or fibril bundles (random selection).

4.7 Characterisation of polymer morphology

4.7.1 Crystallinity

DSC measurements were performed at a scanning rate of 20 K/min (fig. 33). The melting enthalpy Δh^m was determined by integration of the melting endotherm around 250°C. In case of cold crystallinisation of amorphous samples the melting enthalpy is the sum of the enthalpies of cold crystallinisation and the melting endotherm. The degree of crystallinity of the PET samples, w_c was calculated using

$$w_c = \frac{\Delta h^m}{\Delta h_0^m} \tag{13}$$

and using literature values for the melting enthalpy of 100 % crystalline PET sample ($\Delta h_0^m = 125.6$ J/g) [180]. Crystallinity of the other polymer samples was calculated similarly. The following literature values for melting enthalpy of 100 % crystalline samples were used:

PEN: $\Delta h_0^m = 103$ J/g [181]

PBT: $\Delta h_0^m = 140$ J/g [7]

UHMW PE: $\Delta h_0^m = 295$ J/g [182]

PTFE: $\Delta h_0^m = 58.6$ J/g [180].

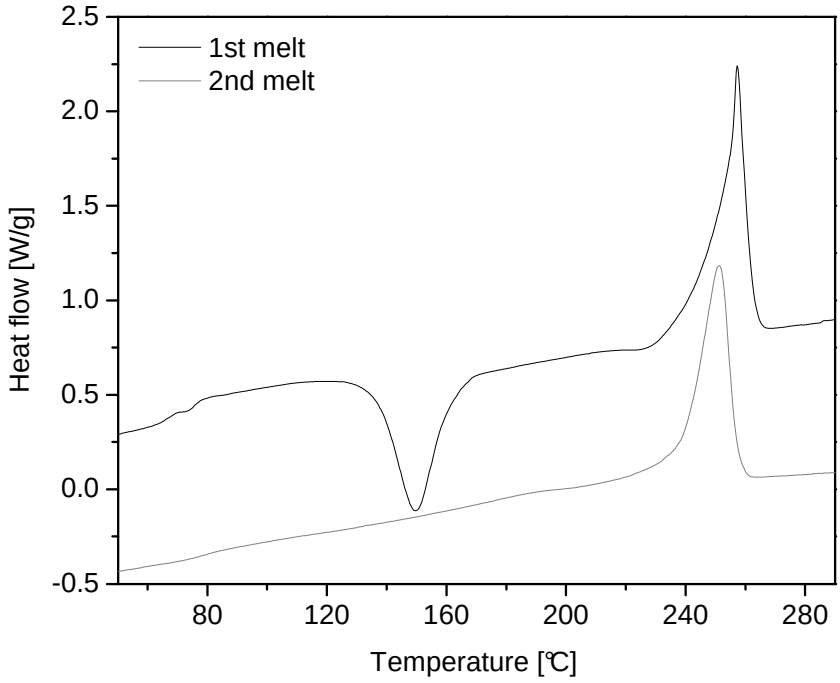

Fig. 33: Melting curve of an amorphous laboratory-made PET film (black) and melting curve of the same sample after cooling at 20 °C/min. Both ramps were run at 20°C/min. In the first melt, glass transition temperature T_g is around 75°C, cold crystallinisation occurs at about 150°C and melting is observed at about 250°C.

4.7.2 Orientation

The degree of orientation of uniaxially stretched samples was investigated by wide-angle x-ray diffraction (WAXS). Measurements were performed at the middle part of the stretched sample. WAXS diffractograms of non-oriented amorphous and semicrystalline PET films (annealed 16 hours at 150°C) were first recorded for comparison. WAXS diffractograms of uniaxially stretched samples and biaxially oriented Thermanox were then obtained. The equipment was calibrated using aluminum foil as standard.

The average degree of orientation of the polymer chains in uniaxial stretched samples can be expressed by Hermans' orientation function f determined by azimuthal integration of the x-ray diffractograms [183, 184]:

$$\langle P_2 \rangle = \frac{\left(3\langle \cos^2 \alpha \rangle - 1\right)}{2} \tag{14}$$

α is the azimuthal angle in relation to the meridian, i.e. the stretching direction. <$\cos^2 \alpha$> can be determined from the intensity distribution, I(α), as follows [183, 184]:

$$\langle \cos^2 \alpha \rangle = \frac{\int_0^{\frac{\pi}{2}} I(\alpha) \cos^2 \alpha |\sin \alpha| d\alpha}{\int_0^{\frac{\pi}{2}} I(\alpha) |\sin \alpha| d\alpha} \tag{15}$$

A perfectly uniaxially oriented sample in stretching direction will have P_2 = 1, a completely isotropic sample has P_2 = 0, and P_2 = - 0,5 for a perfectly oriented sample perpendicular to stretching direction.

4.8 Water contact angle

A 10 µL water droplet was deposited on the sample surface using a microsyringe. The drop-surface contact line was visualized with a camera and the water contact angle at the water-air surface contact point was measured with the software Drop Shape Analysis. On samples treated for longer than 10 minutes the water droplet rolled off the surface and contact angle could not be measured as described. In those cases a hanging drop from the syringe was carefully approached to the surface until contact was made. Then the syringe was removed. For each sample a minimum of 6 measurements were performed.

4.9 Characterisation of adhesion and friction properties

Load-displacement curves were obtained with a home-built indentation apparatus (fig. 34) [177]. A sapphire sphere with a diameter of 5 mm was glued to the free end of a glass spring which is mounted on a piezoelectric crystal and coupled to a hexapod nanopositioning stage. The sample was placed under the sphere, and then the sphere was pressed with a defined preload onto the sample surface. The sphere was retracted at a constant rate of 2 µm/s until pull-off occurred. The deflection of the spring was monitored using a laser interferometer and converted into force (spring constant was 308,670 N/m). Before each test the sapphire sphere was cleaned with high purity ethanol. All measurements were performed at 24°C and 22 % humidity. From the load-displacement curves, the force at the pull-off event was taken as measurement for the adhesion force. Adhesion measurements were performed on nanostructured films and flat controls.

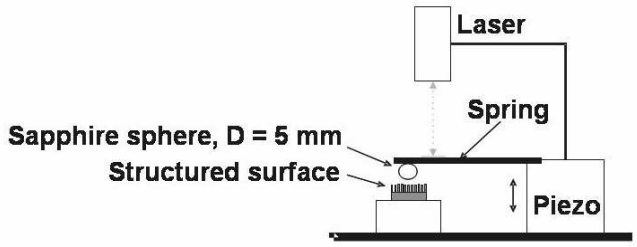

Fig. 34: Home-built indentation apparatus for adhesion measurements. Courtesy of C. Greiner.

Macroscale friction measurements were performed using a slide equipment consisting of a board with adaptable angle to the horizontal moved by an electric motor (fig. 35). The films were cut into 1 cm^2 pieces and fixed to a cubic piece of wood (weight = 1 g) with a double sided adhesive tape. In order to avoid edge effects, the edges of the piece of wood were rounded, thus the foil also exhibits a light curvature. As counter surface, polymer plates with known roughness or a glass slide were fixed to the movable board. These were positive replicas in epoxy resin (Spurr) obtained by casting negative replicas of sand

paper made of dental wax and had an average roughness as given in table 7 [185]. SEM images of selected sand papers are shown in figure 36.

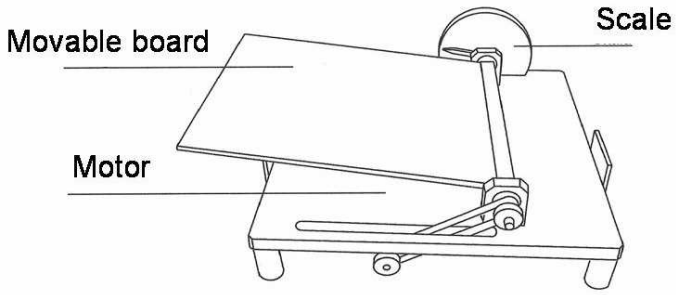

Fig. 35: Slide with a movable board on which the samples were fixed for friction measurements. Courtesy of R. Berthe [186].

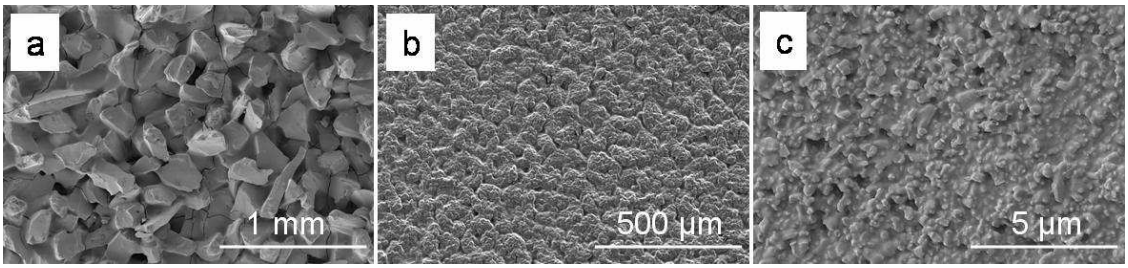

Fig. 36: SEM pictures of selected sand paper a) P100 (Struers, Copenhagen, Denmark), b) 12, and c) 0.3 (Buehler GmbH, Düsseldorf, Germany). Courtesy of C. Miksch.

During the measurement, the angle of the slide was increased at a speed of ≈ 2° per second until the sample started sliding. For each sample, the sliding angle was determined 10 times. Measurements were performed at a temperature of 24°C and a humidity of 49 %. For the measurement, plasma treated Thermanox samples under following conditions were used: 20 min oxygen plasma, 100 W, 0.1 mbar.

Tab. 7: Roughness of glass and Spurr substrates

Sample	R_a [µm]
Glass	0.0014 ± 0.0001
Spurr flat	0.033 ± 0.003
Spurr 0.3	0.083 ± 0.003
Spurr 1	0.32 ± 0.01
Spurr 3	0.99 ± 0.04
Spurr 9	2.12 ± 0.11
Spurr 12	2.52 ± 0.14
Spurr P220	8.89 ± 1.31
Spurr P100	13.94 ± 2.15

Friction experiments were also performed with films possessing tilted nanofibrils with fibrils forming 30° and 45° to the substrate (treatment conditions were 20 min oxygen plasma, 100 W, 0.1 mbar). Measurements were performed in the tilting direction (fig. 37a) and in the opposite direction (fig. 37b). Perpendicular fibres and the flat sample were tested in random directions for comparison.

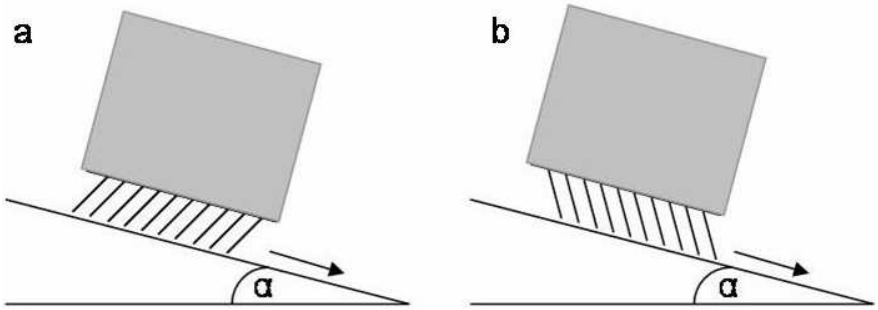

Fig. 37: Friction measurements were performed in a) the direction of the fibrils or b) against the direction of the fibrils.

5. Results

5.1 RIE Chamber and Process

The RIE chamber used for these studies contained two powered electrodes with grounded chamber walls (fig. 38). The sample was placed on the lower electrode. When the plasma was started, a sheath was formed between the bulk plasma and the materials surface due to the negative voltage on the electrode where the sample was positioned. The bias voltage depends on the gas pressure in the chamber, the applied power and the size of the electrodes and, under RIE conditions, it dropped entirely across this sheath. Positive ions entering the sheath will be accelerated towards the sample. The thickness of the sheath is less than the mean free path of the ions. Therefore, most ions do not experience collisions in the sheath and impact the surface at normal incidence. This energetic ion bombardment is expected to enhance etch rate and create directionality in the etching process.

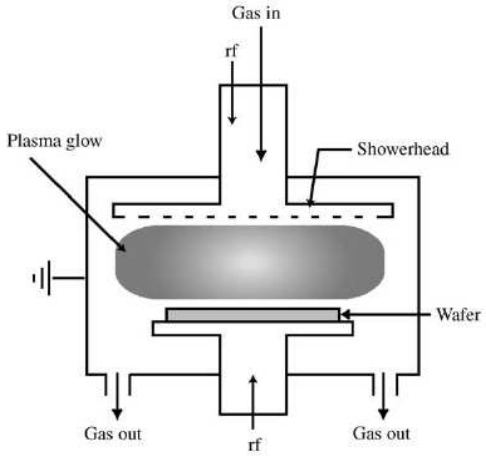

Fig. 38: Schematic of plasma chamber. (Reprinted from [141], copyright 2002, with permission from Elsevier.)

The chamber allows monitoring of the pressure in the chamber and the temperature at the electrode during the plasma experiment. Figure 39a shows a representative pressure profile. Significant variations of the pressure during the experiment were observed. Each injection of the etching gas could be detected in the pressure curve as a temporal increase of the total pressure (up to 0.25 mbar) that required about one minute to go back to the

desired value (in general 0.1 mbar). The time interval between subsequent injections was not constant and varied between the experiments. Since the pressure of the etching gas could be a relevant parameter for the plasma treatment (see section 5.2.2), attempts to improve the pressure control were performed. By connecting the plasma chamber to a pump with higher performance, a different pressure profile was observed (fig. 39b). The pressure jumps after injection were less intense and they were compensated by the pump within 15-20 seconds. This resulted in a lower average pressure and more frequent injections as compared to the other pump.

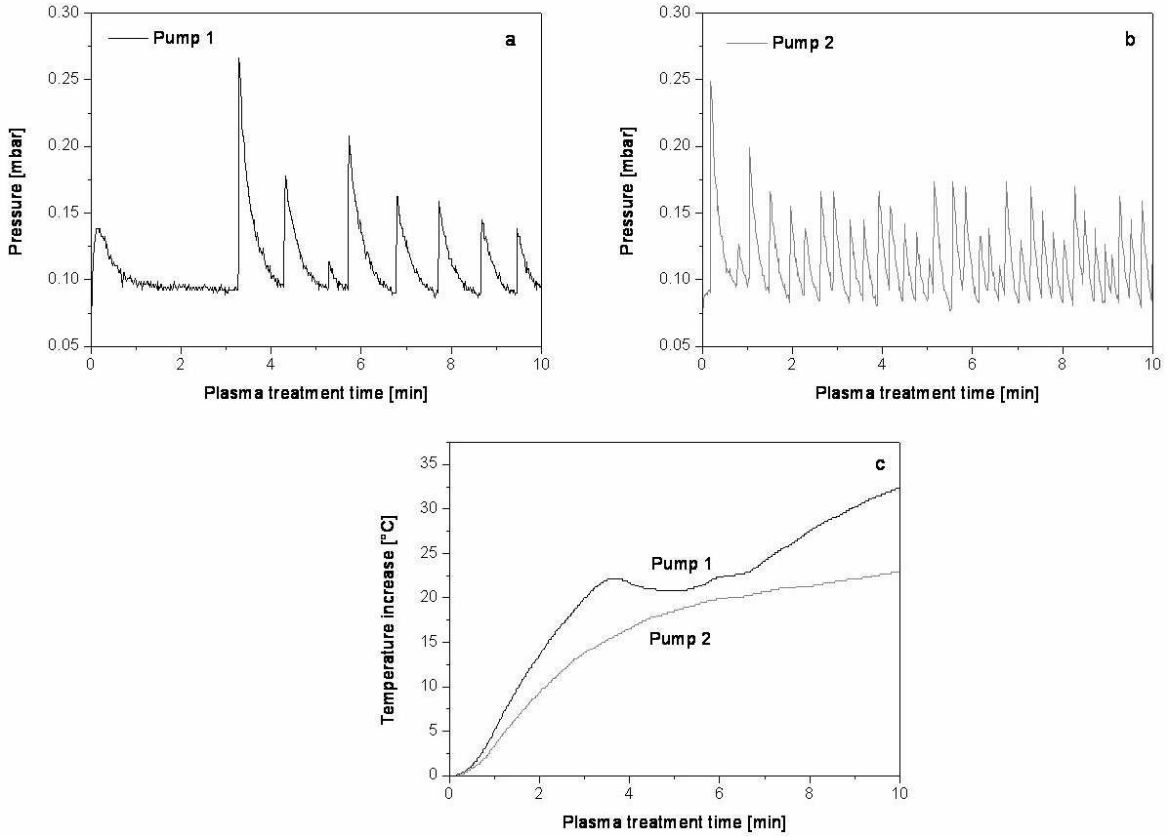

Fig. 39: a) and b) Pressure profile during oxygen plasma treatment using two different pumps. c) Corresponding electrode temperature profiles. Plasma parameters were 100 W and 0.1 mbar.

Figure 39c shows the temperature profile at the electrode corresponding to the pressure profiles in figures 39a and b. The temperature showed a rapid increase during the experiment that can be associated to the intense ion bombardment. When using the pump with the higher performance, the temperature increase is significantly decelerated after 4

to 5 minutes of experiment. The temperature profile corresponding to the pump with lower performance shows an irregular behaviour, with alternating intervals of increasing and constant temperature that correlate with the pressure jumps reflected in figure 39a. When the chamber operated at higher pressures (e.g., after large injections), the electrode temperature remained constant or even decreased. When the chamber operated at lower pressures (between 0.1 and 0.17 mbar) the electrode temperature increased with time. The overall temperature increase during the experiment was higher than with the high performance pump.

In order to improve the temperature control, the original electrode of the plasma chamber was exchanged by a metallic plate connected to a cooling/heating thermostat that pumped tempered silicone oil inside the sample stage and allowed experimentation at fixed temperatures between -10°C and 80°C (see figure 40 for schematic of sample stage). Before starting the experiment, the tempered oil was allowed to circulate through the sample stage for thermal stabilization. It was observed that the temperature measured at the sample stage (via an integrated thermocouple) never reached the programmed temperature, even after long stabilization times. Therefore, the experiments were started when the thermocouple showed a stable temperature over time, even if this was higher/lower than expected.

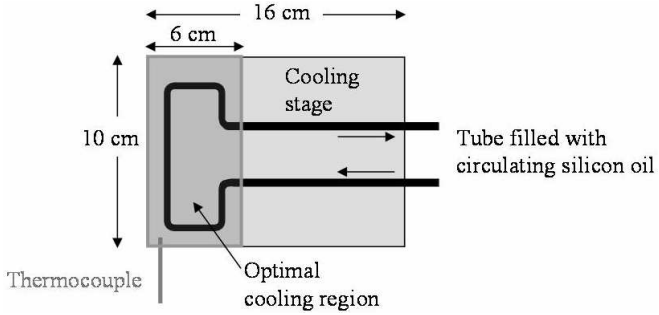

Fig. 40: Schematic of the temperature controlled electrode (cooling stage). The optimal cooling region, where the samples were placed during the experiments, is marked.

Figure 41 shows the temperature profile during experiments with programmed temperatures between -10°C and 80°C. A temperature increase of 10-20°C was observed after 10 minutes plasma treatment. The temperature increase was faster during the first 3

to 4 minutes, decelerated for longer treatment times and reached a plateau value after ca. 5 minutes. Experiments with no temperature control showed also a fast temperature increase at the beginning of the experiment and a significant deceleration after 3 to 4 minutes, but temperature continued to increase during the whole experiment and a plateau value was not achieved (inset fig. 41).

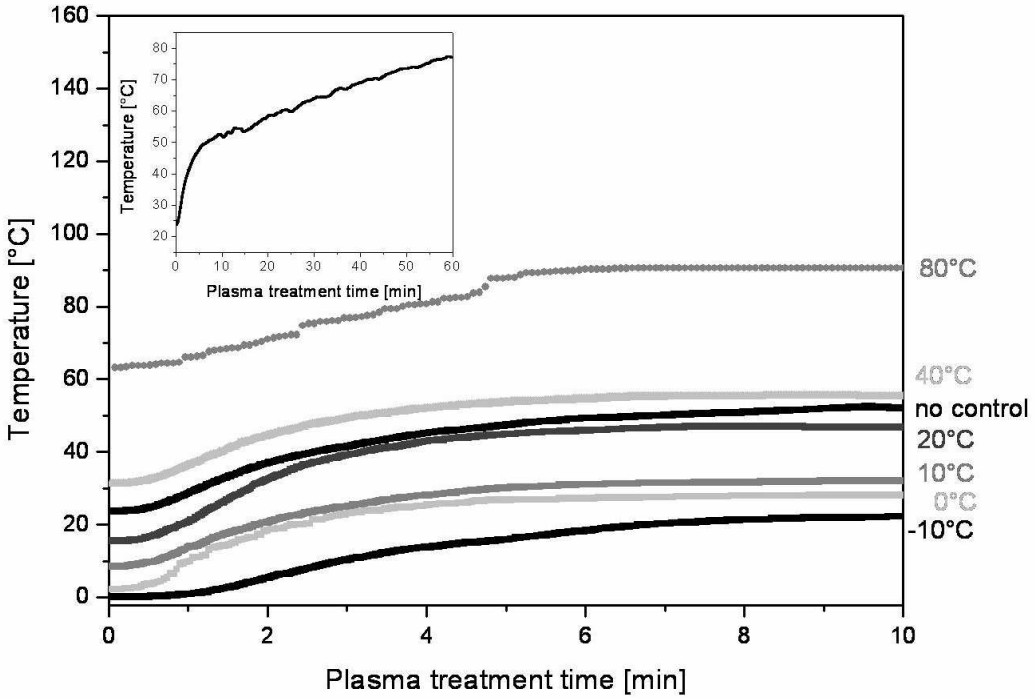

Fig. 41: Temperature variation at the electrode during oxygen plasma treatment with and without external temperature control. Plasma treatment was performed at 0.1 mbar and 100 W. Note that the measuring range of the thermocouple was between 0° and 200°C and, therefore, the curve corresponding to the experiment at -10°C can only be taken as indicative below 0°C. Inset shows temperature variation at longer treatment times without temperature control.

It is important to note that the temperature measured by the thermocouple may differ from the real temperature at the sample surface during the experiment, since the chemical and physical processes occurring during plasma treatment may provide further heating. In view of these effects, an upgrading of our machine to incorporate a thermocouple that allows separated measurements at different sites seemed crucial and was planned but could not be performed within the time framework of this thesis. The polyester-polyurethane tubes required to circulate the silicon oil inside the sample stage had severe leaking after being used for a short plasma time, presumably because of degradation

under the used RIE conditions. Unfortunately, the design of the chamber did not allow changing the tubing or installation of a temperature-controlled stage and, therefore, most experiments in this thesis were performed without cooling/heating the sample. In order to avoid continuous increase of the temperature in the chamber during a series of experiments, the chamber was left open to cool down after each treatment so that all experiments started at similar temperature.

Figure 42 shows the surface structures observed in our initial experiments using commercial PET films (Thermanox) and plasma conditions comparable to those reported in the literature (fig. 42a, b). For comparison, the flat surface structure of untreated Thermanox films is also shown (fig. 42c). A nanofibrillar topography with fibrils of different lengths was observed after plasma treatment. Long fibrils seemed to be mechanically unstable and collapse. A close similarity between the obtained and the previously reported topographies is evident (fig. 42d, e) [24]. Starting from these conditions, the next sections will present the topographical changes observed upon variation of the plasma conditions and material properties in an effort to understand the mechanism of fibrillar formation and the influencing parameters.

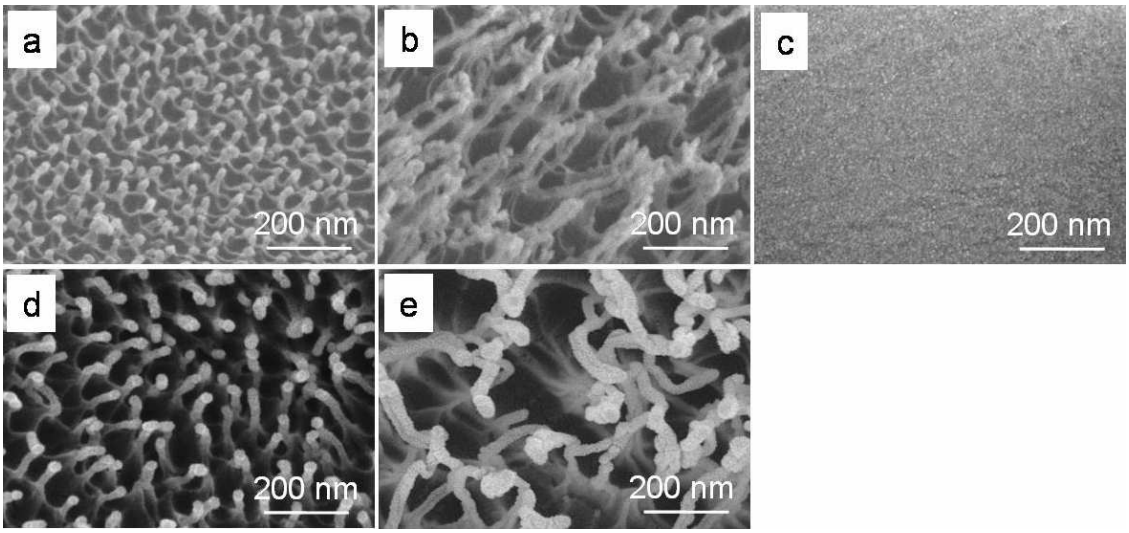

Fig. 42: SEM micrographs of PET samples (Thermanox) after oxygen plasma treatment of a) 10 minutes at 50 W and 0.1 mbar, b) 30 minutes at 100 W and 0.1 mbar, c) 0 minutes (untreated PET film), d) 10 minutes at 50 W and 0.18 mbar, and e) 30 minutes at 50 W and 0.18 mbar. (d) and e) reprinted with permission from ref. [24]. Copyright 2003 American Chemical Society.)

5.2 Surface structures under different plasma treatment conditions

5.2.1 Type of process gas

PET films were treated with gas mixtures containing oxygen in different concentrations: air, a mixture of air and pure oxygen, and pure oxygen. Air contains around 78 vol-% nitrogen, 21 vol-% oxygen, and 1 vol-% argon. The exact oxygen concentration in the air-oxygen mixture was unknown because oxygen supply was leaky. Pressure was kept constant (0.08 mbar) in all experiments.

In air, small bumps (diameter 24 ± 4 nm) at the top of poorly defined ridges formed (fig. 43a). Increasing the oxygen concentration in the process gas produced higher and better visible protrusions and ridges (fig. 43b). Processing with pure oxygen generated bundles of 3 to 5 fibrils with a diameter of 21 ± 4 nm (fig. 43c). The higher oxygen contents resulted in higher aspect ratio of the formed fibrils, which became mechanically unstable and collapsed forming bundles. Similar results were also found by other authors [24, 187]. All following experiments were performed using pure oxygen.

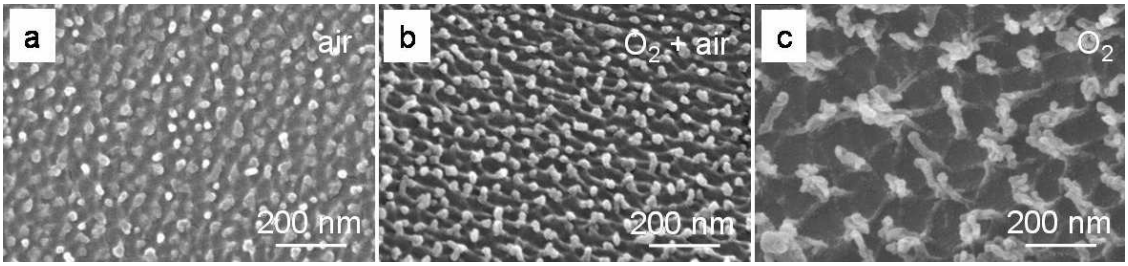

Fig. 43: SEM images of PET film (Thermanox) treated for 10 min at 100 W and 0.08 mbar with a) air, b) air mixed with pure oxygen, and c) pure oxygen.

5.2.2 Gas pressure

Experiments at oxygen pressures between 1.0 and 0.05 mbar were performed (fig. 44). 10 minutes plasma treatment at 1.0 mbar did not lead to any visible change in the surface topography (fig. 44a). On decreasing the oxygen pressure to 0.7 mbar, small bumps with 14 ± 3 nm diameter and separated by 39 ± 10 nm appeared (fig. 44b). A further decrease

in pressure resulted in higher bumps (fig. 44c). Experiments at 0.1 mbar showed isolated fibrils with a diameter 21 ± 4 nm, a length of about 200 nm (estimated from tilted SEM pictures) and separated by 81 ± 22 nm (fig. 44d). The number of the bumps or fibrils per unit area decreased as pressure decreased. At 0.05 mbar, fibrils up to 400 nm in length were observed (fig. 44e). Fibrils were bent and clumped together in bunches of 2 - 6 units. Visible ridges connecting the bumps and fibrils were found in all experiments.

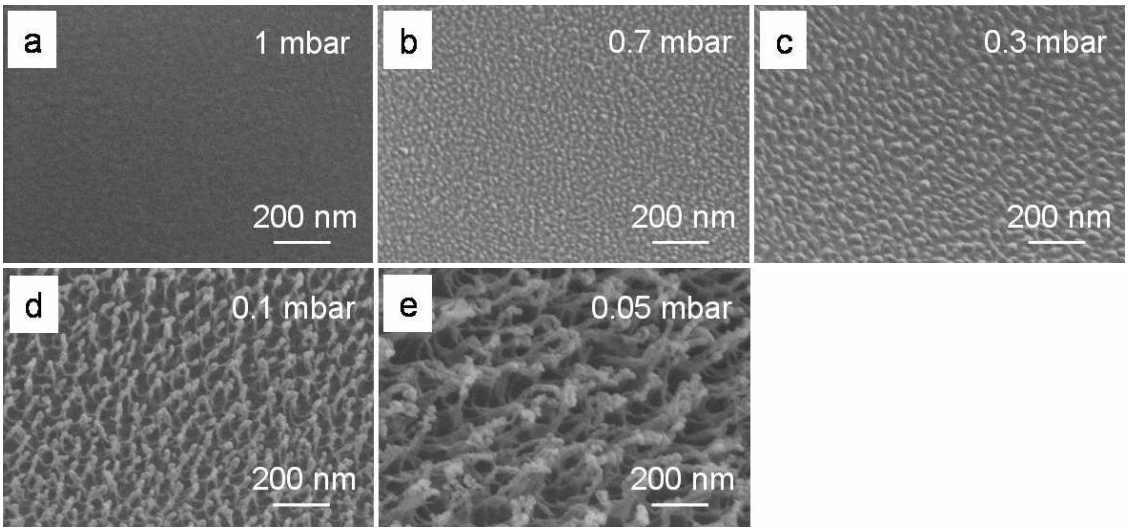

Fig. 44: SEM images of PET (Thermanox) treated 10 min at 100 W with oxygen plasma at different pressures of a) 1.0 mbar, b) 0.7 mbar, c) 0.3 mbar, d) 0.1 mbar, and e) 0.05 mbar. Samples were tilted 45° for imaging.

The effect of the oxidative plasma treatment was also evaluated by determining the weight variation of the PET film after plasma treatment. A significant weight loss occurred upon plasma treatment, indicating that the plasma caused significant etching and material loss at the surface (fig. 45a). The weight loss increased exponentially when lowering the oxygen pressure during the plasma experiment. This means that lower oxygen pressures significantly accelerated surface etching under our plasma conditions. This result agrees with the structures observed in the SEM images, where longer fibrils (indicative of higher etching depths) were found with decreasing pressure (fig. 44).

It is important to point out that increased etching resulted in longer structures, indicating that etching is directional and, therefore, physical etching caused by accelerated ion

bombardment is dominating the surface structure formation mechanism, as expected from RIE processes.

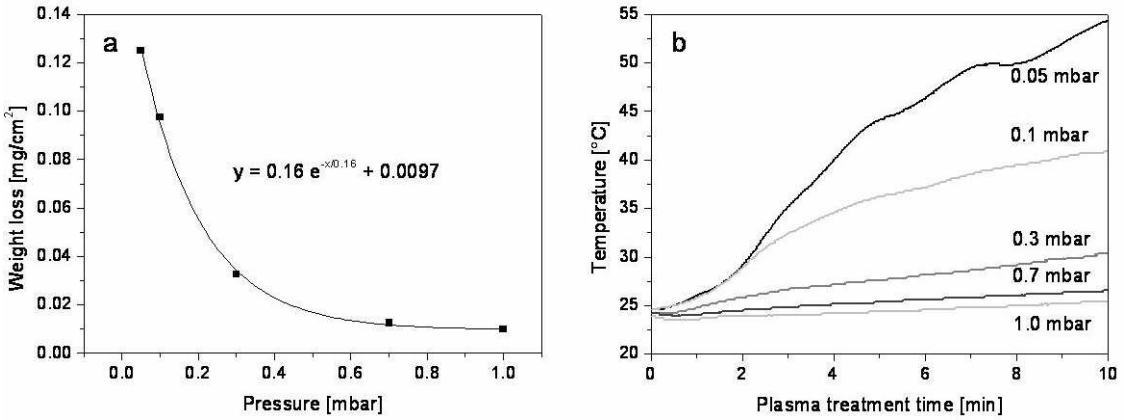

Fig. 45: a) Weight loss after 10 minutes plasma treatment of PET (Thermanox) at 100 W in dependence of different chamber pressures. b) Variation of electrode temperature when processing at different chamber pressures.

As pointed out in section 5.1, decreasing pressure during the plasma experiment enhances ion density and causes higher ion bombardment and a temperature increase at the electrode. Figure 45b shows the temperature variation observed in experiments performed at different pressures. During 10 minutes plasma treatment at pressures above 0.3 mbar, the electrode temperature increased less than 5°C, whereas the same treatment at lower pressures resulted in a temperature increase up to 30°C.

5.2.3 Power

Thermanox films were plasma treated at different powers between 20 and 100 W. Figure 46 shows SEM images representing the obtained surface topographies at three different powers. Fibrillar structures were observed in all cases. Fibril diameter (20-25 nm), length (up to 150 nm) and interfibrillar distance (42 ± 9 nm to 70 ± 22 nm) increased with increasing power. At power ≥ 40 W the long fibrils were no longer mechanically stable and collapsed forming bundles. The size of the bundles increased with plasma power (fig. 47). At 60 W bundles were composed of 3 - 4 fibrils. At 80 W and 100 W no free-

standing fibrils were found any more and up to 10 fibrils stuck together in one single bundle. The higher the power, the broader was the bundle size distribution, as depicted by the error bars in figure 46. The number of fibre bundles and fibre bundle size did not change significantly by increasing the power from 80 W to 100 W.

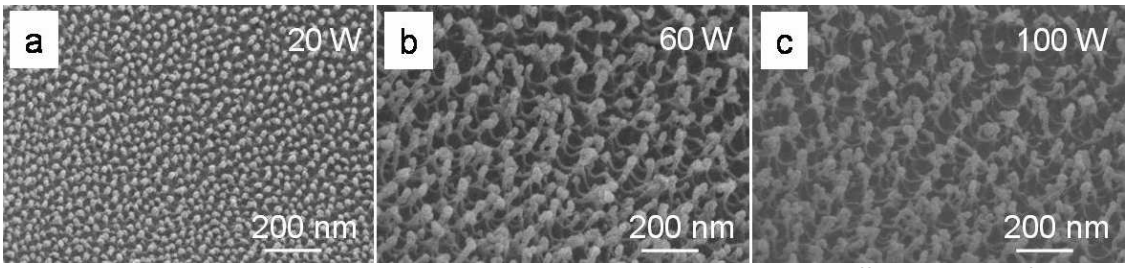

Fig. 46: PET (Thermanox) treated 10 min with oxygen plasma at 0.1 mbar and different powers of a) 20 W, b) 60 W, and c) 100 W. Samples were tilted 45° for imaging.

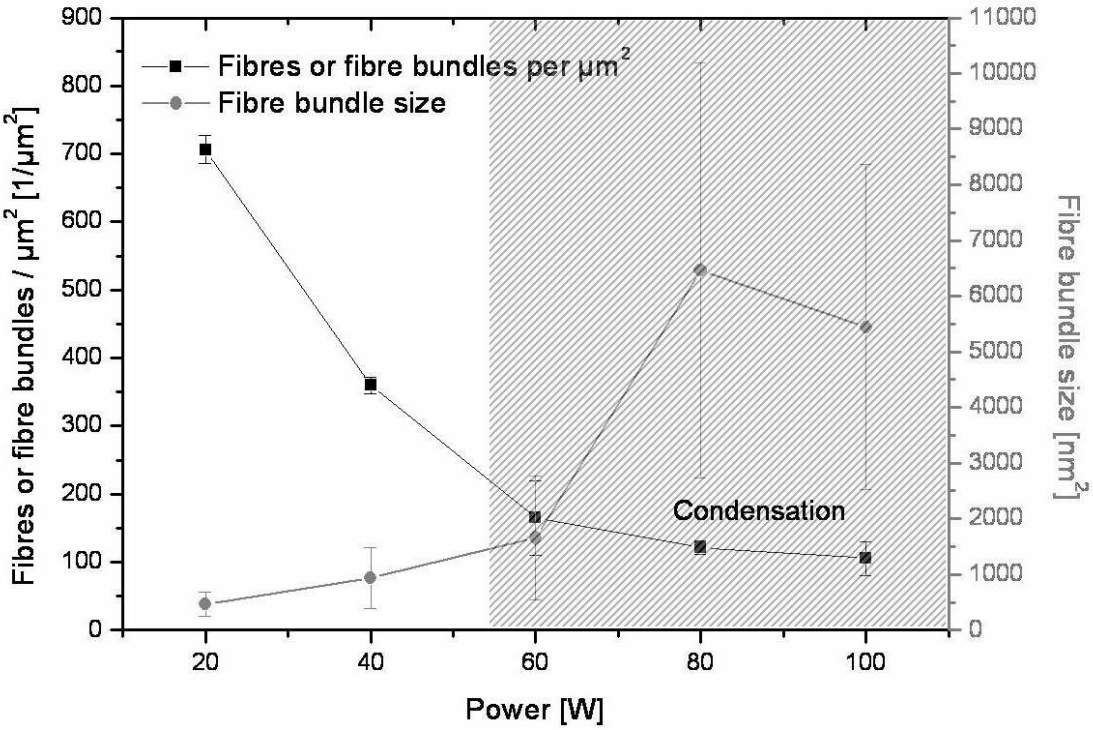

Fig. 47: Variation of the number of single fibres or bundles on the PET surface (Thermanox) with the plasma power. With higher power fibril length increased and fibrils stuck together (condensation).

The weight loss of the PET samples was measured after treatment at the different powers (fig. 48a). A linear increase of weight loss with the power was observed between 20 and 80 W. For higher powers (i.e. 100 W, which is the highest possible with our equipment)

the weight loss remained constant. These results agree with the surface features in fig. 46, where fibrils with similar dimensions were observed after treatment at 80 and 100 W.

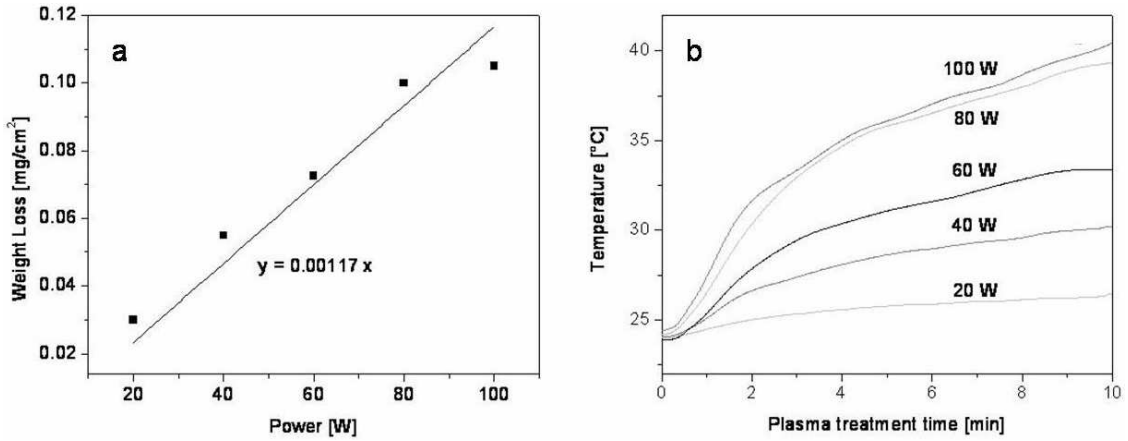

Fig. 48: a) Weight loss and b) temperature profile during plasma treatment of PET (Thermanox) at different powers.

An increase in power also affected the temperature at the electrode. Significantly higher electrode temperatures were found with increasing power (fig. 48b). Upon plasma treatment at 20 W for 10 minutes, the electrode temperature increased 4°C. A similar treatment at 80 W resulted in a temperature increase of 15°C. These temperature variations will be considered for the interpretation of our results since they may induce changes in the material that could affect the final surface morphology (see section 6.2 in discussion).

5.2.4 Plasma treatment time

Thermanox samples were treated at 100 W and 0.1 mbar with increasing times and the weight loss was determined (fig. 49). A linear increase in weight loss with increasing plasma time was detected during the first 10 minutes (0.0104 mg/cm^{2}min, which corresponds to an etching rate of 76 nm/min). Weight loss was decelerated at longer plasma treatment times. For comparison, a rate of 0.003 mg/cm^{2}min had been reported in the literature for oxidative plasma treatment of amorphous biaxially oriented PET samples using a glow discharge plasma (15 kHz, 0.067 mbar, 36 W, 1 sccm O_2) [188].

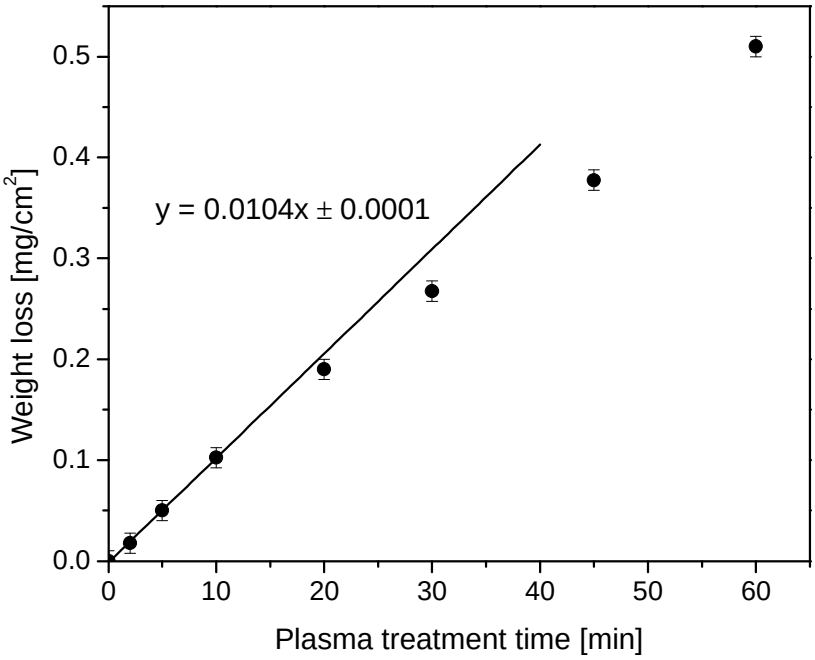

Fig. 49: Weight loss of PET (Thermanox) after plasma treatment. Samples were treated with oxygen plasma at 100 W and 0.1 mbar and were weighed immediately before and after plasma treatment.

SEM images of the Thermanox samples after different treatment times are shown in figure 50. No surface structures could be detected at times below 9 seconds. Above 9 s bumps of 15 to 20 nm diameter appeared and a superposed honeycomb structure with stretched hexagons of 400 nm length and 100 nm width became visible. The hexagonal pattern became weaker after 30 s and fainted after 50 s. The diameter of the bumps increased with plasma time and reached a diameter of about 30 nm after 60 s.

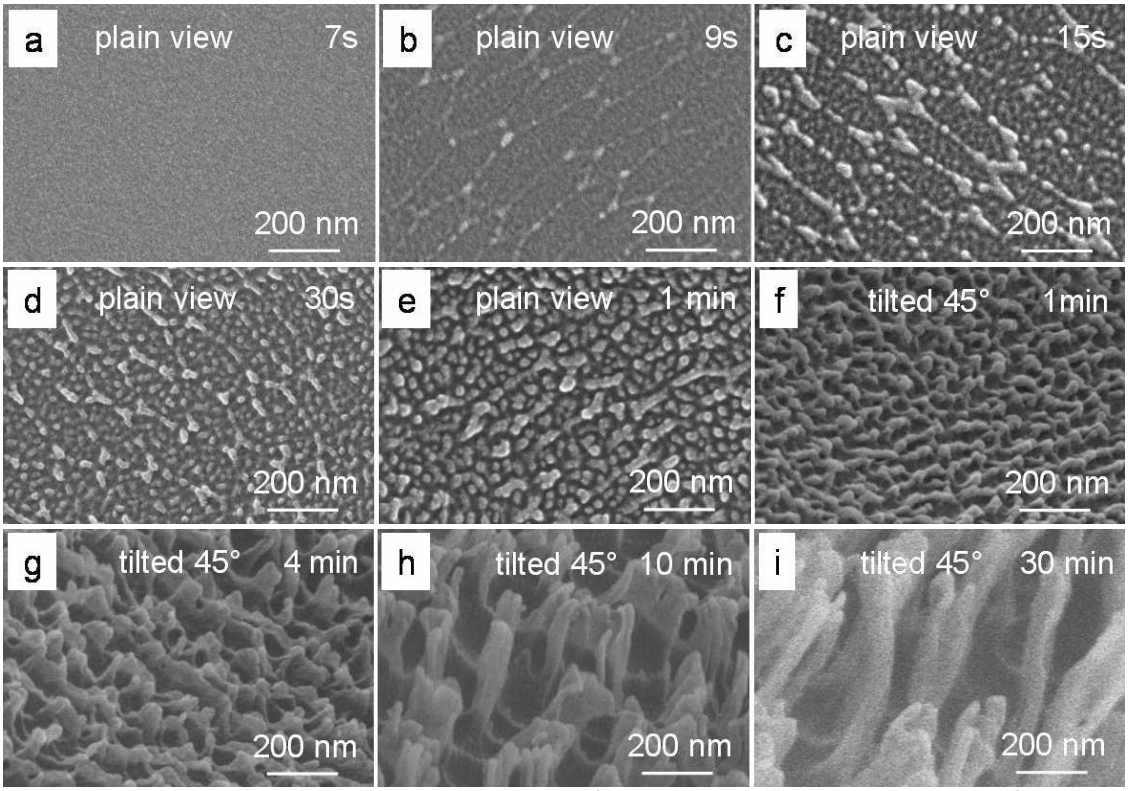

Fig. 50: PET (Thermanox) treated with oxygen plasma for a) 7 s, b) 9 s, c) 15 s, d) 30 s, e) and f) 1 min, g) 4 min, h) 10 min, and i) 30 min. Plasma parameters were 100 W and 0.1 mbar for pictures a-e (plain view), and 30 W power and 0.1 mbar for pictures f-i (tilted 45°).

Longer plasma treatment times resulted in the formation of ridges and fibrils (fig. 50f-i). Both structures became visible at the same time. Initially, high ridges decorated with small bumps appeared. Ridges were oriented in all directions. As etching proceeded, the height of the ridges between bumps decreased and the aspect ratio of the bumps increased. After 4 min, the surface structure consisted of fibrils that were interconnected at their basement by very short ridges. Longer plasma times led to longer fibrils that became mechanically unstable and condensed to form bundles. In fact, the onset for fibril condensation was observed after 4 to 6 min plasma treatment, when the aspect ratio of the fibrils approached three. After 30 minutes, fibril length increased to more than 900 nm.

The etching rate was also followed by imaging the cross section of the PET film after cutting thin slices by ultramicrotomy. In order to visualize the etching profile, a micropatterned gold-palladium layer was sputtered onto the surface prior to plasma

treatment (see section 4.3.2 for details). Gold-palladium etching rate was much slower than PET under our plasma treatment conditions and, therefore, the gold-palladium layer protected the underlying PET regions from etching. Figure 51 shows SEM images of cross-sections. After five minutes plasma treatment, fibrils could be observed at the etched regions. The top of the fibrils was at the same height as the gold layer, indicating that only material between the fibrils was removed during treatment. Increasing the plasma treatment time led to a linear increase of the etching depth (73 nm/min) and of the fibril length (30 nm/min) (fig. 52). A deceleration at longer times, as observed in the rate of weight loss may be masked because of scattering of the data and cannot be excluded. The slower increase of the fibril length indicates that single fibrils also underwent etching as plasma treatment proceeded.

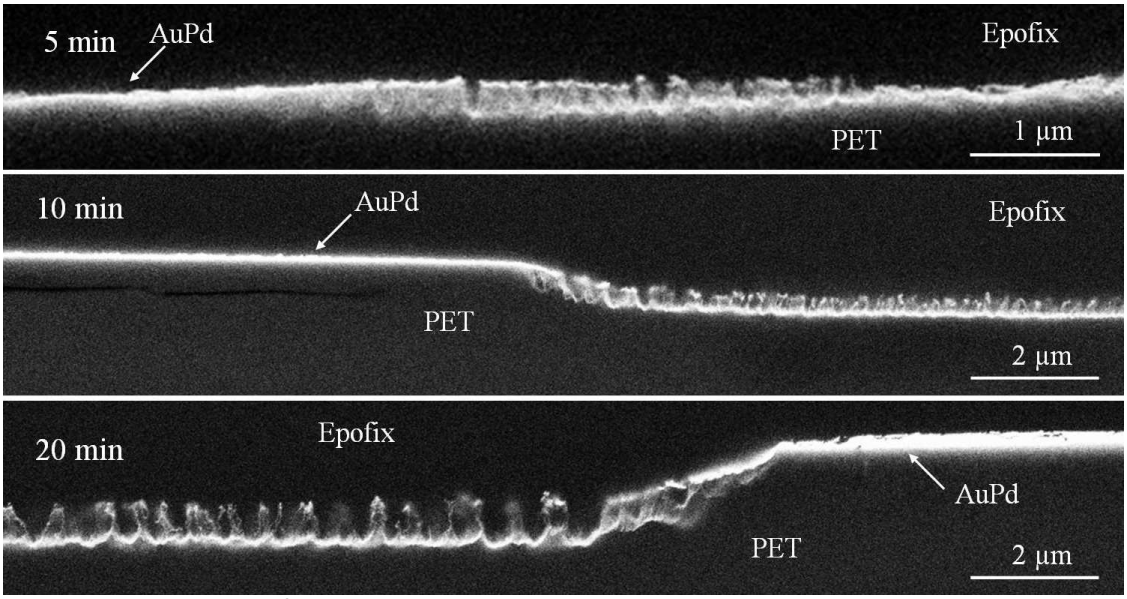

Fig. 51: Cross sections of micro patterned and subsequently plasma treated PET samples (Thermanox) (selected pictures). AuPd coated regions appear flat; they were not affected by the plasma treatment. PET regions show etching, nanofibrils were generated.

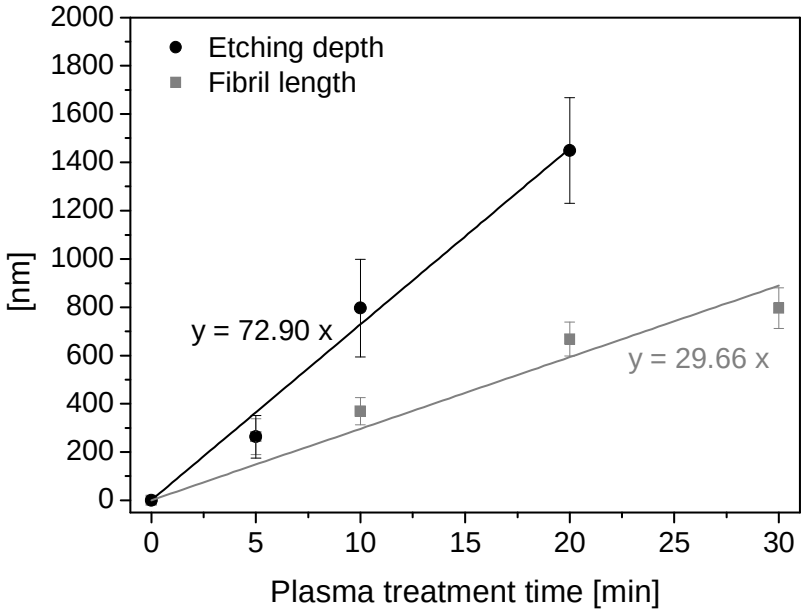

Fig. 52: Variation of fibril length and etching depth on PET film (Thermanox) with plasma treatment time. Treatment conditions were 0.1 mbar and 100 W.

At this point, we checked if the detected surface structures and tendencies were specific to Thermanox films or if they could also be found in other crystalline biaxially stretched PET films from other providers. For this purpose, we performed similar experiments with Hostaphan-RN and Mylar A and analysed the surface topography (see Appendix A for SEM pictures). Both films showed bumps, ridges and fibrils with similar dimensions at plasma times >1 min. The variation of the density number of fibrils or fibre bundles with time was also similar for the three materials, as shown in figure 53. Obviously, the etching mechanism must be the same for all of them. The honeycomb pattern observed for Thermanox at short plasma times (<1 min) was not observed in the other films.

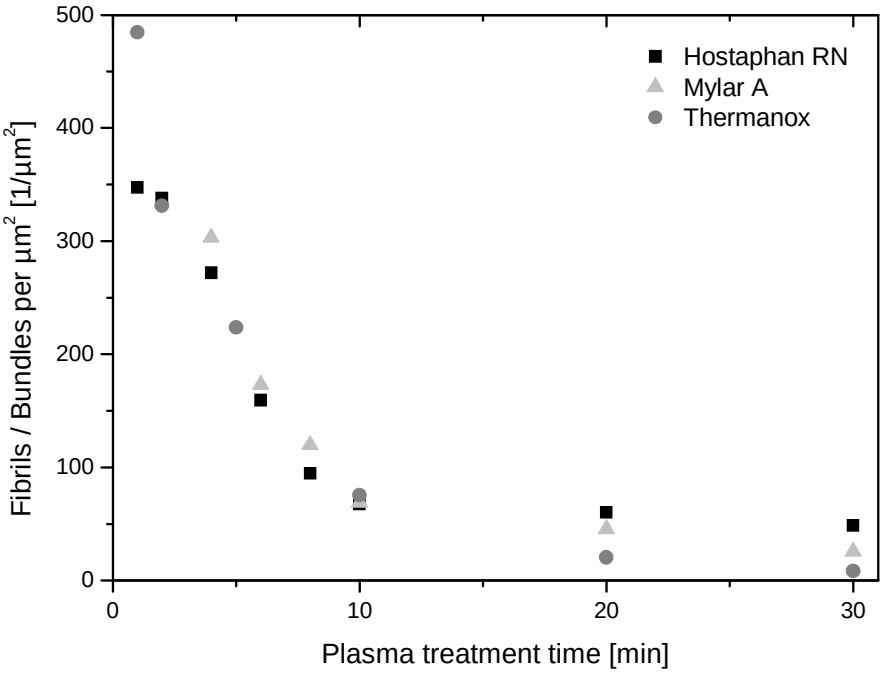

Fig. 53: Number of fibrils / fibril bundles per μm^2 after different plasma treatment times at 100 W and 0.1 mbar of three commercial biaxially oriented PET films from different providers.

5.2.5 Electrode temperature

Thermanox films were plasma treated at -10°C, 0°C, 5°C, 10°C, 20°C, 40°C, 60°C and 80°C using the tempered sample stage described in section 5.1 (fig. 40). Figure 54 shows representative SEM images of obtained topographies. Below 0°C, a hilly landscape with ridges and short incipient fibrils could be recognized. Higher temperatures afforded longer fibrils that collapsed above 20°C. The structure evolution suggests accelerated etching of the PET sample with increasing electrode temperature. These results will be discussed more in detail in section 6.2.

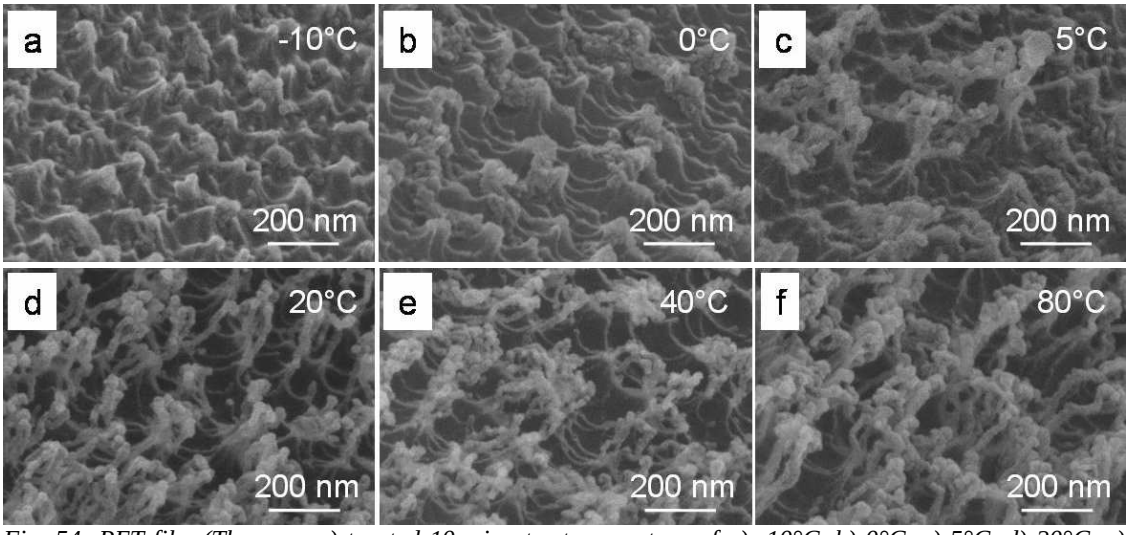

Fig. 54: PET film (Thermanox) treated 10 min at a temperature of a) -10°C, b) 0°C, c) 5°C, d) 20°C, e) 40°C, and f) 80°C. Plasma conditions were 100 W and 0.1 mbar. Samples were tilted 45° for imaging.

5.2.6 Tilted sample stage

Several experiments were performed by placing the PET sample on a tilted disposition (30°, 45° and 60°) to the electrode (see section 4.4 for details). SEM analysis of the sample rim showed tilted nanofibrils with comparable dimensions in all films (fig. 55). Tilting angle varied depending on the inclination of the sample stage during plasma treatment. For a tilt angle of 30° the tilt angle of the fibrils could be estimated from the SEM pictures to be about 30° as well. Plain view images of samples tilted 30° did not differ from perpendicular fibrils because fibrils bent under the electron beam of the SEM. At higher tilt angles estimation of the tilt angle was not possible because fibrils condensated strongly. These results corroborate that etching is highly directional under our experimental conditions.

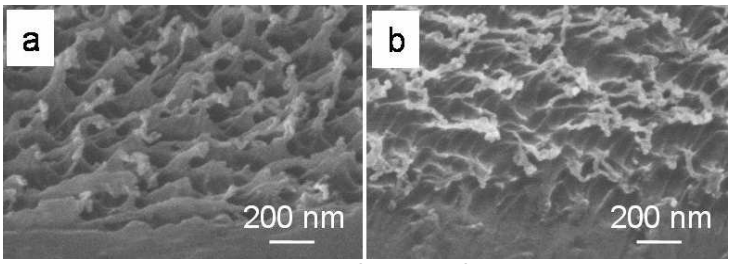

Fig. 55: SEM images at the rim of the PET film (Thermanox) treated at 0.1 mbar and 100 W for a) 5 min at a tilt angle of 30°, b) 10 min at a tilt angle of 60°. Samples were tilted 40° for imaging.

5.3 Influence of material properties on the surface nanostructures

5.3.1 Crystallinity

Amorphous and semicrystalline PET films were prepared by compression moulding and either rapidly quenched (amorphous film) or slowly cooled from the melt (semicrystalline samples). The degree of crystallinity of the samples as determined by DSC is shown in Table 8.

Tab. 8: Degree of crystallinity of PET samples

PET	**Company**	**Crystallinity [%]**
Laboratory-made films	Quenched	0
	Slowly cooled (10°C/min) from the melt	35
Commercial, biaxially oriented	Goodfellow	0
	Nunc, Thermanox	35

The films were plasma treated under equivalent conditions and the weight loss of the samples was determined (fig. 56). At plasma times below 10 minutes both samples showed a linear decrease of weight loss with plasma treatment time. The amorphous samples showed higher weight loss rate, indicating that the polymer chains in the amorphous state were etched more easily. At etching times above 10 minutes, etching of the amorphous sample was significantly slowed down. Deceleration was less significant in the semicrystalline sample. After 60 minutes of plasma treatment, the weight loss of the amorphous sample was lower than the weight loss of the semicrystalline sample.

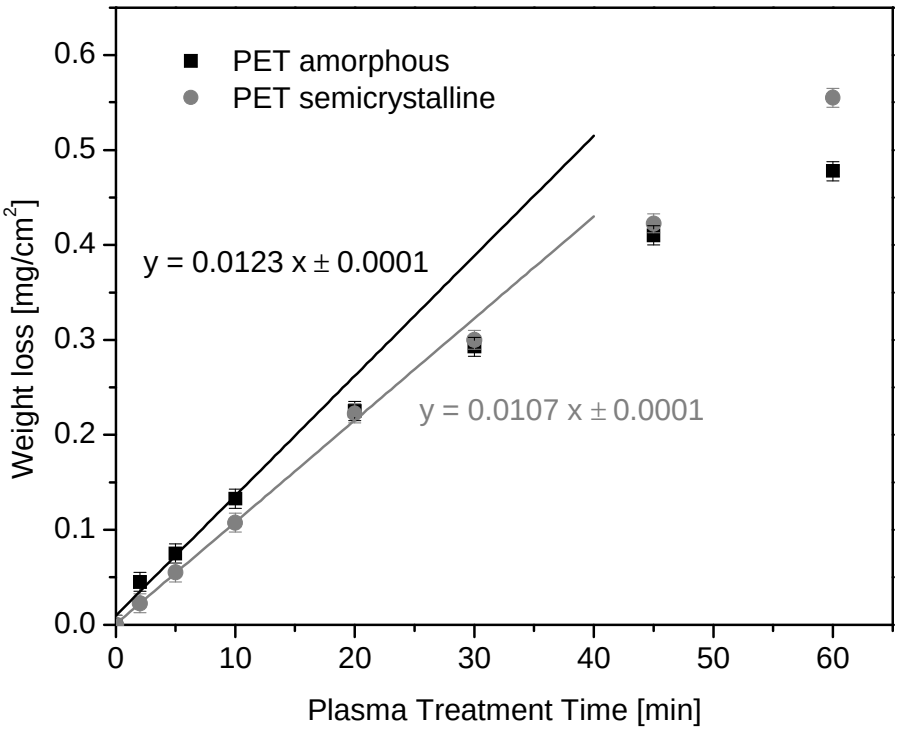

Fig. 56: Weight loss of laboratory-made amorphous and semicrystalline PET films after plasma treatment at 100 W and 0.1 mbar.

We hypothesized that the increase of temperature during plasma treatment (see fig. 41) could induce the formation of ordered domains in the amorphous PET sample and this could influence etching rate. In order to check this assumption, the thermal properties of the amorphous PET samples after plasma treatment at different times were analysed by DSC and compared. The melting curve of non plasma treated amorphous PET film is shown in figure 33 (black), showing the glass transition (T_g~75°C), the cold crystallization exotherm (T_c~150°C) and the melting endotherm (T~250°C). Figure 57 shows the DSC profiles of the glass transition corresponding to PET samples after plasma treatment at different times. A weak shoulder at a temperature below T_g that moved to higher temperatures with increasing plasma treatment time was visible and appeared as a pronounced endothermic peak at 78°C after 20 minutes plasma treatment (fig. 57b). Such profile is characteristic of physical ageing (or enthalpic relaxation) effects of supercooled polymer samples when stored at temperatures below T_g [189]. Note that the temperature at the sample during the plasma experiment approached 60°C after 20 minutes treatment,

as indicated in the inset in Figure 41. The ageing peak disappeared after 60 minutes plasma treatment, in agreement with the experimental observation that the temperature at the sample overcame T_g and physical ageing effects were erased (see section 6.3 for discussion).

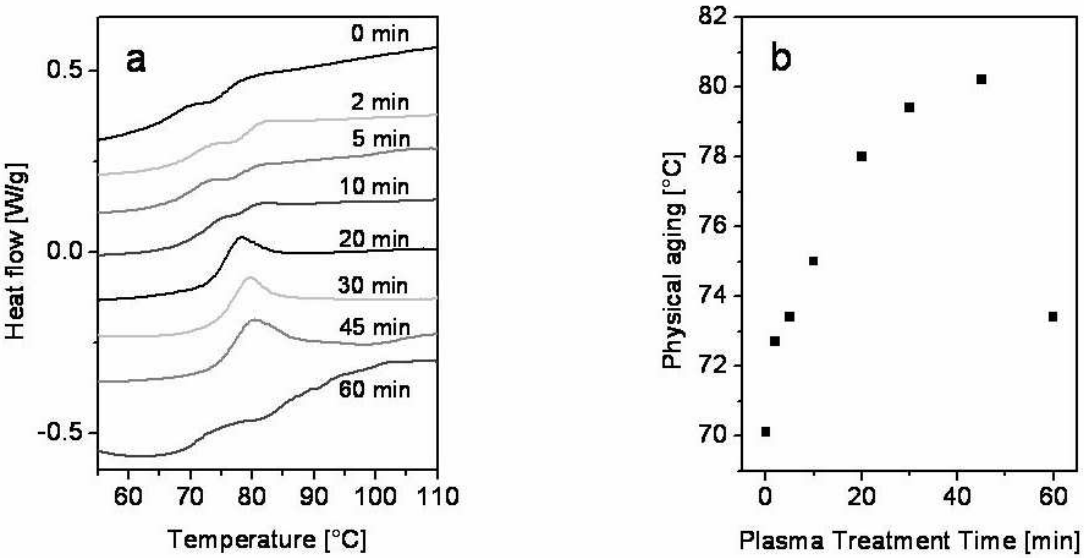

Fig 57: a) DSC melting profile of amorphous PET samples after different plasma treatment times at 100 W and 0.1 mbar. b) Position of ageing peak of the PET samples.

These results demonstrate that the temperature indicated by the thermocouple represents quite well the real temperature at the sample surface during plasma treatment. In the experiment at 60 minutes, the thermocouple indicated a maximum temperature of 77°C (fig. 41). According to the disappearance of the ageing peak in the DSC curves, the sample must have reached 80°C for a short time. A difference of less than 5°C between the measured and the real temperature seems reasonable since the thermocouple is located inside of the electrode and not directly exposed to the plasma.

The position of the cold crystallisation exotherm also showed a small variation with increasing plasma treatment times (fig. 58). A shift to lower temperatures was visible and became more pronounced in the samples that had been plasma treated for longer than 10 minutes. This result indicates that the increase in temperature during plasma treatment allowed a certain degree of chain mobility and reorganization that facilitated posterior

crystallization. No significant difference in the cold crystallization enthalpy was found between samples that were plasma treated during times below 45 minutes (ΔH = 46 J/g). However, after 60 minutes plasma treatment the cold crystallization enthalpy was reduced to 40.4 J/g, indicating that the higher temperatures reached during the plasma treatment already allowed initiation of the crystallization process (up to 5%). The melting endotherm did not change with plasma treatment and had an enthalpy of 46.4 J/g corresponding to a degree of crystallinity of 37 %.

The exposed results indicate that the increase of temperature during plasma treatment significantly changes the morphology of the amorphous PET sample. These changes may be responsible for the differences in etching rate observed between the amorphous and the semicrystalline samples. Section 6.3 discusses these issues in detail.

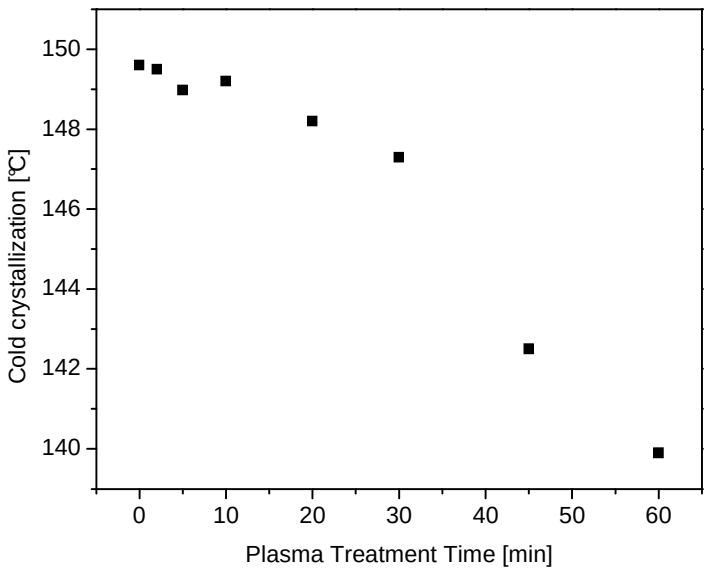

Fig. 58: Variation of the cold crystallization temperature of the amorphous PET samples measured by DSC after plasma treatment for different times.

The surface topography of the amorphous and crystalline PET films after plasma treatment was analyzed by SEM and is compared in fig. 59. Different topographies between both samples were observed after plasma treatment for times below 10 minutes. Incipient fibrils were found in the semicrystalline sample. In the amorphous sample nanostructures with the same magnitude were generated but the structures were less

defined than in the crystalline sample. After 10 minutes, both samples showed similar fibrillar topography, although fibril density in the semicrystalline sample was significantly higher. These results suggest that the polymer microstructure influences material response to plasma treatment and, consequently, the obtained surface design. The thermal history of the sample prior to plasma treatment, and the temperature treatment that the sample undergoes during plasma treatment must be taken into account in order to understand the structure formation mechanism.

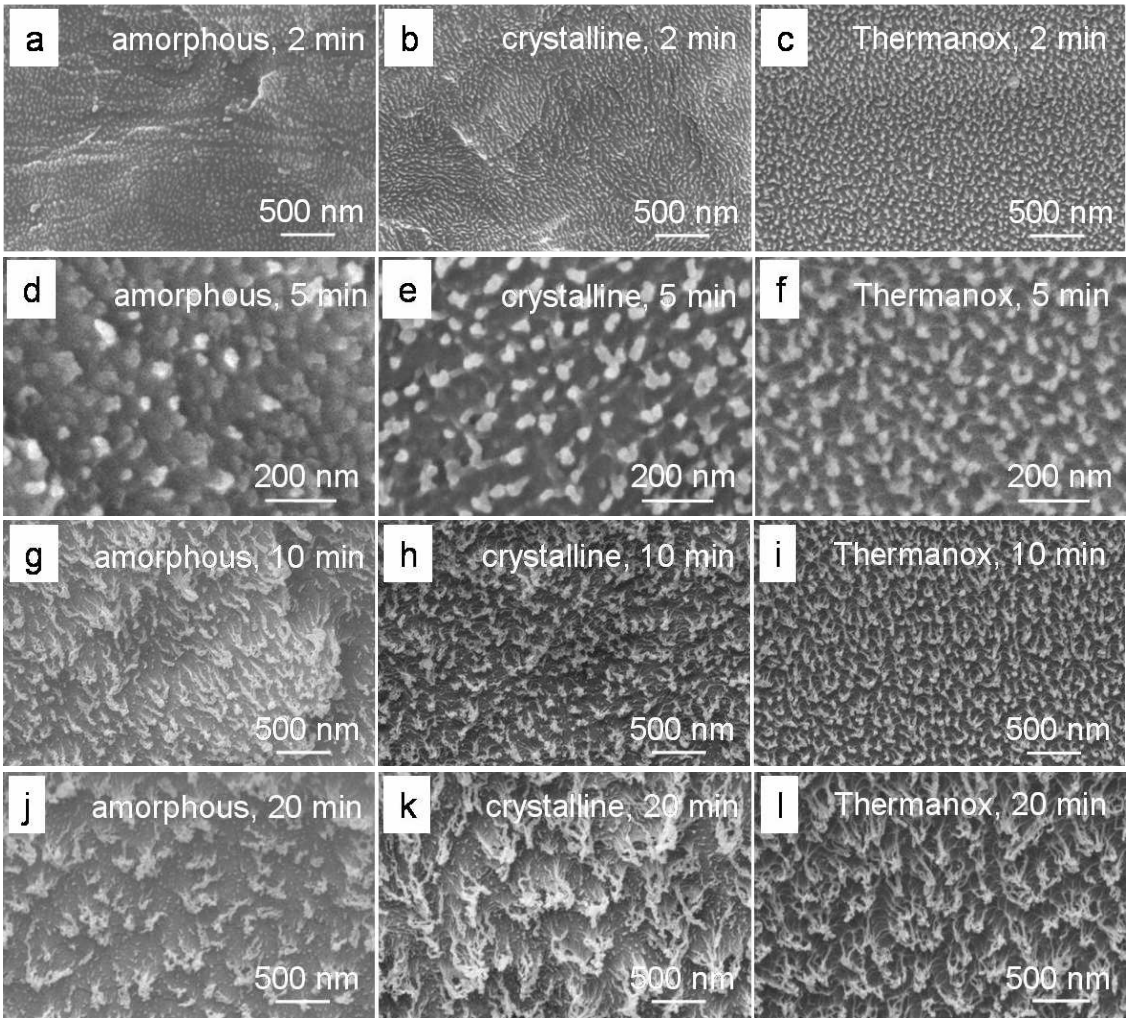

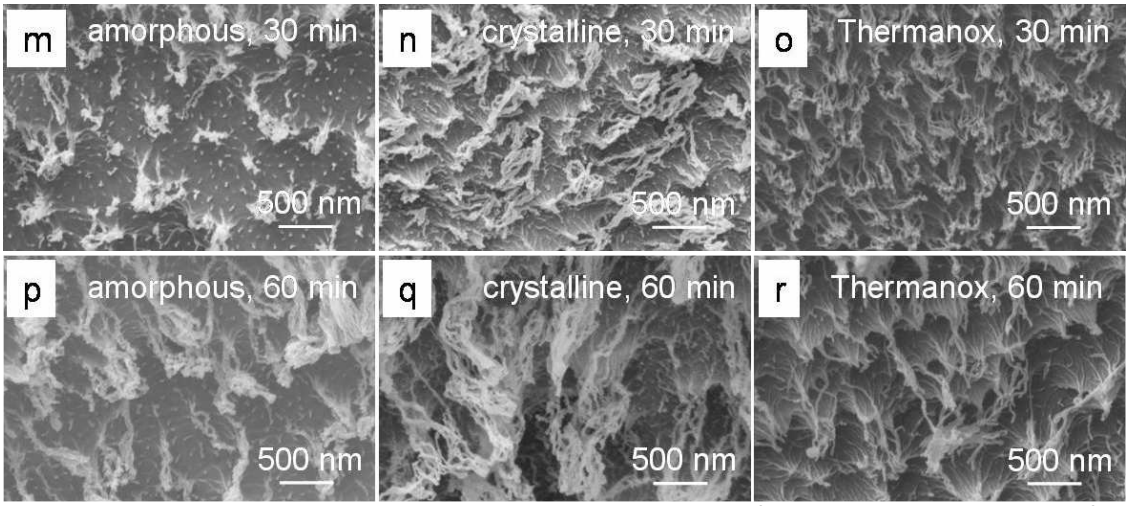

Fig. 59: Laboratory-made amorphous and semicrystalline PET films and commercial PET film (Thermanox, semicrystalline, biaxially oriented) after plasma treatment at 0.1 mbar and 100 W. All samples are tilted 30°. It should be noticed that scale is different in pictures p-r.

5.3.2 Orientation

Figure 60 compares the weight loss of a laboratory-made semicrystalline film and a biaxially stretched semicrystalline film (Thermanox) after plasma treatment. Both samples showed similar weight loss independent of the orientation history. After 10 minutes, the etching rate decelerated. The deceleration was more significant in the semicrystalline sample than in the oriented semicrystalline sample.

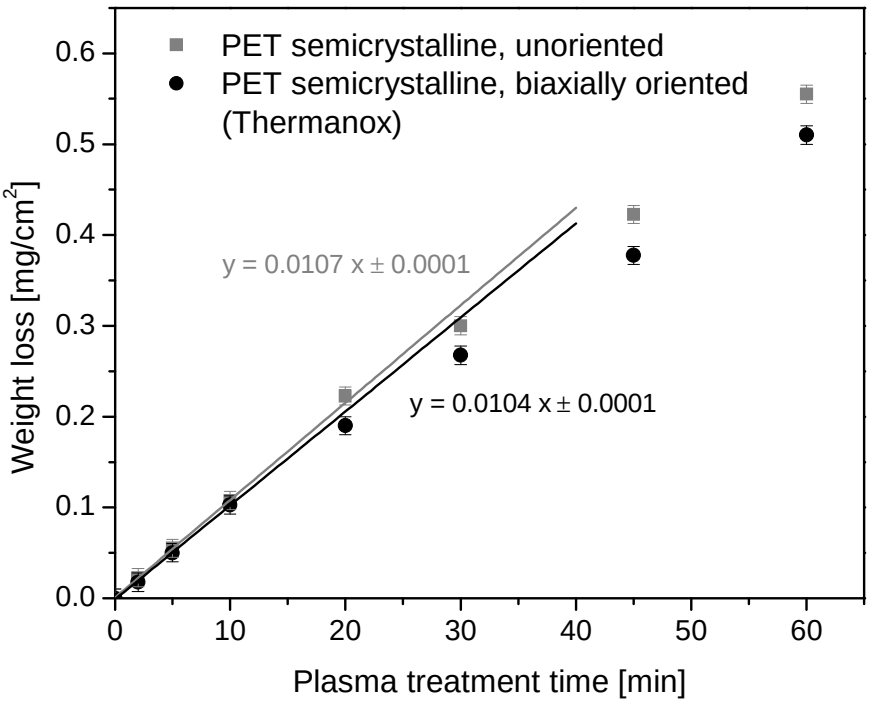

Fig. 60: Weight loss of unoriented and biaxially oriented semicrystalline PET films after plasma treatment at 0.1 mbar and 100 W.

Figure 59 shows the surface structures of the oriented and non-oriented semicrystalline films. Similar fibrillar structures were observed in both samples, but fibrils were better defined and more homogeneously distributed in the biaxially oriented sample. It is important to note that the mechanical history of a sample strongly influences its crystalline morphology (flow-induced microstructure). An increase in chain orientation by stretching the sample from the amorphous (as in the commercial film) typically favours nucleation of crystals. Therefore, in spite that both films have similar degrees of crystallinity, the size and size distribution of the crystalline domains in each film is expected to be very different.

In order to further investigate a possible influence of orientation in the surface topography, a series of experiments with monoaxially oriented samples (commercial and laboratory-made) were performed. Commercial uniaxially stretched amorphous PET threads were plasma treatment under similar conditions as used in the previous

experiments (100 W and 0.1 mbar) (fig. 61). Homogeneously but stochastically distributed fibrillar structures were already visible after 3 minutes plasma. Fibrils and walls collapsed with increasing plasma treatment time. These structures were only present along a stripe at the upper part of the thread, covering about one third (120°) of its surface. The rest of the surface remained unchanged. Closer analysis at a cross section of the thread showed that fibrils length decreased across the curved surface: they were longer at the top and became shorter with increasing curvature. From 45° to 60°, the topography changed from fibrils to grooves (fig. 62). It is important to note that the angle of ion bombardment with respect to the surface changes with the curvature. The higher the incident angle, the shorter were the structures.

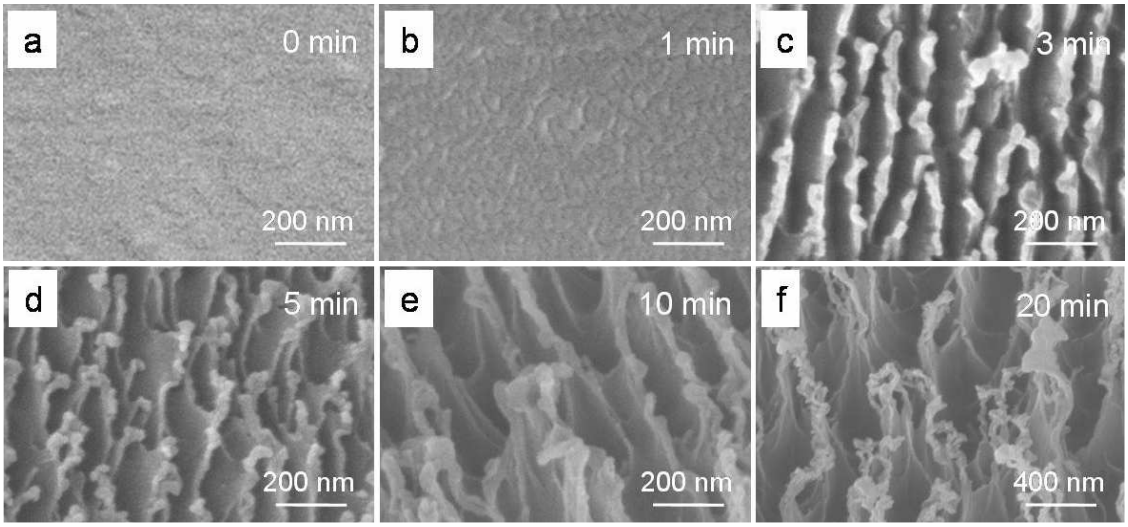

Fig. 61: Plain view of plasma treated PET threads (diameter 0.1 mm). Thread axis is horizontal. Plasma parameter were 0.1 mbar and 100 W. With increasing treatment times fibrils with increasing length were generated. Alignment of the fibrils perpendicular to the stretching direction was observed.

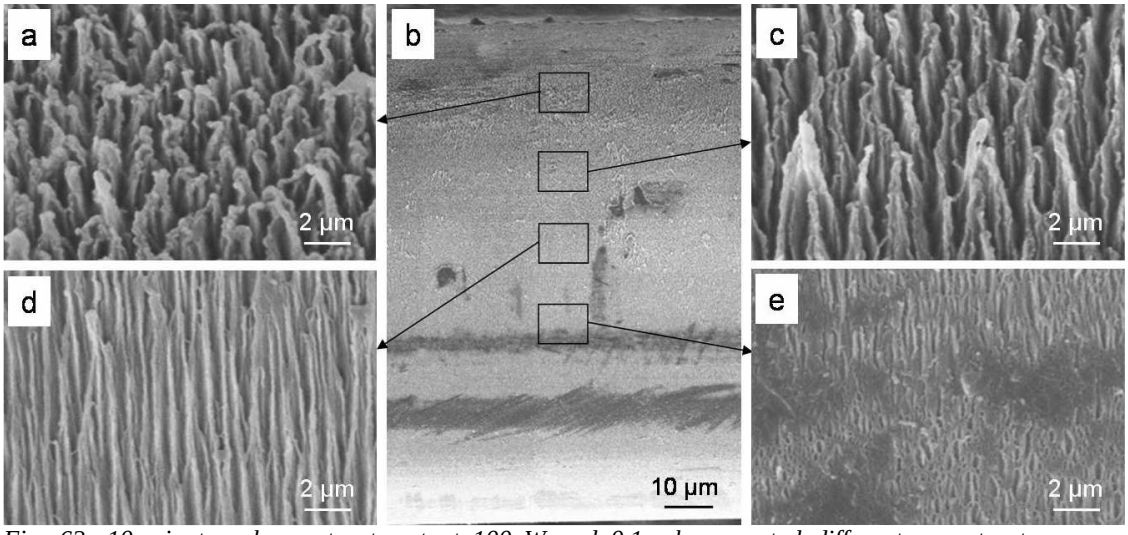

Fig. 62: 10 minutes plasma treatment at 100 W and 0.1 mbar created different nanostructure on a commercial PET thread. The shape of the nanostructures varied with the position on the thread. a) and c) Perpendicular ion bombardment led to a fibrillar surface on top of the thread, whereas a decreasing incident angle generated d) grooves and then e) holey structures.

Cross sections of plasma treated threads were imaged to obtain the variation of fibrils length with plasma treatment time (see Appendix B for SEM images). Fibrils on the thread were much longer than those observed on the films under similar plasma treatment conditions. The rate of fibril growth was 82 nm/min (fig. 63). Note that this rate is 2.7 times higher than the rate in semicrystalline biaxially oriented films (30 nm/min, fig. 52).

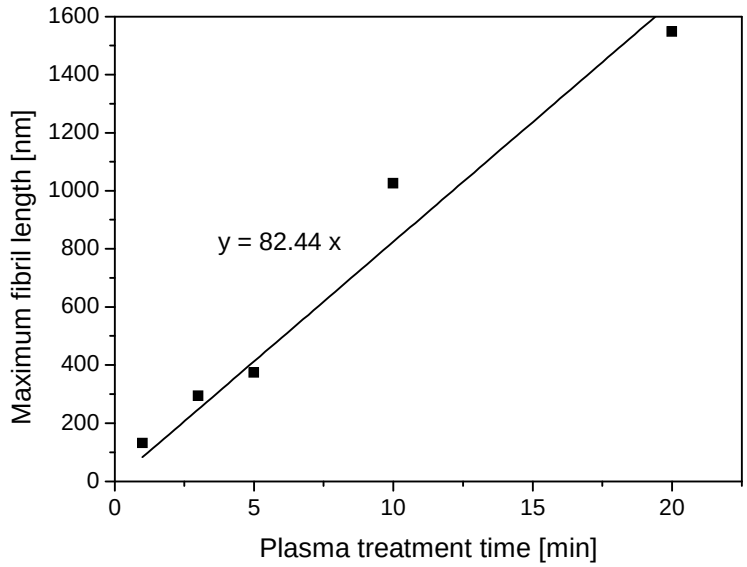

Fig. 63: Fibril length on the surface of plasma treated PET threads increases linearly with plasma treatment time.

Uniaxially stretched PET samples with controlled thermal histories and orientation were also prepared. Samples were stretched at a temperature above T_g (100°C) from the amorphous or semicrystalline film and, in some cases, annealed at the same temperature maintaining the sample in the tester under load (table 6 in chapter 4.3.5 and table 9). The degree of orientation and the crystallinity were analysed by X-ray diffraction and DSC experiments on the stretched fibres.

Tab. 9: Thermal and mechanical history, crystallinity and degree of orientation, $<P_2>$, of uniaxially stretched PET samples. Degree of crystallinity was measured after stretching in the middle of the stretched parts.

Orientation, $<P_2>$	Thermal history, crystallinity w_c
Uniaxial stretched from amorphous	19.7 %
Uniaxial stretched from amorphous	Annealed 75 min at 100°C in the tensile tester directly after stretching without removing the clamps, 44.7 %
Uniaxial stretched from crystalline, 0.852 ± 0.002	44.4 %

Higher elongation (ca. 400 %) was achieved when stretching the sample from the amorphous state than from the semicrystalline state (ca. 240 %). Neck formation was observed when stretching the semicrystalline sample, while the amorphous sample flows more easily and does not form a neck at these elongations. X-ray analysis confirmed higher orientation degree in the oriented semicrystalline sample, with better defined diffraction spots concentrated at the equator (fig. 64) [190]. The stretching process at 100°C induces crystallization of the amorphous sample. Annealing after stretching further favoured relaxation and ordering of the stretched polymer chains and resulted in an enhancement of intensity of the diffraction spots and higher crystallinity.

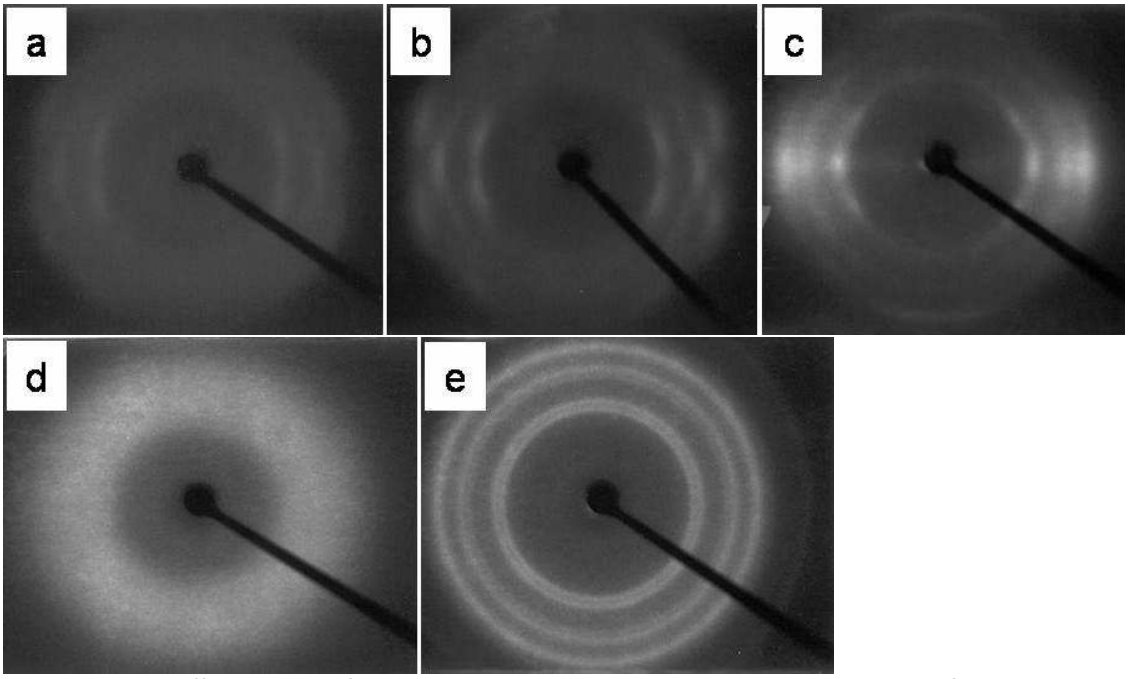

Fig. 64: WAXS diffractograms of PET samples indicated in table 9. a) Uniaxial stretched from amorphous, b) uniaxial stretched from amorphous and subsequently annealed, and c) uniaxial stretched from crystalline. Stretching direction is vertical. For comparison, the WAXS diffractograms of the original films are also included. d) Amorphous and e) crystalline PET.

Figure 66 shows the obtained surface structures after plasma treating the stretched samples. For comparison, both the surface structure of the oriented parts and the surface structure of non-oriented parts of the sample (from the clamped end during stretching) are shown (schematic of uniaxial stretched sample shown in fig. 65). The black arrow indicates the stretching direction. All stretched samples showed nanofibrils, both at the clamped end and at the elongated parts. In the oriented sample from the amorphous film, the nanofibres in the stretched region appeared aligned forming rows. Row direction was perpendicular to the stretching direction. This superstructure could not be found at the surface of the clamped end, suggesting that it is a consequence of the orientation process and not of the thermal treatment. If the oriented fiber was annealed after stretching, the fibrils were no longer aligned. Stress relaxation and further crystallization of the ordered domains during annealing seemed to blur the pre-existing orientation-related morphology for the plasma process. The semicrystalline sample stretched after crystallization also showed aligned fibrils. Neither semicrystalline nor amorphous biaxial oriented samples showed such alignment of the fibrils (fig. 67).

Fig. 65: Schematic of uniaxial stretched PET sample.

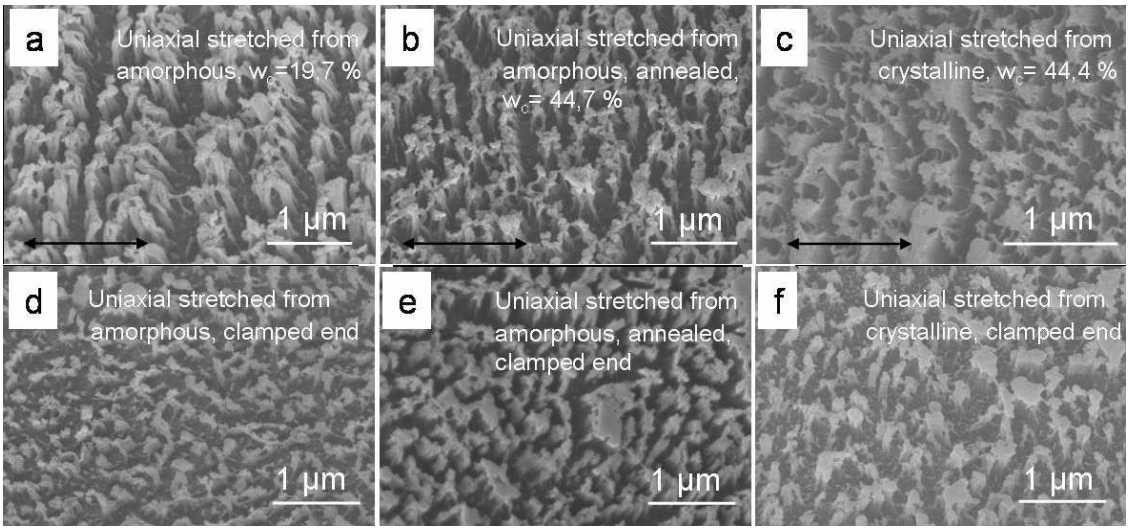

Fig. 66: PET samples after uniaxial stretching and subsequent plasma treatment. a) Stretched from amorphous film, b) stretched from amorphous film and annealed in the tensile tester after stretching, and c) stretched from semicrystalline film. d-f) Piece of the clamped end of the samples a-c after plasma treatment. Treatment conditions were 10 minutes at 100 W and 0.1 mbar. Pictures are tilted 30°.

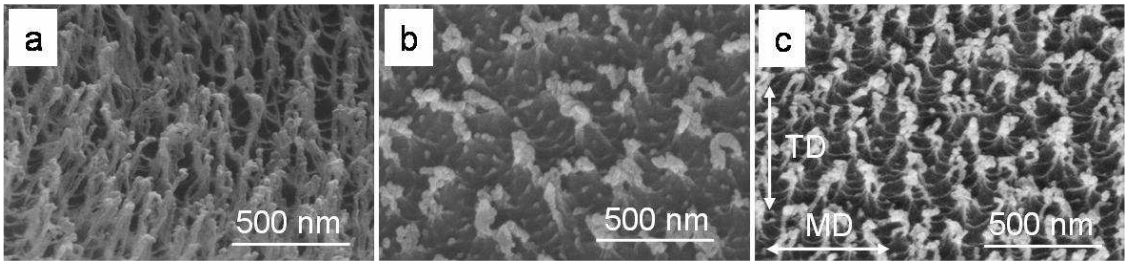

Fig. 67: Commercial biaxially oriented PET films from different suppliers after 10 minutes oxygen plasma at 100 W and 0.1 mbar. a) Thermanox, crystallinity 35%, b) Goodfellow, amorphous, and c) Hostaphan RN, crystallinity 35%. Drawing directions of Hostaphan RN are indicated as machine direction (MD) and transverse direction (TD). Pictures are tilted 30°.

5.3.3 Chemical structure

Polymer materials with different chemical structure were plasma treated under similar conditions as those used for PET. The following samples were tested (see Appendix C for a representation of the chemical structure):

- Two polyesters with a chemical structure close to PET
    - Poly(ethylene naphthalate) (PEN), semicrystalline (37.5 %), biaxially oriented
    - Poly(buthylene terephthalate) (PBT), semicrystalline (39.6 %), biaxially oriented
- Two fluor-containing polymers
    - Tetrafluoroethylene-perfluoromethoxyethylene copolymer (Teflon PFA), amorphous, biaxially oriented
    - Tetrafluoroethylene-hexafluoropropylene copolymer (Teflon FEP), semicrystalline (27.6 %), biaxially oriented
- A silicone, Polydimethylsiloxane (PDMS), amorphous film prepared by mixing liquid precursors
- Ultra high molecular weight Poly(ethylene) (UHMW-PE), semicrystalline (32.9 %). Film was peeled with a long blade from a rotating, large diameter solid rod, which was produced by pressing powder and then sintering it.
- Polystyrene (PS), amorphous film prepared by extrusion, biaxial stretched using rollers that are in-line and perpendicular to the direction of extrusion
- Polymethylmethacrylate (PMMA): amorphous film fabricated by melt extrusion (molten polymer is cast onto chilled calendar rolls to produce the film).

Figure 68 shows the surface structures of the different polymers. The three polyesters, PET, PEN and PBT, showed similar fibrillar structures. PEN fibrils exhibited a diameter of about 20 – 30 nm like PET. Freestanding as well as condensated fibrils were observed. In contrast, the PBT fibrils were strongly condensated, no single fibril could be observed. Fibril diameter was in the same magnitude as PET and PEN. Teflon FEP showed long nanofibril bundles at the top of pyramidal structures. Fibril diameter was measured between 15 to 40 nm like on PET, but fibril length was at least five times higher. Condensed nanofibrils were also found on Teflon PFA with a diameter between 25 and 40 nm. Fibrils were longer than on PET but shorter than on Teflon PFA. PE and PS show an incipient surface structure, but not well defined. On PE, bumps with a diameter between 20 and 90 nm were generated. Bump size on PS was between 10 and 55 nm.

Several PS bumps looked like they were coalescenced. On PMMA a rough surface covered with bumps between 50 and 230 nm in size was generated. PDMS showed no nano structures but a wavy structure with a period of about 4 microns. It is important to note that oxidative plasma treatment of PDMS generated a silica surface layer that cannot be further removed. This is not the case of the other polymers since they do not contain silicon in the chemical structure.

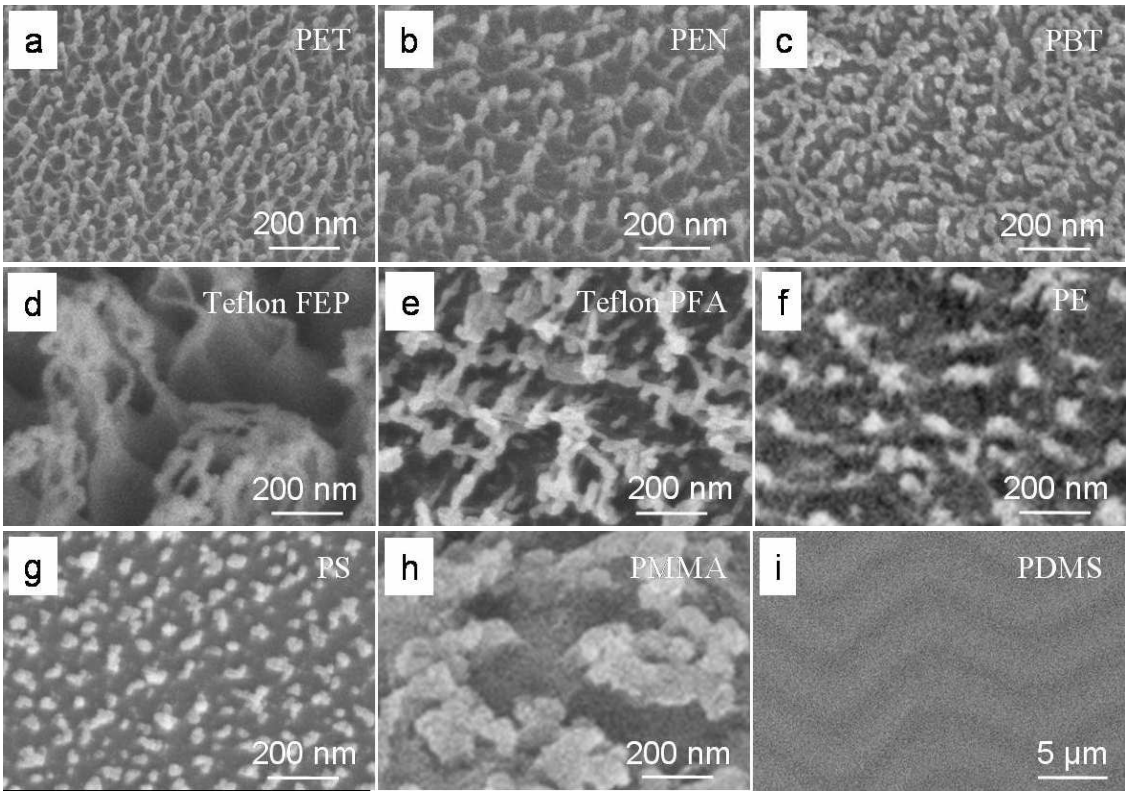

Fig. 68: Different polymers after 10 minutes of oxygen plasma treatment (at 100 W and 0.1 mbar if not stated otherwise). a) PET, b) PEN, power 50 W, c) PBT, d) Teflon FEP, e) Teflon PFA), f) UHMW-PE, g) PS, h) PMMA, and i) PDMS, time 20 min. Samples a-e were tilted 45° for imaging, f-h were tilted 30°, i plain view.

5.4 TEM analysis of the internal structure of the nanofibrils

In order to gain information about the internal structure of the fibrils and compare it to the bulk material, we performed several experiments using a transmission electron

microscope. We expected to identify and visualize amorphous and crystalline domains in the fibrils and in the bulk.

Cross sections of plasma treated PET films containing nanofibrils on the surface were prepared by ultramicrotomy after embedding the film in an Epoxy resin. TEM analysis showed very poor contrast between the PET material and the resin and, therefore, TEM images had very low contrast and the fibrils were difficult to visualize. In order to enhance the contrast at the interface between the two polymers, the surface of the PET samples was sputter coated with a 5 nm thin AuPd layer prior to embedding. SEM and TEM images (fig. 69) of the nanofibrils with better contrast could then be obtained.

The TEM pictures showed that the gold coating was not continuous and single gold dots were identified (fig. 69b). Overlapping gold dots generated a Moiré pattern, visible at higher magnification (fig. 69c). Some fibrils were straight while others showed twists. The different lengths of the fibrils in the TEM picture was a consequence of the cutting process. No crystalline or amorphous domains could be identified in the fibrils, even at larger magnifications, except in the crystalline gold dots. In order to increase the contrast between amorphous and crystalline regions, embedded and trimmed PET samples were stained with Rutheniumtetroxid (see section 4.5.3 for details), and cross sections were cut subsequently. This reagent was expected to attach to the amorphous parts of PET and, therefore, amorphous parts should appear dark while crystalline parts should appear brighter in TEM images and thus can be differentiated [191-195]. Unfortunately, TEM analysis of stained samples did not show any difference to the unstained samples. It was not possible to learn anything about the arrangement of amorphous and crystalline domains in the fibrils.

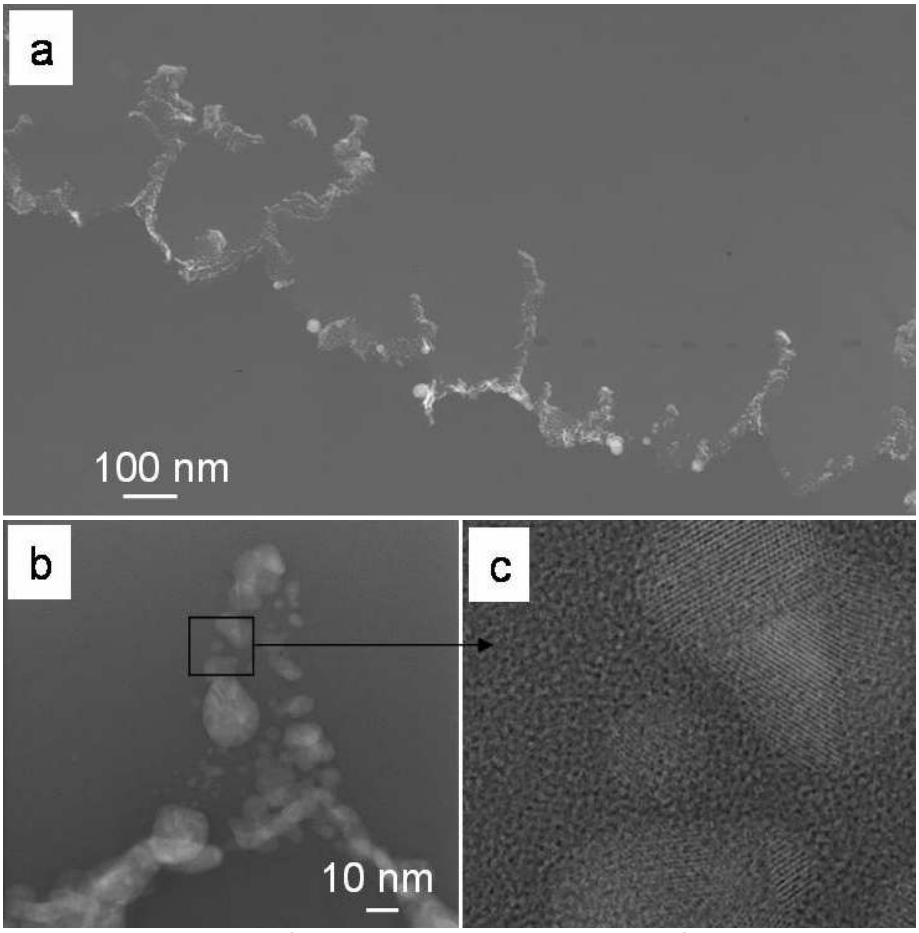

Fig. 69: a) TEM image of 20 min plasma treated PET nano fibres sputter coated with 5 nm AuPd. b) Higher magnification of single fibril. Gold coating on fibrils is not continuous, single gold dots were observed. c) Higher magnification of a small part of one fibril. Gold and PET were identifiedd, but it was not possible to distinguish amorphous and crystalline PET regions.

5.5 Properties of surface structured PET

5.5.1 Water contact angle

The water contact angle (CA) of PET films before and after plasma treatment was measured and compared. Thermanox films showed a water contact angle of 59° ± 3, while Mylar (also a commercial biaxially oriented semicrystalline film from a different provider) showed a contact angle of 76°. The lower contact angle of Thermanox is attributed to a post-processing corona treatment of the film (see section 6.1) which introduced nitrogen functional groups and made the surface more hydrophilic.

Surprisingly, laboratory-made PET films showed a significantly higher contact angle (92°). These films were prepared by compression moulding between two PTFE plates at 270°C. This temperature is close to the degradation temperature of PTFE and, therefore, we cannot exclude some contamination of perfluorinated chains on the surface of our PET. This could be the reason for a higher CA as expected.

Oxygen plasma treatment of the films reduced the contact angle of the PET surface to almost 0° and made it highly hydrophilic, independently of the plasma treatment time. This was a consequence of the oxidation and more incorporation of polar oxygen atoms to the surface during plasma treatment.

Plasma treated PET films were hydrophobized after plasma treatment by coating with a perfluorinated compound (see section 4.3.6 for experimental details). Perfluorinated flat PET showed a contact angle of 113°. Perfluorinated PET films after plasma treatment for increasing times showed increasing values of contact angles that reached 160° after 20 minutes (fig. 70). The drastic change in the surface wettability from highly hydrophilic to superhydrophobic (160°) is attributed to the interplay between the fibrillar surface topography, that only allow a small contact area (Cassie-Baxter theory, see section 2.6) and the low surface energy of fluorinated coatings.

Water droplets showed very low adhesion to the superhydrophobic PET surface (20 minutes plasma treatment) and rolled off the surface as soon as deposited from the syringe. Figure 71 shows captured images of the behaviour of the drop on the surface, visualizing the anti-adhesion effect. Longer plasma treatment times did not further modify the contact angle or the roll off properties.

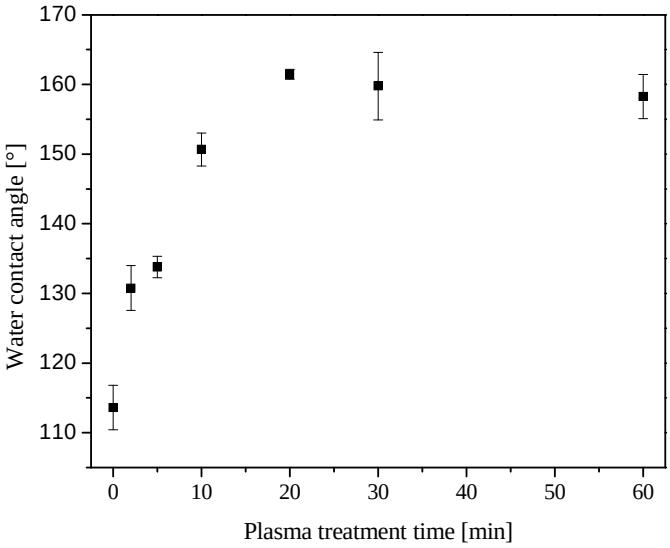

Fig. 70: Water contact angle of PET samples after plasma treatment for different times and posterior perfluorination.

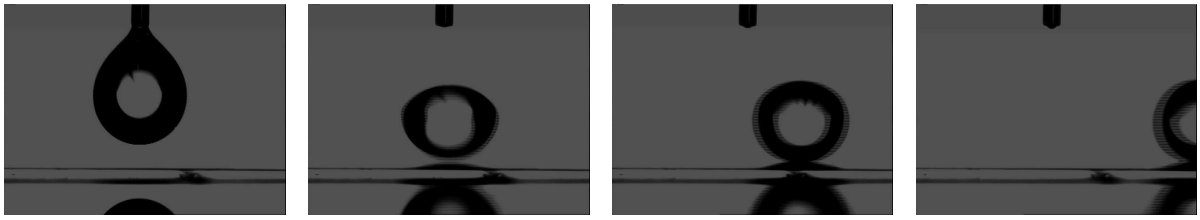

Fig. 71: Roll off of a water drop deposited on a PET surface after 20 minutes plasma treatment and perfluorination.

5.5.2 Adhesion and friction

The adhesion properties of plasma treated PET films (Thermanox) and non-treated controls were measured. Representative force-distance curves are shown in figure 72. The pull-off force is the force at the pull-off event and is a measure of the adhesion performance of the surface. For the original Thermanox film, a low value of the pull-off force was obtained (350 μN). Similar measurements were performed on the Thermanox film after 10 minutes oxygen plasma treatment. In this case the pull-off event could not

be detected, indicating that the surface adherence is lower than in the original film. An upper limit for the pull-off force was estimated with 10 µN. This result is attributed to the low density of fibrils after plasma treatment that causes a dramatic decrease in the contact area. The area density of the fibrils was determined with 36 %, so only one third of the original surface is in contact at the beginning of the measurement.

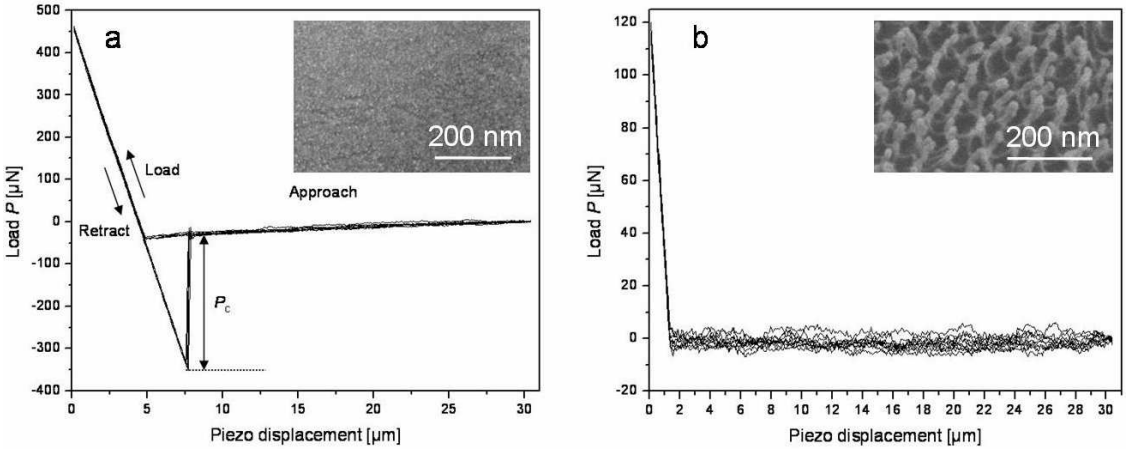

Fig. 72: Load-displacement curves for a) flat and b) plasma treated PET films. Sample is approached to substrate, and then it is loaded to a defined preload. When retracted, sample adheres to substrate until pull-off occurs. Nanostructured PET showed lower adhesion than flat sample. Insets show SEM images of the PET films.

Figure 73 shows the friction coefficient of Thermanox samples measured against substrates with different roughness under different humidity conditions. The original Thermanox film showed a decrease in the friction coefficient from 0.45 to 0.3 with increasing surface roughness up to 1 µm. Above 1 µm the friction coefficient remained constant. An increase in humidity from 47 to 61% resulted in lower friction coefficients. Plasma treated samples (20 minutes) showed similar friction coefficients to non treated films on substrates with roughness below 0.2 µm. The fibrillar bundles were about 315 ± 140 nm in length and 140 ± 55 nm in width. However, an increase in surface roughness led to a significant increase in the friction coefficients up to a value of 0.6. As observed in the non structured surfaces, an increase in humidity led to lower friction.

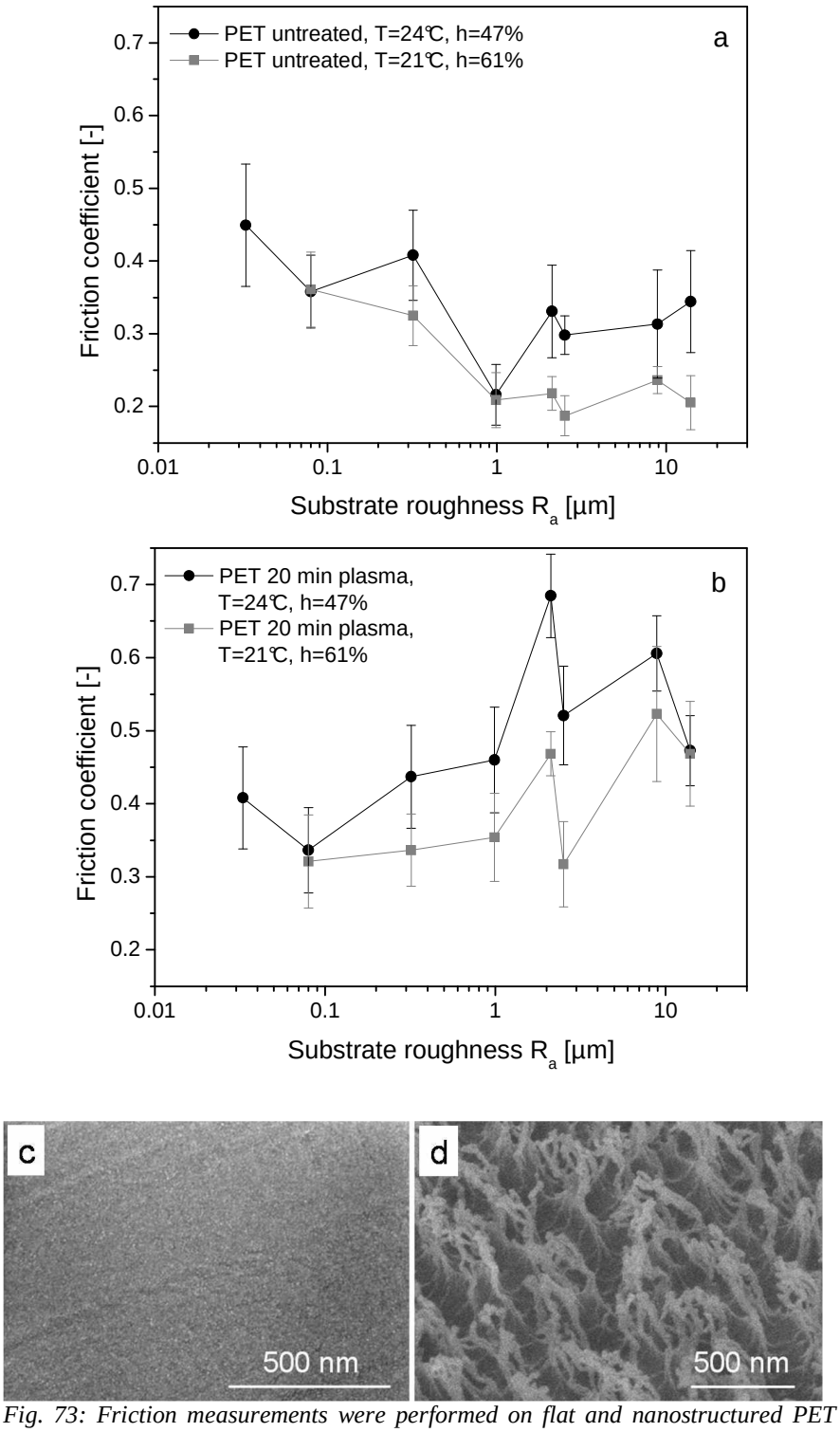

Fig. 73: Friction measurements were performed on flat and nanostructured PET films (Thermanox) on epoxy resin substrates with different roughness. Friction coefficient of a) flat and b) 20 minutes plasma treated PET films. SEM pictures of c) flat and d) 20 minutes plasma treated PET film. Treatment conditions were 100 W, 0.1 mbar and room temperature. Picture d is tilted 30°.

Friction experiments were also performed on plasma treated samples where the fibrillar structures were tilted (see section 4.9 and fig. 74). The friction coefficients were measured by pulling the sample along and against the tilting direction of the fibrils. Plasma treated samples always showed higher friction values than non-treated Thermanox. However, no significant difference in the friction coefficients in the different directions could be detected.

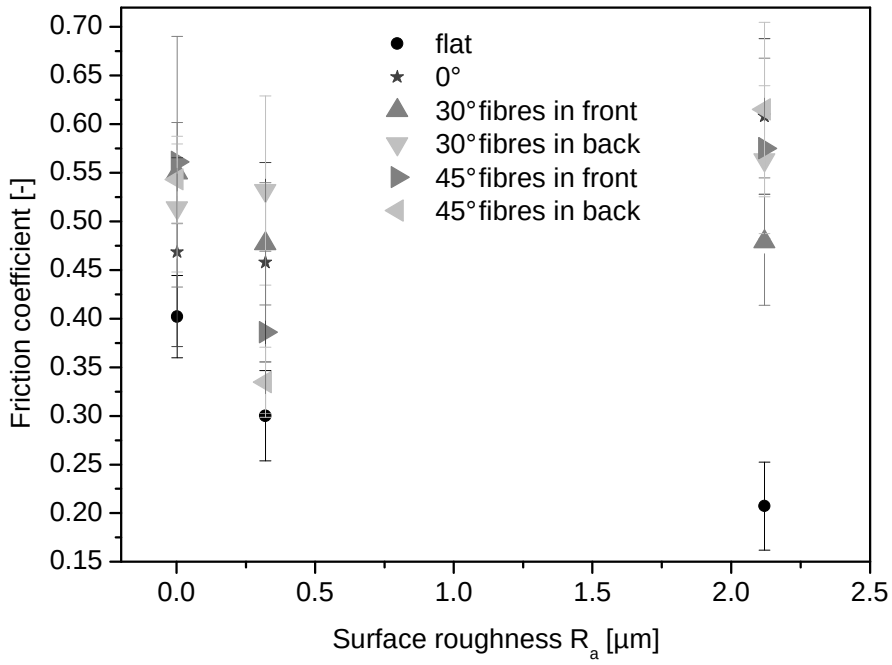

Fig. 74: Friction coefficient in dependence of tilt angle and tilt direction was measured on substrates with different roughness.

5.6 Summary of the results

Fibrillar nanostructures were generated by reactive ion etching with oxygen. A variation of plasma treatment conditions showed that fibril length increased with increasing oxygen content in the process gas, increasing power, treatment time and sample temperature as well as with decreasing pressure. The longer the fibril length the higher was the weight loss, measured directly after the plasma treatment. Fibrils as well as the surrounding material were etched during the plasma treatment, but etching rate of the

fibrils was significant lower. After achieving an aspect ratio of three fibrils started to stick together (condensation). The number of fibrils stuck together in one bundle increased with fibril length.

Material properties such as crystallinity and orientation influenced structure formation. The magnitude of all structures was the same after plasma treatment, but nanofibrils on amorphous samples were less defined than on crystalline samples, especially after short treatment times. DSC measurements of the amorphous sample showed a weak shoulder at a temperature below T_g that moved to higher temperatures with increased treatment time and changed to an endothermic peak after 20 minutes. The position of the cold crystallinisation exotherm also showed a small variation with increasing plasma treatment time. This indicates that due to an increase in sample temperature during plasma treatment relaxation processes can appear in the amorphous film.

Fibrils in biaxially oriented samples were better defined and more homogeneously distributed than in non-oriented samples. Uniaxial stretching of samples, with a high degree of orientation, resulted in nanofibrils aligned perpendicular to the stretching direction.

Plasma treatment of other polymers under the same conditions always led to structuring of the surfaces. On PEN, PBT, Teflon FEP, and Teflon PFA nanostructures were generated. Bumpy structures were fabricated on PE, PS and, less defined, on PMMA. On the PDMS surface a wavy structure was observed after the treatment.

Water contact angle measurements revealed a change from 59° to almost 0° after oxygen plasma treatment independent of treatment duration. Perfluorination of the sample after plasma treatment generated a hydrophobic surface, which changed to a superhydrophobic surface at longer treatment times ($\geq$ 20 min). Nanostructured PET surfaces were antiadhesive and showed an increase in friction coefficient with increasing substrate roughness.

6. Discussion

6.1 Types of etched patterns observed on PET films

Reactive ion etching of PET films was used to produce bumps, ridges, isolated fibrils and condensed fibrils in the form of bundles at the surface. At low levels of etching bumps were observed, which further developed into fibrils with increasing aspect ratio as etching proceeded. The diameter of the bumps and fibrils typically varied between 15 and 40 nm and the distance between features from 20 to 50 nm. These dimensions were maintained independently of the experimental plasma conditions. When fibrils reached an aspect ratio of about 3, they became mechanically unstable and started to collapse and stick together forming bundles. The number of fibrils in the bundles increased when etching was continued for longer. Fibril bundles reached heights of up to 1 µm. Depending on the sample's thermal and mechanical history, these features were either located randomly across the surface (figs. 43, 44, 46, 50, 54), or they were aligned in a preferential direction (figs. 61, 66a and c).

The transition from bumps to fibrils with increasing etching is smooth, as depicted in fig. 50. This evolution suggests that initial bumps at low etching levels are etched more slowly than the surrounding material and act as masks. Assuming that physical etching dominates, as expected from our experimental conditions, the bump pattern is developed vertically in the material and produces long fibrils at higher etching times. Two open questions remain: what is the nature of the bumps and why do they present lower etching rates than the surrounding matrix.

A particular surface topography was observed in Thermanox films after short plasma treatment times (<1 min) (fig. 50b-e) consisting of polygonal structures superposed on the bump pattern. This structure was not observed under similar plasma conditions on other commercial PET samples with comparable thermal and mechanical pretreatment (Mylar, Hostaphan). Considering that Thermanox film is a PET substrate for application

in cell culture, we hypothesized that it may have been previously treated or functionalized for improving biocompatibility and cell attachment. In fact, the supplier of Thermanox plates (Nunc) revealed that one side of the film was treated with a corona discharge in order to increase the surface energy and wetting properties [196]. Corona discharge is a type of plasma treatment performed at atmospheric pressure under conditions that favour free radical formation and chemical reactions involving radicals at the treated surface that incorporate oxygen and nitrogen atoms [197]. Analysis of the surface composition by X-ray photoelectron spectroscopy revealed the presence of nitrogen at the surface, which is absent in the other samples and is not expected in pure PET [198]. However, the nitrogen was found on both sides of the film and the polygonal structures also appeared on both sides.

The polygonal structure of Thermanox was also observed upon chemical etching of the surface with n-propylamine. The surface structures of Thermanox after 30 seconds of plasma etching and 1 hour chemical etching with n-propylamine are compared in figure 75. Both pictures show underlying bumps with similar dimensions.

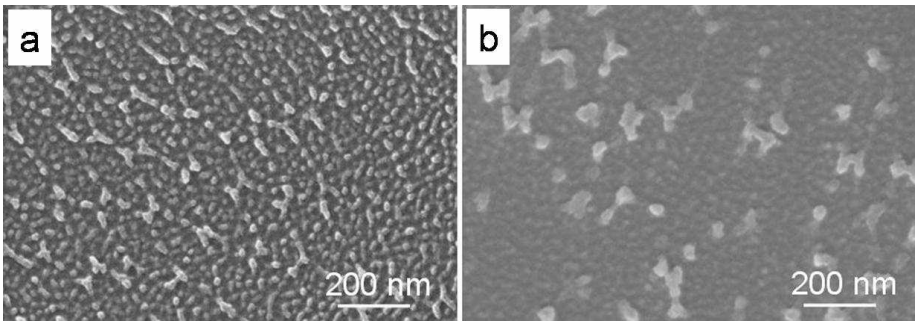

Fig. 75: Comparison of PET surface (Thermanox) after a) 30 s plasma etching and b) 1 hour chemical etching with n-propylamine. Both samples show polygonal structures and underlying bumps with similar dimensions.

The polygonal pattern was also reported by Powell et al. 2003 after plasma treating Thermanox in similar conditions [24]. These authors did not consider the corona pretreatment and claimed that the polygonal structures are a consequence of the formation of a thin film of polar, low molecular weight fragments on PET that undergoes

dewetting. Our results demonstrate that these structures are not specific to PET etching and should be associated with the corona treatment. A dewetting mechanism is plausible considering that the corona treatment introduces more polar groups at the surface.

6.2 Changes in etching and pattern geometry under different plasma conditions

Ion current density, ion energy and atomic and molecular oxygen concentration, in addition to substrate temperature, have been reported to be the most relevant parameters in RIE of polymer surfaces with oxygen gas [199]. These parameters can be varied by tuning the operating variables of the plasma, such as power or pressure. However, changing one plasma parameter usually modifies the others and, therefore, a parametric study is not easy. In addition, as well as the etching rate the etching mechanisms (physical or chemical) and the directionality can also be affected by the changes. These effects will be discussed in the following paragraphs.

A higher gas pressure in the plasma chamber leads to a higher ion density, but also to a higher number of collisions between the ionized particles before they reach the surface (i.e. shorter mean free path). These two effects have a counteracting influence in the etching rate. The negative bias voltage is also expected to increase with decreasing pressure [200]. Therefore, at lower pressures ions will be accelerated more strongly and impact the electrode surface with higher energy. In fact, etching rates usually decrease with increasing gas pressure [201]. Our results show that this dependence is exponential under our plasma conditions and within the pressure range of 0.05 to 1 mbar (fig. 44).

An increase in power in the plasma chamber is expected to generate a higher density of ionized particles that impact the polymer surface [142, 202]. The ion energy is not expected to change significantly with the plasma power [202]. The mean free path of the ions does not change because the total number of particles in the chamber remains constant [202]. The plasma contains more ions, which results in higher etching ability

and thus, higher weight loss and longer fibrils, as found in our experiments (fig. 48 and 46). Similar results have also been reported in the literature for PET [187] and PS [158].

For biaxially stretched PET films, etch rates of 69, 138, and 340 nm/min using powers of 25 W, 50 W, and 100 W were determined at 13.56 MHz, 0.133 mbar, and 10 sccm oxygen [187]. The authors did not give any information about the crystallinity of the samples. We obtained for semicrystalline biaxially stretched samples etch rates of 73 nm/min (measured from cross sections, fig. 49) and of 76 nm/min (obtained from weight loss measurements, fig. 52). The conditions were 24 kHz, 0.1 mbar, and 100 W (gas flow could not be adjusted). The magnitudes of the etch rates are similar, although at the same power of 100 W the literature value is nearly five times higher. This difference could be caused by the different frequencies applied, but varying chamber geometries must also be considered. The etching mechanism changes when the frequency is varied, therefore etch rates are different.

For PS an increase in the diameter, height, and interfibrillar distance and a decrease in fibril density has been reported with increasing power [158]. Our results with PET showed a similar tendency. The aspect ratio of the fibrils increased with power. At power >40W the fibrils collapsed and formed bundles with increasing diameter. The area percentage of the fibrils was 15 % to 24 % for PS and 27 % to 31 % in our case.

Decreasing pressure and increasing power increased the temperature at the electrode in our experiments up to a maximum value of 80°C. Substrate heating in RIE is mostly due to the constant bombardment flux of high-energy positive ions, q_+. According to [203], the rate of substrate temperature rise *dT/dt* depends upon the difference between the ion energy (heat) flux to the substrate and the rate of heat loss from the substrate to the surrounding, $q_L(T)$, as follows:

$$q_n(T) = \rho C_p L\left(\frac{dT}{dt}\right) = q_+ - q_L(T) \qquad (16)$$

where $q_n(T)$ is the net flux to the substrate and ρ, Cp and L are the substrate mass density, specific heat and thickness respectively.

The heat loss function during the RIE process, $q_L(T)$, can be represented by

$$q_L(T) = 2\sigma_{SB}\varepsilon(T^4 - T_0^4) - \kappa_g\left(\frac{dT}{dz}\right) + \alpha\Lambda_0 p(T - T_0) \quad (17)$$

Where σ_{SB} is the Stefan-Boltzmann constant for radiative heat transfer, ε is the surface radiation emissivity constant, T_0 is the wall temperature (assumed constant), κ_g is the thermal conductivity of the gas, dT/dz is the temperature gradient across the electrode gap, α is the accommodation coefficient for molecular heat transfer, Λ_0 is the molecular thermal conductivity of the gas and p is the gas pressure. The first term on the right-hand side of equation (2) represents heat transfer from the substrate to the surroundings by radiation, while the second and third terms account for heat transfer by viscous (independent of p) and molecular (proportional to p) heat conduction to the gas. Solid-state heat conduction from the film to the cathode during RIE is negligible assuming contact between the PET film and electrode is not conformal due to multiscale roughness at both surfaces. Under our typical plasma operating pressures (0.1 mbar), the heat loss function is a combination of radiative and molecular gas conduction and the viscous heat contribution is negligible.

At film temperatures <100°C the RIE rate of polymer films has been reported to depend only to a small degree on substrate temperature [203, 204]. However, chemical etching can take place over the whole temperature range. In fact, higher etching rates with increasing temperature have been reported in the literature in RIE of different polymer materials (eg. PMMA, poly(α-methylestyrene), photoresist Novolak) [201, 203-206]. Our experiments also showed a significant change in the surface topography with temperature (fig. 54), with increased fibril length and clustering in the experiments performed at higher temperatures. This is an indication of stronger etching at higher temperatures, in agreement with reported results. No isolated fibrils were observed at any temperature between -10 and 80°C, in contrast to experiments without cooling/heating and clustering was visible at all temperatures. Similar variations in surface structures of PET after plasma etching by changing T have also been reported by other authors [24]. These results reveal a significant contribution from chemical processes during our RIE experiments that contribute to structure formation and cannot be disregarded.

In the experiments performed with the tempered sample stage, we observed an increase in temperature during the experiment up to a plateau value, after which temperature remained constant for the rest of the experiment (fig. 41). The experiments without cooling never reached a plateau. Other authors have found a similar temperature profile using a cooled sample stage and also reported a parallel increase in the etching rate up to a plateau (see fig. 76) [203]. These authors also demonstrated that the temperature control can be further improved by thermally bonding the sample to the stage using high-vacuum grease. Etching rates of thermally bound substrates remained constant over the time. However, the grease introduces a contamination in the plasma chamber that may also influence the results. For this reason, we did not use any material to improve thermal transport between the sample and the stage in our case. Cryo-sample holders working with He underside cooling are commercial available for some plasma chambers and seem to be the best solution for improving thermal control without introducing contamination.

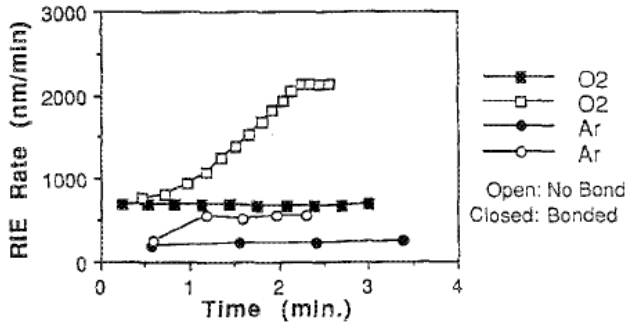

Fig. 76: Effect of thermal bonding on RIE rate of PMMA. (Reprinted with permission from [203]. Copyright 1990, American Institute of Physics.)

An increase in the sample temperature during the plasma treatment may also induce changes in the sample morphology. This depends on the initial state of the polymer sample (amorphous, supercooled, semicrystalline, etc.), its phase diagram and the temperature profile during the experiment. Under our experimental conditions the maximum temperature achieved was 80°C (fig. 41 inset). Taking into account that T_g of PET is 75 - 80°C, rearrangements in amorphous domains (physical ageing) cannot be excluded. Such processes may well influence the etching rate and surface topography of the sample. The next section discusses these issues.

6.3 Controlling surface structures with a crystalline morphology

Significant differences in the etching rate and resulting surface structures were found between amorphous and semicrystalline samples. Under our experimental conditions the etching rate of amorphous PET decreases after 10 minutes of plasma treatment (fig. 56). We interpreted these results as a consequence of ageing effects promoted by the increase in temperature of the sample during plasma treatment, as seen from the DSC measurements (fig. 57). Ageing effects involve reorganization of the polymer chains in the amorphous state at temperatures close to T_g to form densified regions. These regions seem to be more resistant to plasma etching than amorphous domains. As ageing and etching proceed during the plasma treatment, the surface is enriched in densified domains and the overall etching rate (as given by the weight loss) decreases. At the same time, fibrillar structures become more defined as a consequence of a masking effect at the densified regions.

It is important to note that the surface T_g of PET is expected to be lower than that of the bulk. In fact, a surface T_g of 56°C has been reported for PET [207]. The oxidative plasma treatment may cause chain scission and a decrease in the molecular weight at the surface and, in turn, further lower surface T_g (a surface T_g of 53°C has been reported for PET after 30 s oxygen plasma treatment at 13.54 MHz, 50 W, $6.7 \cdot 10^{-4}$ mbar [207]). This means that ageing effects at the surface may start at lower temperatures than in the bulk and occur faster.

Physical ageing occurs when a polymer is in a non-equilibrium state (i.e. supercooled) and is caused by molecular relaxations that are biased in the direction required to drive the material closer to equilibrium. Ageing occurs in the amorphous state but does not easily occur in the amorphous domains of crystalline samples where chain mobility is highly constrained due to the presence of crystallites. Accordingly, we observed a nearly constant etching rate in semicrystalline PET, as expected from a sample that does not undergo significant changes during the plasma process. The slight decrease in etching rate with longer treatment times can be attributed to charge accumulation at the surface of

the material which may deflect incoming ions and may reduce the flux of accelerated ions to the surface [141].

Assuming that the differences in the etching rate between amorphous and semicrystalline PET are due to differences in the etching rate of amorphous and crystalline regions, and considering a semicrystalline polymer as a two-phase material, we estimated the etching rate of the crystalline domains from the formula [208, 209]

$$v_e = c \cdot v_{e,c} + (1-c)v_{e,a} = (v_{e,c} - v_{e,a})c + v_{e,a} \quad [209] \qquad (18)$$

where v_e is the total etching rate (as measured in the semicrystalline PET), $v_{e,c}$ is the etching rate of the crystalline phase, $v_{e,a}$ is the etching rate of the amorphous phase (as measured in the amorphous PET), and crystalline fraction c.

This model also assumes that the etching rate remains constant with time. According to the results shown in fig. 56, this is only true during the first 10 minutes of plasma treatment. Therefore, etching rates v_e and $v_{e,a}$ were obtained by fitting the data from fig. 56 with treatment times below 10 minutes (see fig. 77). Table 10 shows the estimates. Etching rates of 31.2 nm/min and 104.1 nm/min were found for the crystalline and amorphous fractions. The difference between these values determines the selectivity of the etching process. It is important to note that this calculation is somewhat speculative and relevant aspects involved in etching (temperature effects, change in surface chemistry and roughness during treatment or surface restructuring) have not been considered. As such, it should only be taken as indicative.

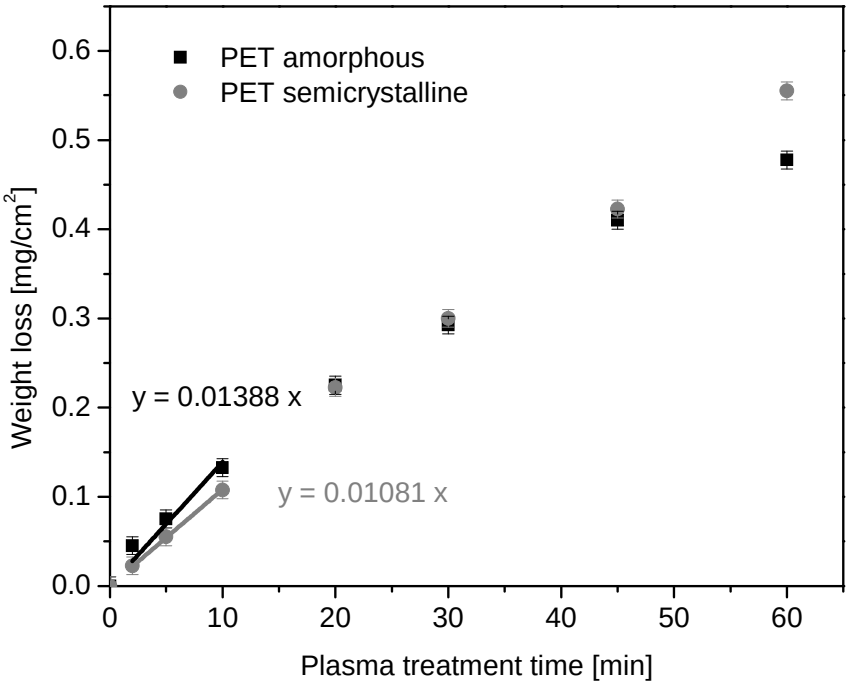

Fig. 77: Weight loss of laboratory-made PET films after plasma treatment. Linear fit between 0 and 10 minutes treatment time was determined.

Tab. 10: Etching rates determined by weight loss experiments using the following data.

PET	**amorphous**	**100 % crystallinity**	**35 % crystallinity**
Weight loss (fig. 77) [mg/cm^{2}min]	0.01388	-	0.01081
Density [g/cm^3]	1.333 [210]	1.455 [132]	1.376
Etching rate [nm/min]	104.1	31.2	78.6

Our hypothesis assumes that the morphology of the PET film is homogeneous across the film thickness. However, there is recent evidence in the literature claiming differences in the degree of crystallinity at the surface and in the bulk [211]. The formation of a "skin layer" a few microns thick that has different properties from the bulk is plausible if processing conditions involve rapid cooling, as in the amorphous quenched PET film. Cooling at the surface will be faster and, therefore, incipient ordering processes may

increase in the interior of the film. This could also explain a decrease in the etching rate with increasing etching depth in the amorphous film.

At this point it is important to consider that semicrystalline PET cannot be described by a simple two-phase model of crystalline and amorphous domains [212]. The morphology of semicrystalline PET is complex and has been demonstrated to contain varying amounts of intermediate ordered morphologies. There, the PET chains are only partially ordered and constrained due to the crystalline domains. The ratio and type of mesomorphic domains strongly depend on the thermal and orientation history (draw temperature and draw rate) of the sample. We hypothesize that these mesophases will present intermediate etching rates between the purely amorphous and purely crystalline domains and blur surface patterns.

6.4 Controlling surface structures with mechanical treatment

Non-oriented, uniaxially and biaxially oriented semicrystalline PET films showed small but distinctive differences in the surface topography after oxidative plasma treatment. The dimensions of the fibrils were similar in all cases, but fibrils were better defined and more homogeneously distributed in the oriented samples (see fig. 59, 66). Assuming that the fibrils are a consequence of differential etching of domains with differing morphology, it seems that ordered domains are better defined in the oriented samples and this enhances the response to and selectivity of the etching process.

The size and size distribution of the crystalline domains in the semicrystalline oriented and non-oriented films are expected to be very different. This is already evident from the optical appearance of the films: the self-prepared non-oriented PET film is opaque, while biaxially oriented Thermanox is transparent. Opacity in semicrystalline polymers results from scattering of light because of optical heterogeneities in the polymer bulk having dimensions comparable to the wavelength of light. In fact, the radius of the semicrystalline aggregates (spherulites) in PET has been demonstrated to be directly

related to the degree of opacity, being maximum for a spherulite radius between 1.8 and 2 µm [213]. Spherulite radius must be much larger than in the semicrystalline oriented film.

The fibrils in self-prepared uniaxially stretched samples were aligned in rows (65c, f) perpendicular to the stretching direction, demonstrating the possibility of exploiting a mechanical pretreatment to obtain a regular arrangement of surface nanofeatures in a single plasma process. Annealed samples after mechanical treatment did not show aligned fibrils, indicating that the final topography results from mechanical and thermal factors. During annealing different phenomena take place, such as chain relaxation, reorganization of amorphous segments, chain transport, crystallization of amorphous domains, and improvement of crystalline regions. As a result, the microstructure of the PET sample relaxes and evolves into a more stable state closer to thermal equilibrium, forgetting to some extent the mechanical pretreatment.

Fibrils obtained on amorphous uniaxially stretched commercial threads were 2.7 times longer than fibrils obtained from films (stretched or non stretched). Assuming that fibrils occur as a consequence of differential etching of ordered/ amorphous domains during plasma etching, it seems that etching in threads occurs with much higher selectivity. Recently reported work on flow-induced morphology of PET during stretching on monoaxially stretched amorphous PET above T_g claims that crystalline, amorphous and mesomorphic phases coexist in the stretched sample depending on stretching rate, ratio and temperature [214]. At low stretch ratios, isotropic crystallites form and are embedded in an amorphous isotropic matrix. For larger stretching, anisotropic fibrillar domains were found oriented along the stretching direction with crystallites forming a layered structure within the fibrillar domain. This structure is also present in oriented semicrystalline PET, although in this case orientation of the chains is preceded by the breaking of isotropic crystals. At higher stretching ratios, crystallites are oriented and more crystallites develop within the fibrillar domains. A significant proportion of the material still remains non-oriented. This description agrees with the three-phase model proposed for the microstructure of stretched PET fibres in an older study, which included a threadlike interconnected, highly oriented noncrystalline phase coexisting with a more

unoriented amorphous phase and the crystallites (fig. 78) [215]. The stretching ratio of the commercial Goodfellow fibre is expected to be much higher than in the other samples and, therefore, the internal microstructure could be different. This could be the reason for the different fibrillar dimensions observed.

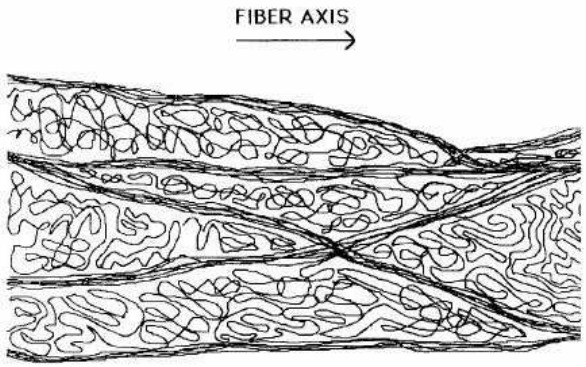

Fig. 78: Schematic of the molecular arrangement in fibres melt-spun at intermediate spinning speeds. The oriented amorphous domains form a fine network. Molecules of the unoriented phase are loosely attached to these oriented domains. (Reprinted from ref. [215] with permission from John Wiley & Sons, Inc.)

Fibrils in biaxially oriented films were interconnected by ridges that seemed oriented in random directions. The PET thread also showed fibrils interconnected by walls. Ridges and walls seem to be etched faster than fibrils, but slower than the surrounding matrix. We hypothesize that these ridges could originate from etching of the anisotropic fibrillar domains (mesomorphic phase). More experiments on stretched samples under different and controlled stretching conditions would be required to prove this hypothesis.

6.5 Surface topography observed on PET etched with other methods

There are a few reports in the literature concerning surface treatment of PET with different etching methods that have also generated a distinct surface topography. This section discusses the reported results and compares them to our observations.

Chemical etching of mono- and biaxially stretched PET films (from amorphous at 100°C) using n-propylamine as solvent has generated a surface macrostructure with interconnected ridges (fig. 79a) [216]. The width of the ridges was about 15 nm and the

mean length between interconnections was about 150 nm. Bigger structures up to 1 µm in length were also observed because dimensions depend on sample history. These dimensions are similar to ours at low etching ratios (about 250 nm in length and 90 nm in width, see fig. 75). In uniaxially stretched samples, ridges were oriented perpendicular to the stretching direction. The orientation improved with the stretching ratio (fig. 79a). Biaxial orientation produced unoriented macrostructure. Ridges have also been observed when wearing the surface of uniaxially and biaxially oriented PET films with an AFM tip in contact mode above a certain load [217, 218]. Inter-ridge spacing was 100 nm and increased up to 200 with increasing AFM tip load. No correlation with the drawing direction was seen in this case, probably because of the small size of the scanned field (1x1micron).

Several authors have reported ridged, bump and short fibrillar structures upon increasing photoablation of PET films using an excimer laser. The feature geometry resembles our obtained structures, but lateral dimensions are bigger (fibril diameter about 1 micron) (fig. 79c-d) [219-222]. Etching rates of ca. 40 nm/min were reported, lower than in our case [219]. The authors attribute the formation of the short fibrils to the crystalline subsurface morphology, since they were not observed in amorphous samples [219-222]. In oriented samples aligned fibrils along the stretching direction were obtained [220]. Other authors attribute ridge formation under similar conditions to the development of cracks within the modified surface [223]. Frozen-in stresses accumulated within the material during stretching then relax due to crack formation when exposed to laser radiation. This could be the reason for ridges appearing in the stretching direction and may also explain the connection lines between fibrils in biaxially oriented samples (fig. 79b). No structures were found in annealed film, since stress relaxation occurs at the annealing temperature. In this model, differences between crystalline and amorphous material were not considered. Moreover, no explanation for the occurrence of fibrils was given. Fibrils in fig. 79b strongly resemble the condensed fibrils resulting from some of our plasma conditions (e.g. fig. 59c).

In atmospheric plasma using Ar as etching gas (etching rate 1 to 4 nm/min), biaxially oriented PET films showed oriented ridges aligned perpendicular to the second drawing direction with ca. 50 nm period and 30 nm width, decorated with globular features on the top that resembled incipient fibrils [224]. In a monoaxially oriented film similar features were obtained. Alignment was less clear, but appeared to be induced perpendicular to the draw direction [224]. It is important to note that etching in atmospheric plasmas is supposed to be only chemical and, therefore, isotropic.

The fact that different etching methods render similar surface structures strongly supports our hypothesis that the structure formation mechanism relies on a pre-existing sample morphology that becomes visible upon etching under our experimental conditions.

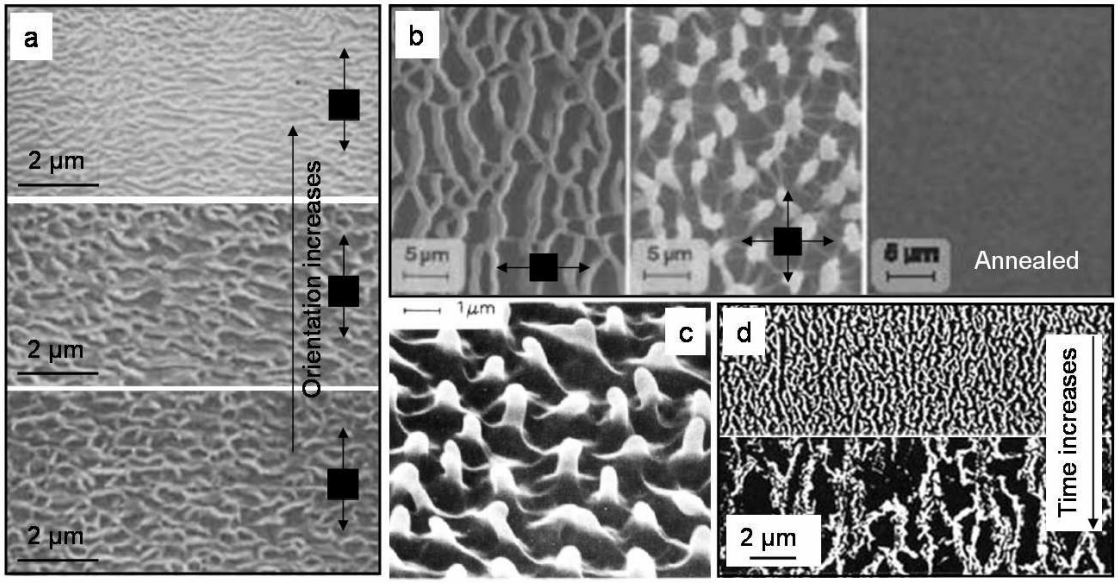

Fig. 79: PET surface morphology after different kinds of treatment: a) Chemical etching with n-propylamine led to the formation of interconnected ridges, which are oriented perpendicular to the uniaxial stretching direction. Structure size decreases with increasing sample orientation. (Reprinted from ref. [216] with permission from John Wiley & Sons, Inc.) b) Exposure to KrF laser radiation generates wall-type structures in uniaxial and nap-type structures in biaxial stretched samples which are perpendicular to the stretching directions. (Reprinted from [225], Copyright 2000, with permission from Elsevier.) In annealed films no structures were observed. (Reprinted from [226] with kind permission of Springer Science+Business Media.) c) Treatment with ArF excimer laser generated fibrillar structures on biaxially oriented PET. (Reprinted with permission from [220]. Copyright 1986 American Chemical Society.) d) Exposure to KrCl excimer lamp formed ridges on biaxially oriented PET films. (Reprinted from ref. [219] with permission from John Wiley & sons, Inc.)

6.6 Influence of polymer chemical structure

The chemical structure of the macromolecule strongly influences the interaction pathways of the plasma species with the material. Different RIE and chemical etching rates are expected from different polymers. According to the literature, polymers with oxygen in the backbone are generally the most susceptible to oxygen plasma degradation, particularly those connected with aliphatic chains [188]. Polyolefins and polymers containing aromatic functionalities are among the most RIE resistant organic materials. The superior etch resistance of aromatic polymers is attributed to the energy stabilizing effect of the phenyl ring as well as its ability to act as free radical sink, which further inhibits oxidative degradation. Siloxane containing materials are probably the less susceptible to degradation with oxygen plasmas. Table 11 summarizes reported etching rates from the literature for different polymers that illustrate these tendencies. Although plasma parameters change for each investigator, it is evident that the etching rate of PMMA is considerably higher than that of PET. PS and PTFE show very slow etching rates and PDMS does not show any appreciable weight loss upon plasma treatment.

Tab. 11: Dependence of etching rate of different polymers on plasma conditions.

Polymer	**Process gas**	**Plasma parameter**	**Etching rate [nm/min]**	**Technique**	**Ref.**
PET	Argon	13.56 MHz, 1.0 mbar, 10 W 13.56 MHz, 0.1 mbar, 10 W	1 4	Scanning force microscopy	[224]
PET	Helium	2.45 GHz, $3 \cdot 10^{-4}$ mbar, 25 W, sample capacitively coupled to a 13.56 MHz rf-potential, dc bias -100 V/ -200 V	4.5 / 6	Atomic force microscopy	[34]
PET	Oxygen Air Nitrogen Argon	13.56 MHz, 80 sccm, $4.13 \cdot 10^{-2}$ mbar, 0.051 W/cm^2	40.2 23.4 10.2 10.2	Weight loss	[142]
PET	Oxygen Argon Hydrogen Nitrogen NH_3	13.56 MHz, 10 sccm, 0.133 mbar, 25 W/50 W/100 W	69.0/38.0/ 340.8; 43.2/7.4/ 69.0; 25.8/69.0/ 125.4; 13.2/55.8/ 73.2; 21.6/34.8/ 73.2	Weight loss	[187]

PET	Oxygen	2.45 GHz, 0.19 mbar, 210W, 70 sccm	130	Weight loss	[227]
PET	Excimer UV radiation*	1 mbar air, λ = 222 nm 25 mW/cm; distance between sample and excimer lamp = 1 cm	≈ 40	Stylus profilometer	[219]
PET	Oxygen	rf, electrodeless discharge process, T ≤ 70°C, 1.3 mbar, 4 sccm/min	≈ 0.29	Weight loss	[228]
PMMA	Oxygen Argon	13.56 MHz, 20 sccm, $4.67 \cdot *10^{-2}$ mbar, 0.75 W/cm^2	550 (thermal bonding) – 2000; 250 (thermal bonding) - 550	Stylus profilometer	[203]
PTFE	Oxygen	rf, electrodeless discharge process, T ≤ 70°C, 1.3 mbar, 4 sccm/min	≈ 0.06	Weight loss	[228]
PMMA	Oxygen	Duo-Plasmaline, 2.45 GHz, 0.15 mbar, power from both ends of quartz tube 600 W + 650 W	≈ 380	Profilometer	[229]
PMMA	Oxygen	rf, electrodeless discharge process, T ≤ 70°C, 1.3 mbar, 4 sccm/min	≈ 0.37	Weight loss	[228]
PMMA	Oxygen	Inductively coupled rf discharge, 13.56 MHz, 100W, 1 min, 40 sccm O_2, pressure unknown	≈ 1330	Weight loss	[230]
PS	Oxygen	rf, electrodeless discharge process, T ≤ 70°C, 1.3 mbar, 4 sccm/min	≈ 0.25	Weight loss	[228]
PDMS	Oxygen	13.56 MHz, 200 W, 0.03 / 0.08 mbar, 60 min	0	Profilometer + optical microscopy (cross sections)	[231]
LDPE	Oxygen	rf, electrodeless discharge process, T ≤ 70°C, 1.3 mbar, 4 sccm/min	≈ 0.56	Weight loss	[228]
PE	Ultraviolet-ozone	fused quartz low-pressure mercury lamp	3 – 27 (depends on crystallinity of sample and distance to lamp)	Weight loss	[208]
PE	CF_4	13.56 MHz, 48-49 W, 0.06-0.07 mbar	3.5 – 5 (depends on crystallinity)	Weight loss	[209]

Using these data and our experimental observations (section 5.3.3), we could not find any correlation between fibril formation, polymer chemistry and etching rate. The analysed polymers also differ in their microstructure (crystallinity and orientation), but this could not be related to fibril formation either. PS, PMMA or PDMS did not form fibrils under our plasma conditions, but other authors have reported similar structures under different plasma conditions (fig. 80) [28, 156, 162]. For comparison, a Thermanox film was treated

under exactly the same conditions as PMMA [28] by P. Munzert. Here, the fibrillar structures look very similar to our results. The dimensions are the same. Plasma parameters obviously also play a major role in the structure formation mechanism.

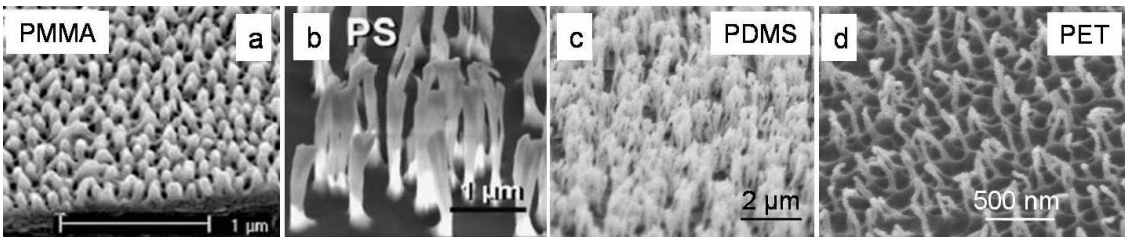

Fig. 80: Different polymers show nanofibrils after plasma treatment. a) PMMA after plasma treatment with a mixture of Ar and O_2. (Reprinted from [31] with permission of the Optical Society of America.) b) PS after Ar+O_2 +CF_4 plasma. ([156]. Copyright Wiley-VCH Verlag GmbH & Co KGaA. Reproduced with permission.) c) PDMS after SF_6 plasma. (Reproduced from ref. [162] with permission from IOP Publishing Ltd.) d) PET treated by P. Munzert (Fraunhofer Institute for Applied Optics and Precision Engineering IOF, Jena) under the same conditions and in the same plasma chamber as a).

6.7 Structure formation mechanism

Different mechanisms of fibril formation in polymers upon plasma treatment have been formulated in the literature. With PET, the following mechanisms have been postulated:

- Differential etching of crystalline and amorphous domains [142]
- Dewetting of a polar fluid film of oxidized low molecular weight fragments in small drops that act as etch masks [24]
- Redeposition of degraded material in atmospheric plasmas [232]

For other polymers further mechanisms have also been discussed:

- Differential etching of crystalline and amorphous domains in cellulose fibres [22] and PP [33]
- Sputtered Al particles from the plasma reactor wall that redeposit onto the surface of the polymer and act as masks during plasma etching of PMMA and PEEK [233]

- Anisotropic ion bombardement of the polymer surface owing to local variation in curvature [156]. Experiments were performed on spin-coated PMMA, PS, PVDF, PEDOT, PPY and photoresist materials
- Spontaneous perturbation and topography formation of a thin film of polymer melt as a consequence of surface instabilities induced by the electric field [153-155]
- No reference to any mechanism [27, 28, 158, 165]

Up to now, none of the reported work has been able to prove their hypothesis with convincing experimental data. Comparison between authors is difficult, since plasma chambers and operating conditions vary from author to author. In addition, the polymer samples used for their analysis are usually commercial and there is no exact information about their thermal and mechanical pretreatment or the presence of additives or fillers.

Under our experimental plasma conditions, the results show a clear correlation between the polymer microstructure and the surface topography that strongly supports the hypothesis of a differential etching mechanism in PET, where the thermal and mechanical pretreatment of the film defines the final topography. Our attempts to analyse the internal structure and composition of the fibrils with TEM could have provided important information to consider or refute the dewetting, redeposition, Al-sputtering or surface-instabilities hypothesis. In the first three cases a different chemical composition of the tip and the rest of the fibril should have been observed. In the last case, chain flow under the electric field should yield fibres formed by highly oriented chains. Unfortunately our TEM results were not clear enough to confirm these ideas.

6.8 Potential of plasma as a templateless patterning technique

Fibrillar structures with different dimensions have been generated by varying the plasma parameters and the thermal and mechanical history of the PET sample. By orienting the polymer film, fibrils could be aligned in a particular direction. Moreover, tilted fibrils

could also be obtained. These results show that plasma etching can be successfully used to create nanofibrilar patterns with controlled dimensions on different materials.

Our results have demonstrated that fibrillar patterns via plasma etching can be obtained on substrates with different geometries, such as curved substrata or threads. Plasma treatment could also be applied to prepatterned films to obtain hierarchically arranged nanofibrils if the prepatterned polymer film has the adequate morphology. Fig. 81 shows SEM images of preliminary experiments on plasma patterning a PET film prepatterned with micropillars obtained by hot embossing. Fibrillar nanotructures were found on the top and on the walls of the micropillars. Similar results were obtained with PDMS films using fluorine plasma under conditions adapted from the literature [48, 164].

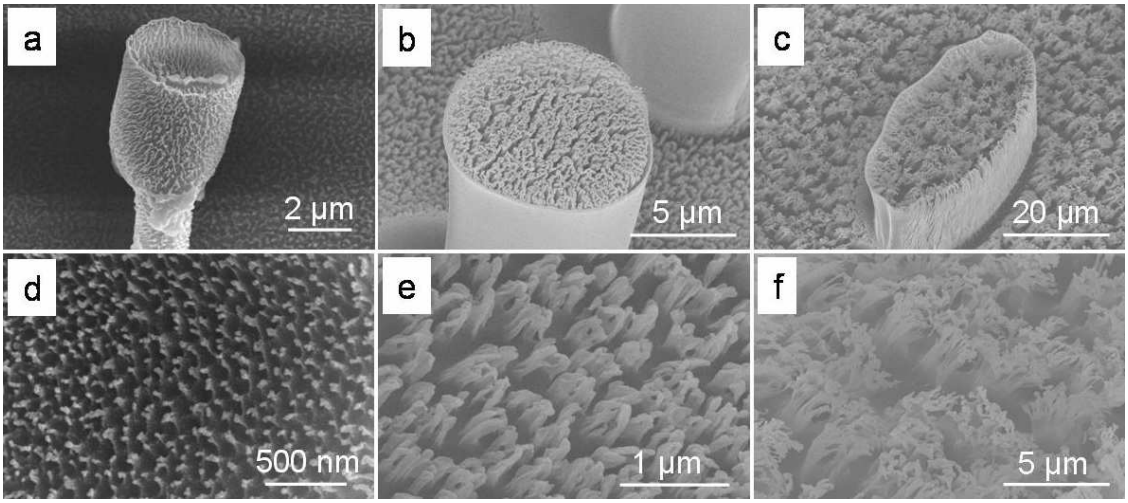

Fig. 81: Hierarchical structures a) on PET generated by hot embossing and posterior oxygen plasma treatment; on PDMS after soft lithography and subsequent b) Ar and then CF_4 plasma, and c) CF_4 + O_2 plasma treatment. d) Higher magnification of a PET micropillar surface, e) and f) higher magnification of b and c.

Plasma treatment is easy, rapid, cheap and fairly flexible. It can pattern large area samples (depending on the size of the electrode) with high aspect ratio fibrils at low cost. None of the available nanopatterning techniques offers such flexibility. A better understanding of the parameters dictating structure development is still required in order to control and predict fibril formation, density and dimensions.

6.9 Properties of fibrillar structures

Oxidative plasma treatment of PET films produces highly hydrophilic surfaces as a consequence of incorporation of polar oxygen atoms in the surface composition and the increase in roughness. Upon storage, hydrophilicity of the surface decreases with time ("hydrophobic recovery") [187, 201, 234].

Perfluorination of PET fibrillar surfaces after 20 minutes plasma treatment made them highly hydrophobic and showed very low adhesion: water droplets effectively rolled off. Slippery surfaces are described by the Cassie-Baxter theory that models surfaces with a topography such that water cannot deeply penetrate and wet: air is trapped in the grooves and the water droplet is suspended across the surface protrusions. Shorter plasma treatment times also created hydrophobic surfaces but the droplet remained attached to the surface (Wenzel regime). The transition from Wenzel to Cassie-Baxter behaviour occurs between 10 and 20 minutes as a consequence of strong collapse of the fibrils that dramatically reduces the solid-liquid contact area (see images fig. 59i, l). Other authors have also found superhydrophobic and slippery surfaces upon plasma treatment and fluorination of PS [27, 158].

Nanofibrillar surfaces showed very low adhesion when compared to flat PET films. The low density of fibrils on the surface accounts for a significant reduction in the effective contact area and, therefore, for low adhesion. Fibrillar surfaces, as in the case of gecko setae, have been shown to increase adhesion as a consequence of the high number of contact elements. However, gecko setae are much more densely packed than our fibrils and they are placed on a compliant substrate which enables good contact with a counter surface. This is not the case for our fibrils, which showed condensation and were attached to a hard PET backing layer.

The fibrillar surfaces displayed higher friction than flat surfaces in the presence of roughness. For friction of non-adhesive surfaces, according to Amontons's law, the friction force is directly proportional to the real area of contact [235]. With increasing

substrate roughness, the contact area between the flat PET film and the substrate decreases, which explains the decrease in friction coefficient of the flat PET film. In contrast, the fibrillar topography allows adaptation to multilevel roughness. Here, the fibrils get stuck between the surface asperities of the rough substrates so movement of the film is hindered. This effect increases with increasing roughness. Therefore, the friction coefficient increased with surface roughness of the substrate and structured samples demonstrated a higher friction coefficient compared to flat analogues.

For other nanostructured materials, measurements of the friction coefficients were also performed. PMMA containing fibres with a diameter of about 250 nm and a length of about 300 nm showed a friction coefficient between 0.25 and 0.33 while flat PMMA exhibited a friction coefficient of 0.63. Measurements were performed with an atomic force microscope (lateral force microscope mode) using a soda lime ball with a radius of 0.5 mm under reciprocating motion with a speed of 1 mm/s and a load of 3 mN [19]. The friction coefficient was calculated from the slope from the plot of friction force versus the applied normal load.

A friction coefficient of greater than 5 at normal loads of 8 kPa were demonstrated for polypropylene fibers with a diameter of 0.6 µm and a length of about 20 µm [236]. Static friction measurements were performed on a traditional pulley apparatus using a glass slide as substrate. The shear load was increased until sliding occurred. The significant increase in friction coefficient compared to the flat analogue (μ = 0.3) is explained by the high compliance of the high aspect ration fibers that allows significant interfacial contact even under light pressure.

Friction experiments performed with vertically aligned carbon nanofibers embedded inside polyurethane (diameter between 50 and 150 nm, length 5 µm) on a custom friction and adhesion measurement system using a glass hemisphere resulted in a friction coefficient up to 1.0. Longer fibers (25 µm) grown on a silicon substrate showed a friction coefficient of 2.2 [237].

Different methods, substrates and substrate roughness were applied to determine the friction coefficient so it is difficult to compare the results. Nevertheless, one trend is obvious. The higher the aspect ratio of the fibrils the higher is the friction coefficient. Fibrils are more compliant and can adapt better to the surface roughness.

A difference in friction coefficient for tilted fibrils was expected, similar to gecko setae [238]. Arrays of angled polypropylene microfibers showed an apparent shear stress of 0.1 and 4.5 N/cm^2 when sliding on a glass surface along and against the microfiber direction [239]. In our samples, no significant variation in friction coefficient with fibril direction could be detected. More measurements are necessary. Presumably, it is better to measure the friction force than the friction coefficient. However, this was not possible with our slide.

7. Summary and Outlook

Oxidative plasma treatment of PET surfaces was used to generate homogeneously distributed nanofibrillar structures with diameters between 15 and 40 nm, interfibrillar distances between 20 and 50 nm and heights up to 1 µm depending on the plasma conditions. Whereas fibril diameter and distance, and therefore fibril density, could not be varied over a large range, fibril length could be modulated between 20 nm and 1 µm by controlling the etching rate by either decreasing the pressure in the plasma chamber or increasing power, sample temperature or treatment time. When the aspect ratio of the fibrils approached three, they started to stick together and formed bundles.

A clear correlation between the polymer microstructure, etching rate and surface topography after plasma treatment was established. Etching proceeded faster in the amorphous sample at short plasma treatment times and low temperatures. Longer plasma treatments resulted in an increase in the electrode temperature and accelerated ageing effects in the amorphous sample. As a consequence of temperature-induced domain densification and ordering processes below T_g, the etching rate of the amorphous sample was slowed down in those conditions. Fibrils were observed in all PET samples, but crystalline samples (either thermally or mechanically induced) showed better defined and homogeneously distributed fibrils at lower plasma treatment times. Uniaxially stretched PET showed fibrils aligned perpendicularly to the stretching direction. Our data firmly support the idea that the fibrillar structure can be controlled to a certain extent by the microstructure of the sample.

PET surfaces exhibited hydrophilic behaviour after oxygen plasma treatment, even at short plasma treatment times. Coating of the surface with a perfluorinated layer led to hydrophobic surfaces. By changing the fibril dimensions with the treatment times, a transition from Wenzel to Cassie-Baxter behaviour, where the drop rolls off the surface, occurred.

The nanofibrillar surfaces showed very low adhesion compared to flat analogues. The low fibril density and the hard backing layer which prevents adaption of the fibrils to the substrate seems to drastically reduce the effective contact area and, therefore, adhesion. In contrast, fibrillar structures displayed higher friction than flat samples on rough surfaces. No influence of the fibril tilt angle on friction behaviour was detected.

There is still a lot that can be done for future experiments on plasma structured PET samples. To confirm our hypothesis of a differential etching mechanism in PET other theories, such as sputtered particles from the plasma reactor wall which could act as an etching mask, should be eliminated by experiment. A systematic investigation of other polymers is necessary to find a consistent explanation for fibril generation by plasma treatment. Additionally, it would be interesting to extend experiments with oriented samples for a better control of the sample microstructure and the fibrillar structure.

The properties of the nanostructured surfaces should be investigated further. Before the samples can be used in applications the mechanical stability of the nanofibrils has to be studied. As the fibrils are very similar to the sub-wavelength structures found in moth eyes [49] and artificial moth eye structures [28, 29] the antireflection properties should be tested as well. Adhesion properties might be enhanced by transferring the nanofibrils to a soft backing layer, for example by spin-coating a thin PET layer on a PDMS surface and subsequent plasma treatment. Further friction measurements are necessary to investigate the influence of fibril length and tilt angle on friction force.

According to the results we obtained in our work, plasma treatment of polymer surfaces promises potential as a technique for templateless patterning. It is easy, rapid, cheap and fairly flexible. It can pattern large area samples (depending on the size of the electrode). Perpendicular and tilted fibrils can be generated on substrates. Curved substrates can also be patterned. It can be combined with other microfabrication techniques (e.g. moulding) to obtain hierarchical structures. This technique can be applied to different materials, but the plasma processing parameters need to be adjusted for each polymer material.

8. Appendices

8.1 Appendix A: Plasma treatment of different PET films

The surface structures of semicrystalline biaxially oriented PET films from different suppliers were compared. All films were plasma treated at 100 W and 0.1 mbar. In figures 82 and 83 the resulting surface structures of Hostaphan RN and Mylar A are depicted.

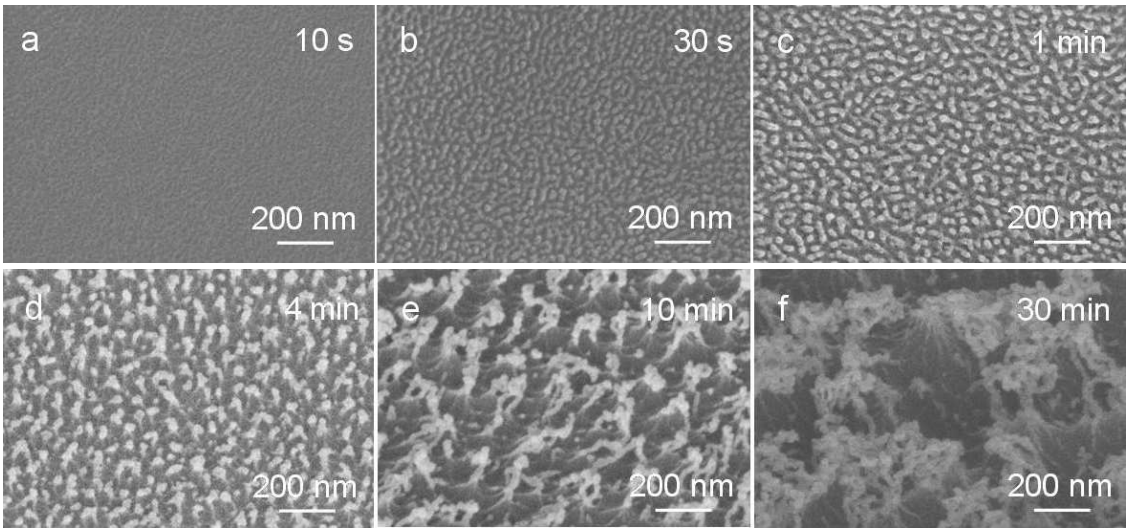

Fig. 82: Commercial PET film Hostaphan-RN treated for a) 10 s, b) 30 s, c) 1 min, d) 4 min, e) 10 min, and f) 30 min at 100 W and 0.1 mbar. Pictures a-c plain view, d-f 30° tilt.

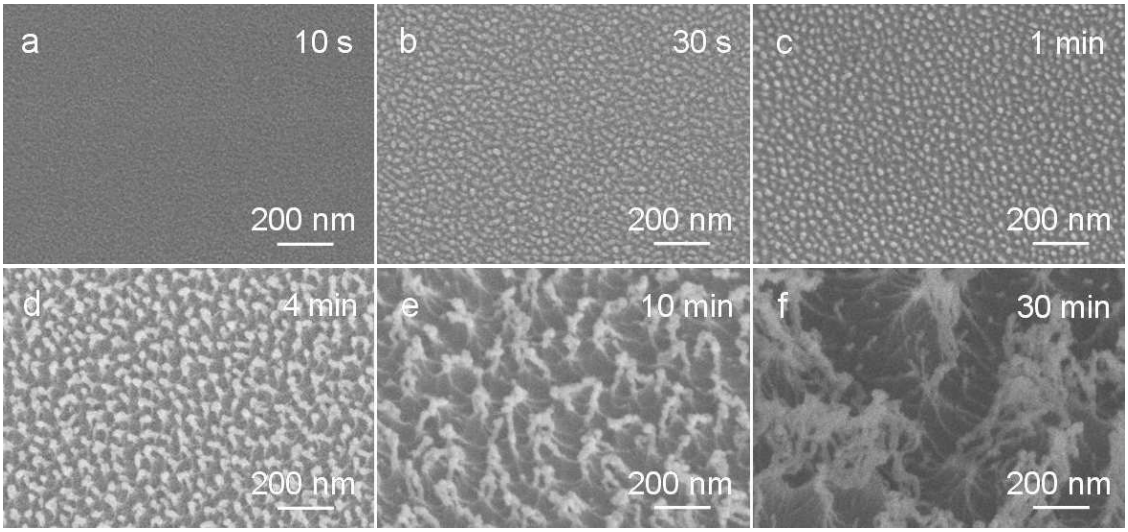

Fig. 83: Commercial PET film Mylar A treated for a) 10 s, b) 30 s, c) 1 min, d) 4 min, e) 10 min, and f) 30 min at 100 W and 0.1 mbar. Pictures a-c plain view, d-f 30° tilt.

8.2 Appendix B: Cross sections of commercial PET threads

A commercial thread was plasma treated between 1 and 20 minutes at 100 W and 0.1 mbar. Subsequently, the threads were coated with 5 nm AuPd, embedded into epofix resin and cut with ultramicrotomy. Cross sections of the thread are depicted in fig. 84.

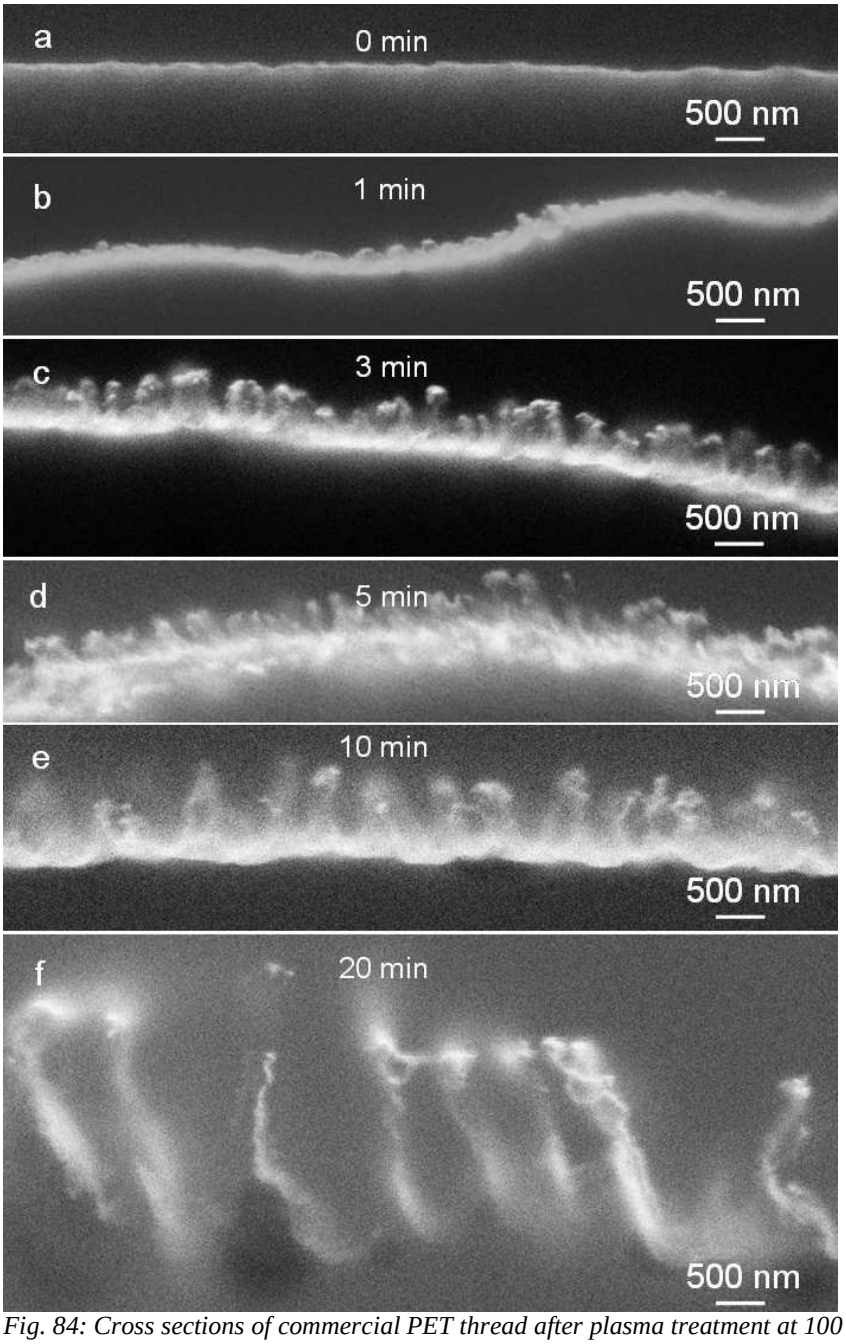

Fig. 84: Cross sections of commercial PET thread after plasma treatment at 100 W and 0.1 mbar.

8.3 Appendix C: Chemical structures of plasma treated polymers

Tab. 12: Chemical structure of plasma treated polymers.

Polymer	Chemical structure
PET	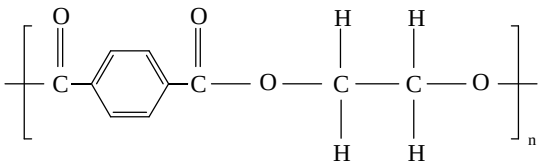
PEN	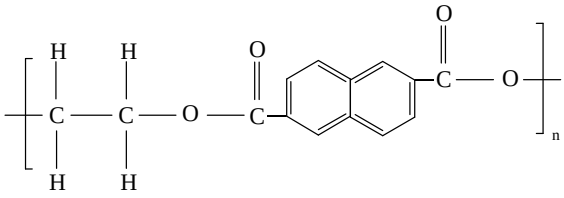
PBT	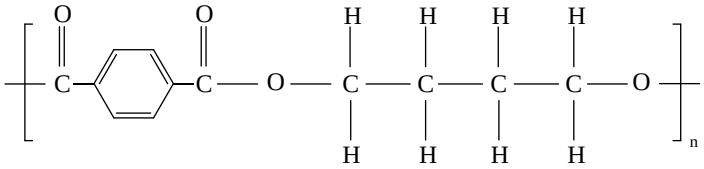
Teflon PFA	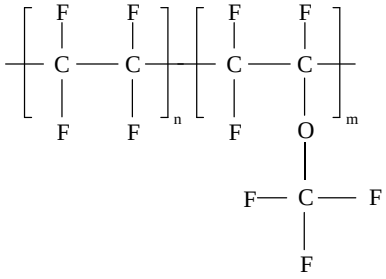
Teflon PEF	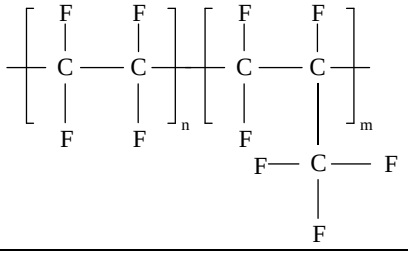

PDMS	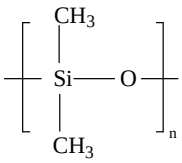
PE	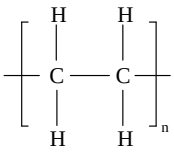
PS	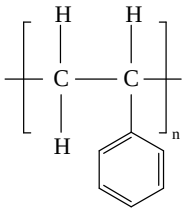
PMMA	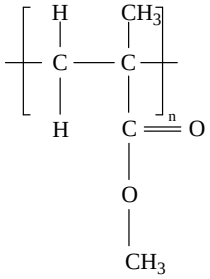

9. References

[1] Hiller U. Untersuchungen zum Feinbau und zur Funktion der Haftborsten von Reptilien. Z. Morph. Tiere 1968;62:307.

[2] Gorb S, Scherge M. Biological microtribology: anisotropy in frictional forces of orthopteran attachment pads reflects the ultrastructure of a highly deformable material. Proceedings of the Royal Society of London Series B-Biological Sciences 2000;267:1239.

[3] Gorb S, Gorb E, Kastner V. Scale effects on the attachment pads and friction forces in syrphid flies. Journal of Experimental Biology 2001;204:1421.

[4] Gorb SN, Beutel RG, Gorb EV, Jiao YK, Kastner V, Niederegger S, Popov VL, Scherge M, Schwarz U, Votsch W. Structural design and biomechanics of friction-based releasable attachment devices in insects. Integrative and Comparative Biology 2002;42:1127.

[5] Autumn K, Peattie AM. Mechanisms of adhesion in geckos. Integrative and Comparative Biology 2002;42:1081.

[6] del Campo A, Arzt E. Design parameters and current fabrication approaches for developing bioinspired dry adhesives. Macromolecular Bioscience 2007;7:118.

[7] Crosby AJ, Hageman M, Duncan A. Controlling polymer adhesion with "pancakes". Langmuir 2005;21:11738.

[8] Glassmaker NJ, Jagota A, Hui CY, Kim J. Design of biomimetic fibrillar interfaces: 1. Making contact. J Roy Soc Interface 2004;1:23.

[9] Greiner C, del Campo A, Arzt E. Adhesion of bioinspired micropatterned surfaces: Effects of pillar radius, aspect ratio and preload. Langmuir 2007;23:3495.

[10] Lamblet M, Verneuil E, Vilmin T, Buguin A, Solberzan P, Léger L. Adhesion Enhancement through Micropatterning at Polydimethylsiloxane-Acrylic Adhesive Interfaces. Langmuir 2007;23:6966.

[11] Geim AK, Dubonos SV, Grigorieva IV, Novoselov KS, Zhukov AA, Shapoval SY. Microfabricated adhesive mimicking gecko foot-hair. Nature Materials 2003;2:461.

[12] Aksak B, Murphy MP, Sitti M. Adhesion of Biologically Inspired Vertical and Angled Polymer Microfiber Arrays. Langmuir 2007;23:3322.

[13] Yurdumakan B, Raravikar NR, Ajayan PM, Dhinojwala A. Synthetic gecko foot-hairs from multiwalled carbon nanotubes. Chemical Communications 2005:3799.

[14] Ge L, Sethi S, Ci L, Ajayan PM, Dhinojwala A. Carbon nanotube-based synthetic gecko tapes. P Natl Acad Sci USA 2007;104:10792.

[15] Zhao Y, Tong T, Delzeit L, Kashani A, Meyyappan M, Majumdar A. Interfacial energy and strength of multiwalled-carbon-nanotube-based dry adhesive. J Vac Sci Technol B 2006;24:331.

[16] Qu L, Dai L, Stone M, Xia Z, Wang ZL. Carbon Nanotube Arrays with Strong Shear Binding-On and Easy Normal Lifting-Off. Science 2008;322:238.

[17] Federle W. Why are so many adhesive pads hairy? The Journal of Experimental Biology 2006;209:2611.

[18] Jeong HE, Lee SH, Kim JK, Suh KY. Nanoengineered multiscale hierarchical structures with tailored wetting properties. Langmuir 2006;22:1640.

[19] Yoon ES, Singh RA, Kong H, Kim B, Kim DH, Jeong HE, Suh KY. Tribological properties of bio-mimetic nano-patterned polymeric surfaces on silicon wafer. Tribology Letters 2006;21:31.

[20] d'Agostino R, Favia P, Oehr C, Wertheimer MR. Plasma Processes and Polymers. Wiley VCH 2005.

[21] Liston EM, Martinu L, Wertheimer MR. Plasma surface modification of polymers for improved adhesion: a critical review. Journal of Adhesion Science and Technology 1993;7:1091.

[22] Balu B, Breedveld V, Hess DW. Fabrication of "Roll-off" and "Sticky" Superhydrophobic Cellulose Surfaces via Plasma Processing. Langmuir 2008;24:4785.

[23] Beake BD, Ling JSG, Leggett GJ. Scanning force microscopy investigation of poly(ethylene terephthalate) modified by argon plasma treatment. Journal of Materials Chemistry 1998;8:1735.

[24] Powell HM, Lannutti JJ. Nanofibrillar surfaces via reactive ion etching. Langmuir 2003;19:9071.

[25] Schönberger W, Gerlach G, Fahland M, Munzert P, Schulz U. Großflächige Entspiegelung von Kunststofffolien durch Plasma- und Ionenbehandlung. 17. Neues Dresdner Vakuumtechnisches Kolloquium; Beschichtung, Modifizierung und Charakterisierung von Polymeroberflächen. Dresden, 2009.

[26] Di Mundo R, Palumbo F, d'Agostino R. Nanotexturing of Polystyrene Surface in Fluorocarbon Plasmas: From Sticky to Slippery Superhydrophobicity. Langmuir 2008;24:5044.

[27] Di Mundo R, De Benedictis V, Palumbo F, d'Agostino R. Fluorocarbon plasmas for nanotexturing of polymers: A route to water-repellent antireflective surfaces. Applied Surface Science 2009;255:5461.

[28] Kaless A, Schulz U, Kaiser N. Self-organized antireflective nanostructures on PMMA by ion etching. In: Angela D, Roland G, Lingli W, editors, vol. 5965: SPIE, 2005. p.59651N.

[29] Kaless A, Schulz U, Munzert P, Kaiser N. NANO-motheye antireflection pattern by plasma treatment of polymers. Surface and Coatings Technology 2005;200:58.

[30] Leitel R, Kaless A, Schulz U, Kaiser N. Broadband Antireflective Structures on PMMA by Plasma Treatment. Plasma Processes and Polymers 2007;4:S878.

[31] Schulz U, Munzert P, Leitel R, Wendling I, Kaiser N, Tunnermann A. Antireflection of transparent polymers by advanced plasma etching procedures. Opt. Express 2007;15:13108.

[32] Munzert P, Schulz U, Kaiser N. Hocheffektive Entspiegelung von Kunststoffoptiken durch Plasmaätzen. 17. Neues Dresdner Vakuumtechnisches Kolloquium; Beschichtung, Modifizierung und Charakterisierung von Polymeroberflächen. Dresden, 2009.

[33] Youngblood JP, McCarthy TJ. Ultrahydrophobic polymer surfaces prepared by simultaneous ablation of polypropylene and sputtering of poly(tetrafluoroethylene) using radio frequency plasma. Macromolecules 1999;32:6800.

[34] Coen MC, Lehmann R, Groening P, Schlapbach L. Modification of the micro- and nanotopography of several polymers by plasma treatments. Applied Surface Science 2003;207:276.

[35] Morra M, Occhiello E, Garbassi F. Surface Characterization of Plasma-treated PTFE. Surf. Interface Anal. 1990;16:412.

[36] Morra M, Occhiello E, Garbassi F. Contact-Angle Hysteresis in Oxygen Plasma Treated Poly(Tetrafluoroethylene). Langmuir 1989;5:872.

[37] Minko S, Muller M, Motornov M, Nitschke M, Grundke K, Stamm M. Two-Level Structured Self-Adaptive Surfaces with Reversibly Tunable Properties. J. Am. Chem. Soc. 2003;125:3896.

[38] Manca M, Cortese B, Viola I, Aricò AS, Cingolani R, Gigli G. Influence of Chemistry and Topology Effects on Superhydrophobic CF4-Plasma-Treated Poly(dimethylsiloxane) (PDMS). Langmuir 2008;24:1833.

[39] Tsougeni K, Tserepi A, Boulousis G, Constantoudis V, Gogolides E. Control of Nanotexture and Wetting Properties of Polydimethylsiloxane from Very Hydrophobic to Super-Hydrophobic by Plasma Processing. Plasma Processes and Polymers 2007;4:398.

[40] Tsougeni K, Tserepi A, Boulousis G, Constantoudis V, Gogolides E. Tunable poly(dimethylsiloxane) topography in O_2 or Ar plasmas for controlling surface wetting properties and their ageing. Japanese Journal of Applied Physics Part 1-Regular Papers Brief Communications & Review Papers 2007;46:744.

[41] Tserepi A, Gogolides E, Tsougeni K, Constantoudis V, Valamontes ES. Tailoring the surface topography and wetting properties of oxygen-plasma treated polydimethylsiloxane. Journal of Applied Physics 2005;98:113502.

[42] Schweikart A, Fery A. Controlled wrinkling as a novel method for the fabrication of patterned surfaces. Microchimica Acta 2009;165:249.

[43] Schweikart A, Horn A, Böker A, Fery A. Oberflächenstrukturierung durch kontrollierte Faltenbildung: Eine Alternative zu lithographischen Verfahren? 17. Neues Dresdner Vakuumtechnisches Kolloquium; Beschichtung, Modifizierung und Charakterisierung von Polymeroberflächen. Dresden, 2009.

[44] Tserepi A, Vlachopoulou ME, Gogolides E. Nanotexturing of poly(dimethylsiloxane) in plasmas for creating robust super-hydrophobic surfaces. Nanotechnology 2006;17:3977.

[45] Vlachopoulou ME, Petrou PS, Kakabakos SE, Tserepi A, Gogolides E. High-aspect-ratio plasma-induced nanotextured poly(dimethylsiloxane) surfaces with enhanced protein adsorption capacity. J. Vac. Sci. Technol. B 2008;26:2543.

[46] Szmigiel D, Hibert C, Bertsch A, Pamua E, Domaski K, Grabiec P, Prokaryn P, Scisowska-Czarnecka A, Pytycz B. Fluorine-Based Plasma Treatment of Biocompatible Silicone Elastomer: The Effect of Temperature on Etch Rate and Surface Properties. Plasma Processes and Polymers 2008;5:246.

[47] Szmigiel D, Domanski K, Prokaryn P, Grabiec P, Sobczak JW. The effect of fluorine-based plasma treatment on morphology and chemical surface composition of biocompatible silicone elastomer. Applied Surface Science 2006;253:1506.

[48] Chen M-H, Hsu T-H, Chuang Y-J, Chen P-H, Tseng F-G. The Preparation of Self-formed PDMS Nanostructures by RIE Etching. Proceedings of the 2nd IEEE

International Conference on Nano/Micro Engineered and Molecular Systems 2007:977.

[49] Bernhard CG. Structural and functional adaption in a visual system. Endeavour 1967;26:79.

[50] Clapham PB, Hutley MC. Reduction of Lens Reflection by Moth Eye Principle. Nature 1973;244:281.

[51] Scherge M, Gorb S. Biological Micro- and Nanotribology. Berlin: Springer, 2001. p.82.

[52] Baum C, Meyer W, Stelzer R, Fleischer LG, Siebers D. Average nanorough skin surface of the pilot whale (Globicephala melas, Delphinidae): considerations on the self-cleaning abilities based on nanoroughness. Mar. Biol. 2002;140:653.

[53] Stavenga DG, Foletti S, Palasantzas G, Arikawa K. Light on the moth-eye corneal nipple array of butterflies. Proc. R. Soc. B-Biol. Sci. 2006;273:661.

[54] Bechert DW, Bruse M, Hage W. Experiments with three-dimensional riblets as an idealized model of shark skin. Exp. Fluids 2000;28:403.

[55] Gorb SN. Functional Surfaces in Biology: Mechanisms and Applications: Taylor & Francis Group, 2006.

[56] Barthlott W, Neinhuis C. Purity of the sacred lotus, or escape from contamination in biological surfaces. Planta 1997;202:1.

[57] Bhushan B, Jung YC. Micro- and nanoscale characterization of hydrophobic and hydrophilic leaf surfaces. Nanotechnology 2006;17:2758.

[58] Burton Z, Bhushan B. Surface characterization and adhesion and friction properties of hydrophobic leaf surfaces. Ultramicroscopy 2006;106:709.

[59] Wagner T, Neinhuis C, Barthlott W. Wettability and contaminability of insect wings as a function of their surface sculptures. Acta Zool. 1996;77:213.

[60] Gorb E, Haas K, Henrich A, Enders S, Barbakadze N, Gorb S. Composite structure of the crystalline epicuticular wax layer of the slippery zone in the pitchers of the carnivorous plant Nepenthes alata and its effect on insect attachment. Journal of Experimental Biology 2005;208:4651.

[61] Koch K, Bhushan B, Barthlott W. Multifunctional surface structures of plants: An inspiration for biomimetics. Prog. Mater. Sci. 2009;54:137.

[62] Stork NE. Experimental analysis of adhesion of Chrysolina polita (Chrysomelidae, Coleoptera) on a variety of surfaces. Journal of Experimental Biology 1980;88:91.

[63] Bauchhenss E. Pulvilli of Calliphora erythrocephala (Diptera, Brachycera) as adhesive organs. Zoomorphologie 1979;93:99.

[64] Walker G, Yule AB, Ratcliffe J. The adhesive organ of the blowfly, Calliphora vomitoria: a functional approach (Diptera, Calliphoridae). Journal of Zoology 1985;205:297.

[65] Gorb SN. Origin and pathway of the epidermal secretion in the damselfly head-arresting system (Insecta : Odonata). J. Insect Physiol. 1998;44:1053.

[66] Homann H. Haften Spinnen an einer Wasserhaut. Naturwissenschaften 1957;44:318.

[67] Ruibal R, Ernst V. Structure of Digital Setae of Lizards. Journal of Morphology 1965;117:271.

[68] Irschick DJ, Austin CC, Petren K, Fisher RN, Losos JB, Ellers O. A comparative analysis of clinging ability among pad-bearing lizards. Biological Journal of the Linnean Society 1996;59:21.

[69] Autumn K, Liang YA, Hsieh ST, Zesch W, Chan WP, Kenny TW, Fearing R, Full RJ. Adhesive force of a single gecko foot-hair. Nature 2000;405:681.

[70] Autumn K, Sitti M, Liang YCA, Peattie AM, Hansen WR, Sponberg S, Kenny TW, Fearing R, Israelachvili JN, Full RJ. Evidence for van der Waals adhesion in gecko setae. Proceedings of the National Academy of Sciences of the United States of America 2002;99:12252.

[71] Huber G, Gorb SN, Spolenak R, Arzt E. Resolving the nanoscale adhesion of individual gecko spatulae by atomic force microscopy. Biology Letters 2005;1:2.

[72] Autumn K. Properties, Principles, and Parameter of the Gecko Adhesive System. In: Smith AM, Callow JA, editors. Biological Adhesives. Berlin: Springer, 2006. p.225.

[73] Liang YA, Autumn K, Hsieh ST, Zesch W, Chan WP, Fearing RS, Full RJ, Kenny TW. Adhesion Force Measurements on Single Gecko Setae. Solid-State Sensor and Actuator Workshop. Hilton Head Island, South Carolina, 2000.

[74] Hansen WR, Autumn K. Evidence for self-cleaning in gecko setae. Proceedings of the National Academy of Sciences of the United States of America 2005;102:385.

[75] Arzt E, Gorb S, Spolenak R. From micro to nano contacts in biological attachment devices. Proceedings of the National Academy of Sciences of the United States of America 2003;100:10603.

[76] Wallraff GM, Hinsberg WD. Lithographic imaging techniques for the formation of nanoscopic features. Chemical Reviews 1999;99:1801.

[77] Rothschild M. Projection optical lithography. Mater. Today 2005;8:18.

[78] Brunner TA. Why optical lithography will live forever. J. Vac. Sci. Technol. B 2003:2632.

[79] Gil D, Brunner TA, Fonseca C, Seong N, Streefkerk B, Wagner C, Stavenga M. Immersion lithography: New opportunities for semiconductor manufacturing. J. Vac. Sci. Technol. B 2004:3431.

[80] Willson CG, Trinque BC. The evolution of materials for the photolithographic process. J. Photopolym. Sci. Technol. 2003;16:621.

[81] Ito T, Okazaki S. Pushing the limits of lithography. Nature 2000;406:1027.

[82] del Campo A, Arzt E. Fabrication approaches for generating complex micro- and nanopatterns on polymeric surfaces. Chemical Reviews 2008;108:911.

[83] Teh WH, Durig U, Salis G, Harbers R, Drechsler U, Mahrt RF, Smith CG, Guntherodt HJ. SU-8 for real three-dimensional subdiffraction-limit two-photon microfabrication. Appl. Phys. Lett. 2004;84:4095.

[84] Teh WH, Dürig U, Drechsler U, Smith CG, Güntherodt HJ. Effect of low numerical-aperture femtosecond two-photon absorption on (SU-8) resist for ultrahigh-aspect-ratio microstereolithography. J. Appl. Phys. 2005;97:11.

[85] Sun HB, Kawata S. Two-photon photopolymerization and 3D lithographic microfabrication. NMR, 3D Analysis, Photopolymerization. Advances in Polymer Science, vol. 170. Berlin: Springer-Verlag Berlin, 2004. p.169.

[86] Juodkazis S, Mizeikis V, Seet KK, Miwa M, Misawa H. Two-photon lithography of nanorods in SU-8 photoresist. Nanotechnology 2005;16:846.

[87] Houbertz R, Schulz J, Frohlich L, Domann G, Popall M, Serbin J, Chichkov B. Inorganic-organic hybrid materials for real 3-D sub-mu m lithography. In: Chrisey DB, Dinescu M, Boyd IW, Rode AV, editors. Symposium on Advanced Optical Processing of Materials held at the MRS Spring Meeting. San Francisco, Ca: Materials Research Society, 2003. p.175.

[88] LaFratta CN, Baldacchini T, Farrer RA, Fourkas JT, Teich MC, Saleh BEA, Naughton MJ. Replication of two-photon-polymerized structures with extremely high aspect ratios and large overhangs. Journal of Physical Chemistry B 2004;108:11256.

[89] Elsner H, Meyer HG. Nanometer and high aspect ratio patterning by electron beam lithography using a simple DUV negative tone resist. Microelectron. Eng. 2000;57-58:291.

[90] Van Kan JA, Bettiol AA, Ansari K, Teo EJ, Sum TC, Watt F. Proton beam writing. Int. J. Nanotechnol. 2004;1:464.

[91] Ansari K, van Kan JA, Bettiol AA, Watt F. Fabrication of high aspect ratio 100 nm metallic stamps for nanoimprint lithography using proton beam writing. Appl. Phys. Lett. 2004;85:476.

[92] Munnik F, Benninger F, Mikhailov S, Bertsch A, Renaud P, Lorenz H, Gmur M. High aspect ratio, 3D structuring of photoresist materials by ion beam LIGA. Microelectron. Eng. 2003;67-68:96.

[93] Osipowicz T, van Kan JA, Sum TC, Sanchez JL, Watt F. The use of proton microbeams for the production of microcomponents. Nucl. Instrum. Methods B 2000;161:83.

[94] van Kan JA, Bettiol AA, Watt F. Three-dimensional nanolithography using proton beam writing. Appl. Phys. Lett. 2003;83:1629.

[95] Soh HT, Guarini KW, Quate CF. Scanning Probe Microscopy. New York: Kluwer Academic Publishers, 2001.

[96] Vasile MJ, Nassar R, Xie JS. Focused ion beam technology applied to microstructure fabrication. J. Vac. Sci. Technol. B 1998;16:2499.

[97] Fu Y, Bryan NKA. Fabrication and characterization of slanted nanopillars array. J. Vac. Sci. Technol. B 2005;23:984.

[98] Fujii T, Iwasaki K, Munekane M, Takeuchi T, Hasuda M, Asahata T, Kiyohara M, Kogure T, Kijima Y, Kaito T. A nanofactory by focused ion beam. J. Micromech. Microeng., 2005. p.S286.

[99] Gratson GM, Xu MJ, Lewis JA. Microperiodic structures - Direct writing of three-dimensional webs. Nature 2004;428:386.

[100] Smay JE, Gratson GM, Shepherd RF, Cesarano J, Lewis JA. Directed colloidal assembly of 3D periodic structures. Adv. Mater. 2002;14:1279.

[101] Therriault D, White SR, Lewis JA. Chaotic mixing in three-dimensional microvascular networks fabricated by direct-write assembly. Nat. Mater. 2003;2:265.

[102] Schift H, Heyderman LJ, Padeste C, Gobrecht J. Chemical nano-patterning using hot embossing lithography. Microelectron. Eng. 2002;61-62:423.

[103] Chou SY, Krauss PR, Renstrom PJ. Imprint of sub-25nm vias and trenches in polymers. Appl. Phys. Lett. 1995;67:3114.

[104] Bailey TC, Resnick DJ, Mancini D, Nordquist KJ, Dauksher WJ, Ainley E, Talin A, Gehoski K, Baker JH, Choi BJ, Johnson S, Colburn M, Meissl M, Sreenivasan SV, Ekerdt JG, Willson CG. Template fabrication schemes for step and flash imprint lithography. Microelectron. Eng. 2001;61-62:461.

[105] Dauksher WJ, Nordquist KJ, Mancini DP, Resnick DJ, Baker JH, Hooper AE, Talin AA, Bailey TC, Lemonds AM, Sreenivasan SV, Ekerdt JG, Willson CG. Characterization of and imprint results using indium tin oxide-based step and flash imprint lithography templates. J. Vac. Sci. Technol. B 2002;20:2857.

[106] Mancini DP, Gehoski KA, Ainley E, Nordquist KJ, Resnick DJ, Bailey TC, Sreenivasan SV, Ekerdt JG, Willson CG. Hydrogen silsesquioxane for direct electron-beam patterning of step and flash imprint lithography templates. J. Vac. Sci. Technol. B 2002;20:2896.

[107] Resnick DJ, Mancini D, Dauksher WJ, Nordquist K, Bailey TC, Johnson S, Sreenivasan SV, Ekerdt JG, Willson CG. Improved step and flash imprint lithography templates for nanofabrication. Microelectron. Eng. 2002;69:412.

[108] Xia YN, Whitesides GM. Soft lithography. Angew. Chem., Int. Ed. 1998;37:551.

[109] Kim YS, Suh KY, Lee HH. Fabrication of three-dimensional microstructures by soft molding. Appl. Phys. Lett. 2001;79:2285.

[110] Suh KY, Choi SJ, Baek SJ, Kim TW, Langer R. Observation of high-aspect-ratio nanostructures using capillary lithography. Adv. Mater. 2005;17:560.

[111] Suh KY, Jeong HE, Park JW, Lee SF, Kim JK. Fabrication of high aspect ratio nanostructures using capillary force lithography. Korean Journal of Chemical Engineering 2006;23:678.

[112] Suh KY, Kim YS, Lee HH. Capillary force lithography. Adv. Mater. 2001;13:1386.

[113] Suh KY, Lee HH. Capillary force lithography: Large-area patterning, self-organization, and anisotropic dewetting. Adv. Funct. Mater. 2002;12:405.

[114] Khang DY, Lee HH. Pressure-assisted capillary force lithography. Adv. Mater. 2004;16:176.

[115] Junarsa I, Nealeya PF. Fabrication of masters for nanoimprint, step and flash, and soft lithography using hydrogen silsesquioxane and x-ray lithography. J. Vac. Sci. Technol. B 2004;22:2685.

[116] Turner R, Desta Y, Kelly K, Zhang J, Geiger E, Cortez S, Mancini DC. Tapered LIGA HARMs. J. Micromech. Microeng. 2003;13:367.

[117] Greiner C, del Campo A, Arzt E. Adhesion of Bioinspired Micropatterned Surfaces: Effects of Pillar Radius, Aspect Ratio, and Preload. Langmuir 2007;23:3495.

[118] Huang XD, Bao LR, Cheng X, Guo LJ, Pang SW, Yee AF. Reversal imprinting by transferring polymer from mold to substrate. J. Vac. Sci. Technol. B 2002;20:2872.

[119] Borzenko T, Tormen M, Schmidt G, Molenkamp LW, Janssen H. Polymer bonding process for nanolithography. Appl. Phys. Lett. 2001;79:2246.

[120] Zhao XM, Xia YN, Whitesides GM. Soft lithographic methods for nano-fabrication. J. Materi. Chem. 1997;7:1069.

[121] Zhao XM, Xia YN, Whitesides GM. Fabrication of three-dimensional micro-structures: Microtransfer molding. Adv. Mater. 1996;8:837.

[122] Childs WR, Nuzzo RG. Patterning of thin-film microstructures on non-planar substrate surfaces using decal transfer lithography. Adv. Mater. 2004;16:1323.

[123] Childs WR, Nuzzo RG. Decal transfer microlithography: A new soft-lithographic patterning method. J. Am. Chem. Soc. 2002;124:13583.

[124] Schäffer E, Thurn-Albrecht T, Russell TP, Steiner U. Electrically induced structure formation and pattern transfer. Nature 2000;403:874.

[125] Schaffer E, Thurn-Albrecht T, Russell TP, Steiner U. Electrohydrodynamic instabilities in polymer films. Europhysics Letters 2001;53:518.

[126] Morariu MD, Voicu NE, Schaffer E, Lin ZQ, Russell TP, Steiner U. Hierarchical structure formation and pattern replication induced by an electric field. Nature Materials 2003;2:48.

[127] Xiang HQ, Lin Y, Russell TP. Electrically induced patterning in block copolymer films. Macromolecules 2004;37:5358.

[128] Hui C-Y, Jagota A, Shen L, Rajan A, Glassmaker N, Tang T. Design of bio-inspired fibrillar interfaces for contact and adhesion — theory and experiments. Journal of Adhesion Science and Technology 2007;21:1259.

[129] Gupta VB, Bashir Z. PET Fibers, Films, and Bottles. In: Fakirov S, editor. Handbook of Thermoplastic Polyesters, vol. 1. Weinheim: Wiley-VCH, 2002. p.317.

[130] Brooks DW, Giles GA. Introduction. In: Brooks DW, Giles GA, editors. PET Packaging Technology. Sheffield: Sheffield Academic Press, 2002. p.1.

[131] Aharoni SM. Industrial-Scale Production of Polyesters, Especially Poly(ethylene terephthalate). In: Fakirov S, editor. Handbook of Thermoplastic Polymers, vol. 1. Weinheim: Wiley-VHC, 2002. p.59.

[132] Daubeny RdP, Bunn CW. The Crystal Structure of Polyethylene Terephthalate. Proceedings of the Royal Society of London. Series A, Mathematical and Physical Sciences 1954;226:531.

[133] Gupta VB, Bashir Z. PET Fibers, Films, and Bottles. In: Fakirov S, editor. Handbook of Thermoplastic Polyesters, vol. 1. Weinheim: Wiley-VCH, 2002. p.363.

[134] http://www.m-petfilm.com/upload/Europe_216GER.pdf http://www.m-petfilm.com/upload/Europe_181GER.pdf. Mitsubishi Polyester Film, 2009.

[135] Gupta VB, Bashir Z. PET Fibers, Films, and Bottles. In: Fakirov S, editor. Handbook of Thermoplastic Polyesters, vol. 1. Weinheim: Wiley-VCH, 2002. p.328.

[136] Gupta VB, Bashir Z. PET Fibers, Films, and Bottles. In: Fakirov S, editor. Handbook of Thermoplastic Polyesters, vol. 1. Weinheim: Wiley-VCH, 2002. p.329.

[137] Denes FS, Manolache S. Macromolecular plasma-chemistry: an emerging field of polymer science. Progress in Polymer Science 2004;29:815.

[138] Meichsner J, Nitschke M, Rochotzki R, Zeuner M. Fundamental investigations in plasma modification of polymers. Surface and Coatings Technology 1995;74-75:227.

[139] Liston EM. Plasma Treatment for Improved Bonding: A Review. The Journal of Adhesion 1989;30:199

[140] Gomathi N, Sureshkumar A, Neogi S. RF plasma-treated polymers for biomedical applications. Current Science 2008;94:1478.

[141] Rogers BR, Cale TS. Plasma processes in microelectronic device manufacturing. Vacuum 2002;65:267.

[142] Cross JH, Lemay MW, McClure DJ. Texturing of Poly(ethylene-terephthalate) film surfaces by sputter etching. Journal of Vacuum Science & Technology a-Vacuum Surfaces and Films 1985;3:495.

[143] Xie YB, Sproule T, Li Y, Powell H, Lannutti JJ, Kniss DA. Nanoscale modifications of PET polymer surfaces via oxygen-plasma discharge yield minimal changes in attachment and growth of mammalian epithelial and mesenchymal cells in vitro. Journal of Biomedical Materials Research 2002;61:234.

[144] Teshima K, Sugimura H, Inoue Y, Takai O, Takano A. Ultra-Water-Repellent Poly(ethylene terephthalate) Substrates. Langmuir 2003;19:10624.

[145] Teshima K, Sugimura H, Inoue Y, Takai O, Takano A. Wettablity of Poly(ethylene terephthalate) Substrates Modified by a Two-Step Plasma Process: Ultra Water Repellent Surface Fabrication. Chemical Vapor Deposition 2004;10:295.

[146] Teshima K, Sugimura H, Takano A, Inoue Y, Takai O. Ultrahydrophobic/Ultrahydrophilic Micropatterning on a Polymeric Substrate. Chemical Vapor Deposition 2005;11:347.

[147] Leitel R, Kaless A, Schulz U, Kaiser N. Broadband Antireflective Structures on PMMA by Plasma Treatment. Plasma Processes and Polymers 2007;4:S878.

[148] Leitel R, Schulz U, Kaiser N, Tunnermann A. Stochastic subwavelength structures on poly(methyl methacrylate) surfaces for antireflection generated by plasma treatment. Applied Optics 2008;47:C143.

[149] Fraunhofer Institut für angewandte Optik und Feinmechanik. http://www.iof.fraunhofer.de/departments/optical-coatings/plastics/index_d.html.

[150] Vourdas N, Tserepi A, Gogolides E. Nanotextured super-hydrophobic transparent poly(methyl methacrylate) surfaces using high-density plasma processing. Nanotechnology 2007;18.

[151] Nitschke M, Konig U, Lappan U, Minko S, Simon F, Zschoche S, Werner C. Low pressure plasma-based approaches to fluorocarbon polymer surface modification. Journal of Applied Polymer Science 2007;103:100.

[152] Liu C, Arnell RD, Gibbons AR, Green SM, Ren L, Tong J. Surface modification of PTFE by plasma treatment. Surface Engineering 2000;16:215.

[153] Northen MT, Turner KL. A batch fabricated biomimetic dry adhesive. Nanotechnology 2005;16:1159.

[154] Northen MT, Turner KL. Meso-scale adhesion testing of integrated micro- and nano-scale structures. Sensors and Actuators a-Physical 2006;130:583.

[155] Northen MT, Turner KL. Batch fabrication and characterization of nanostructures for enhanced adhesion. Current Applied Physics 2006;6:379.

[156] Morber JR, Wang X, Liu J, Snyder RL, Wang ZL. Wafer-Level Patterned and Aligned Polymer Nanowire/Micro- and Nanotube Arrays on any Substrate. Adv. Mat. 2009;21:2072.

[157] Bradley RM, Harper JME. Theory of ripple topography induced by ion-bombardment. Journal of Vacuum Science & Technology a-Vacuum Surfaces and Films 1988;6:2390.

[158] DiMundo R, Palumbo F, d'Agostino R. Nanotexturing of Polystyrene Surface in Fluorocarbon Plasmas: From Sticky to Slippery Superhydrophobicity. Langmuir 2008;24:5044.

[159] Tsougeni K, Boulousis G, Gogolides E, Tserepi A. Oriented spontaneously formed nano-structures on poly(dimethylsiloxane) films and stamps treated in O_2 plasmas. 33rd International Conference on Micro- and Nano-Engineering. Copenhagen, Denmark: Elsevier Science Bv, 2007. p.1233.

[160] Tsougeni K, Tserepi A, Boulousis G, Constantoudis V, Gogolidesk E. Control of Nanotexture and Wetting Properties of Polydimethylsiloxane from Very Hydrophobic to Super-Hydrophobic by Plasma Processing. Plasma Processes and Polymers 2007;4:398.

[161] Vlachopoulou ME, Petrou PS, Kakabakos SE, Tserepi A, Beltsios K, Gogolides E. Effect of surface nanostructuring of PDMS on wetting properties, hydrophobic recovery and protein adsorption. Microelectronic Engineering 2009;86:1321.

[162] Tserepi AD, Vlachopoulou ME, Gogolides E. Nanotexturing of poly(dimethylsiloxane) in plasmas for creating robust super-hydrophobic surfaces. Nanotechnology 2006;17:3977.

[163] Yan YH, Chan-Park MB, Yue CY. CF4 Plasma Treatment of Poly(dimethylsiloxane): Effect of Fillers and Its Application to High-Aspect-Ratio UV Embossing. Langmuir 2005;21:8905.

[164] Cortese B, D'Amone S, Manca M, Viola I, Cingolani R, Gigli G. Superhydrophobicity Due to the Hierarchical Scale Roughness of PDMS Surfaces. Langmuir 2008;24:2712.

[165] Manca M, Cortese B, Viola I, Arico AS, Cingolani R, Gigli G. Influence of Chemistry and Topology Effects on Superhydrophobic CF4-Plasma-Treated Poly(dimethylsiloxane) (PDMS). Langmuir 2008;24:1833.

[166] Vlachopoulou ME, Tserepi A, Beltsios K, Boulousis G, Gogolides E. Nanostructuring of PDMS surfaces: Dependence on casting solvents. Microelectronic Engineering 2007;84:1476.

[167] Kaless A. Oberflächenmodifizierung von Polymethylmethacrylat durch Plasmabehandlung. Halle-Wittenberg: Martin-Luther-Universität 2006.

[168] http://www.iof.fhg.de/departments/optical-coatings/plastics/index_e.html.

[169] de Gennes PG. Wetting: statics and dynamics. Rev. Mod. Phys. 1985;57:827.

[170] Wenzel RN. Resistance of solid surfaces to wetting by water. Industrial and Engineering Chemistry 1936;28:988.

[171] Cassie ABD, Baxter S. Wettability of porous surfaces. Trans. Faraday Soc. 1944;40:0546.

[172] Allen KW. Adhesion and Adhesives. In: Meyers RA, editor. Encyclopedia of Physical Science and Technology, vol. 1. San Diego: Academic Press, 2002. p.237.

[173] Hamaker HC. The London - Van Der Waals attraction between spherical particles. Physica 1937;4:1058.

[174] Tipler PA. Physics for scientists and engineers. New York, 1999.

[175] Israelachvili J. Intermolecular and Surface Forces. New York: Academic Press, 1992.

[176] Puente P, Delgado R, Moñivas S. Rev. Plast. Mod. 2004;88:46.

[177] Peressadko AG, Hosoda N, Persson BNJ. Influence of surface roughness on adhesion between elastic bodies. Physical Review Letters 2005;95.

[178] Chu CM, Wilkes GL. Superstructure in Chemically Etched Poly(Ethylene Terephthalate). Journal of Macromolecular Science-Physics 1974;B 10:551.

[179] Michler GH, Lebek W. Ultramikrotomie in der Materialforschung. München, 2004. p.69, p.90, p.115.

[180] Wunderlich B. Macromolecular Physics. Crystal Structure, Morphology, Defects, Vol. 1. New York: Academic Press, 1973. p.389.

[181] Cheng SZD, Wunderlich B. Glass-Transition and Melting Behavior of Poly(Ethylene-2,6-Naphthalenedicarboxylate). Macromolecules 1988;21:789.

[182] Ehrenstein GW, Pongratz S. Beständigkeit von Kunststoffen. München: Carl Hanser Verlag, 2007. p.160.

[183] Windle AH. Measurement of Molecular Orientation and Structure in Non-Crystalline Polymers by Wide Angle X-Ray Diffraction. In: Ward IM, editor. Developments in Oriented Polymers - 1. London: Applied Science Publisher, 1982. p.1.

[184] Balta Calleja FJ, Vonk CG. X-Ray Scattering of Synthetic Polymers. Amsterdam: Elsevier, 1989.

[185] Spurr AR. A low-viscosity epoxy resin embedding medium for electron microscopy. Journal of Ultrastructure Research 1969;26:31.

[186] Berthe RA. Einfluss der Feinstruktur von Schlangenschuppen auf die Reibung. Diplomarbeit 2007.

[187] Inagaki N, Narushim K, Tuchida N, Miyazak K. Surface Characterization of Plasma-Modified Poly(ethylene terephthalate) Film Surfaces. Journal of Polymer Science Part B-Polymer Physics 2004;42:3727.

[188] Weikart CM, Yasuda HK. Modification, degradation, and stability of polymeric surfaces treated with reactive plasmas. Journal of Polymer Science Part a-Polymer Chemistry 2000;38:3028.

[189] White JR. Polymer ageing: physics, chemistry or engineering? Time to reflect. C. R. Chim. 2006;9:1396.

[190] Viana JC, Mano JF, Denchev ZZ, Oliveira MJ, Cramez MC. Nanostructure evolution during uni-axial deformation of PET - a WAXS and SAXS study using synchrotron radiation. Advanced Materials Forum Iii, Pts 1 and 2, vol. 514-516. 2006. p.1583.

[191] Haubruge HG, Jonas AM, Legras R. Staining of poly(ethylene terephthalate) by ruthenium tetroxide. Polymer 2003;44:3229.

[192] Haubruge HG, Jonas AM, Legras R. Morphological study of melt-crystallized poly(ethylene terephthalate). A. Comparison of transmission electron microscopy and small-angle X-ray scattering of bulk samples. Macromolecules 2004;37:126.

[193] Komoto T, Takai T. A Preparative Method for Transmission Electron Microscopy of Poly(ethylene terephthalate) and Poly(ethylene-2, 6-naphthalate). Sen'i Gakkaishi 2002;57:277.

[194] Trent J, Scheinbeim J, Couchman P. Ruthenium Tetraoxide Staining of Polymers for Electron Microscopy. Macromolecules 1982;16:589.

[195] Xia Z, Sue H-J, Wang Z, Avila-Orta CA, Hsiao BS. Determination of crystalline lamellar thickness in Poly(ethylene terephthalate) using small-angle x-ray scattering and transmission electron microsocopy. Journal of Macromolecular Science, Part B 2001;40:625.

[196] Grace JM, Gerenser LJ. Plasma treatment of polymers. Journal of Dispersion Science and Technology 2003;24:305.

[197] Goldman M, Goldman A, Sigmond RS. The Corona Discharge, its Properties and Specific Uses. Pure and Applied Chemistry 1985;57:1353.

[198] Blöß S. personal communication. 2005.

[199] Pelletier J, Arnal Y, Joubert O. Etching mechanisms of polymers in oxygen microwave multipolar plasmas. Applied Physics Letters 1988;53:1914.

[200] Eisenlohr J. personal communication, 29.1.2010.

[201] Boenig HV. Fundamentals of plasma chemistry and technology. Lancaster: Technomic Pub. Co., 1988. p.167.

[202] Eisenlohr J. personal communication, 11.5.2009.

[203] Dems BC, Rodriguez F. The role of heat transfer during reactive-ion etching of polymer films. Journal of Vacuum Science & Technology B 1990;8:1985.

[204] Pons M, Joubert O, Paniez P, Pelletier J. Plasma etching of polymers: A reinvestigation of temperature effects. Journal of Applied Physics 1991;70:2376.

[205] Egitto FD, Vukanovic V, Taylor GN. Plasma Deposition, Treatment, and Etching of Polymers. In: d'Agostino R, editor. Plasma - Materials Interactions. San Diego: Academic Press, Inc., 1990. p.358.

[206] Joubert O, Paniez P, Pelletier J, Pons M. Etching of polymers by oxygen plasmas: Influence of viscoelastic properties. Applied Physics Letters 1991;58:959.

[207] Hyun J, Aspnes DE, Cuomo JJ. Nondestructive Measurement of a Glass Transition Temperature at Spin-Cast Semicrystalline Polymer Surfaces. Macromolecules 2001;34:2395.

[208] Herbert S, Shinozaki DM, Collacott RJ. Fine-scale morphology of ultraviolet-ozone etched polyethylene. Journal of Materials Science 1996;31:4655.

[209] Riekerink MBO, Terlingen JGA, Engbers GHM, Feijen J. Selective etching of semicrystalline polymers: CF4 gas plasma treatment of poly(ethylene). Langmuir 1999;15:4847.

[210] Fischer EW, Fakirov S. Structure and properties of polyethyleneterephthalate crystallized by annealing in the highly oriented state. Part 1 Morphological structure as revealed by small-angle X-ray scattering. Journal of Materials Science 1976;11:1041.

[211] Kirov KR, Assender HE. Quantitative ATR-IR analysis of anisotropic polymer films: Surface structure of commercial PET. Macromolecules 2005;38:9258.

[212] Cole KC, Ajji A, Pellerin E. New insights into the development of ordered structure in poly(ethylene terephthalate). 1. Results from external reflection infrared spectroscopy. Macromolecules 2002;35:770.

[213] Jabarin SA. Optical Properties of Thermally Crystallized Poly(ethylene terephthalate). Polym. Eng. Sci. 1982;22:815.

[214] Kawakami D, Burger C, Ran SF, Avila-Orta C, Sics I, Chu B, Chiao SM, Hsiao BS, Kikutani T. New insights into lamellar structure development and SAXS/WAXD sequence appearance during uniaxial stretching of amorphous poly(ethylene terephthalate) above glass transition temperature. Macromolecules 2008;41:2859.

[215] Hristov HA, Schultz JM. Thermal Response and Structure of PET Fibers. Journal of Polymer Science Part B-Polymer Physics 1990;28:1647.

[216] Adams GC. Structure Studies of Chemically Etched Poly(Ethylene Terephthalate) Film. Polym. Eng. Sci. 1976;16:222.

[217] Beake BD, Leggett GJ, Shipway PH. Nanotribology of biaxially oriented poly(ethylene terephthalate) film. Polymer 2001;42:7025.

[218] Beake BD, Shipway PH, Leggett GJ. Influence of mechanical properties on the nanowear of uniaxially oriented poly(ethylene terephthalate) film. Wear 2004;256:118.

[219] Zhang ZY, Boyd IW, Esrom H. Surface Modification of Polyethylene Terephthalate with Excimer UV Radiation. Surf. Interface Anal. 1996;24:718.

[220] Lazare S, Srinivasan R. Surface Properties of Poly(ethylene terephthalate) Films Modified by Far-Ultraviolet Radiation at 193 nm (Laser) and 185 nm (Low Intensity). J. Phys. Chem. 1986;90:2124.

[221] Brezini A. Surface Properties of Polyethylene Terephthalate Films Modified by Far UV Radiation at 193 nm. Phys. Status Solidi A-Appl. Res. 1993;135:589.

[222] Novis Y, Pireaux JJ, Brezini A, Petit E, Caudano R, Lutgen P, Feyder G, Lazare S. Structural Origin of Surface Morphological Modifications Developed on Poly(Ethylene-Terephthalate) by Excimer Laser Photoablation. Journal of Applied Physics 1988;64:365.

[223] Bityurin N, Arenholz E, Arnold N, Bauerle D. Laser-induced structure formation on stretched polymer foils. Physical Review E 2007;75:8.

[224] Beake BD, Ling JSG, Leggett GJ. Scanning force microscopy investigation of poly (ethylene terephthalate) modified by argon plasma treatment. Journal of Materials Chemistry 1998;8:1735.

[225] Arenholz E, Heitz J, Wagner M, Bauerle D, Hibst H, Hagemeyer A. Laser-Induced Surface Modification and Structure Formation of Polymers. Applied Surface Science 1993;69:16.

[226] Bäuerle D. Laser Processing and Chemistry. Berlin Heidelberg: Springer, 2000. p.612.

[227] Wrobel AM, Lamontagne B, Wertheimer MR. Large Area Microwave and Radiofrequency Plasma Etching of Polymers. Plasma Chem. Plasma Process. 1988;8:315.

[228] Hansen RH, Pascale JV, Debenedi T, Rentzepi PM. Effect of Atomic Oxygen on Polymers. Journal of Polymer Science Part a-General Papers 1965;3:2205.

[229] Petasch W, Rauchle E, Muegge H, Muegge K. Duo-Plasmaline - a linearly extended homogeneous low pressure plasma source. Surface & Coatings Technology 1997;93:112.

[230] Liu H, Zhang H, Chen J. Surface analysis of long-distance oxygen plasma sterilized PTFE film. Applied Surface Science 2009;255:8115.

[231] Garra J, Long T, Currie J, Schneider T, White R, Paranjape M. Dry etching of polydimethylsiloxane for microfluidic systems. Journal of Vacuum Science & Technology a-Vacuum Surfaces and Films 2002;20:975.

[232] Matthews SR, Hwang YJ, McCord MG, Bourham MA. Investigation into etching mechanism of polyethylene terephthalate (PET) films treated in helium and oxygenated-helium atmospheric plasmas. Journal of Applied Polymer Science 2004;94:2383.

[233] Tsougeni K, Vourdas N, Tserepi A, Gogolides E, Cardinaud C. Mechanisms of oxygen plasma nanotexturing of organic polymer surfaces: from stable super hydrophilic to super hydrophobic surfaces. Langmuir 2009;25:11748.

[234] Beake BD, Ling JSG, Leggett GJ. Correlation of friction, adhesion, wettability and surface chemistry after argon plasma treatment of poly(ethylene terephthalate). Journal of Materials Chemistry 1998;8:2845.

[235] Bowden FP, Tabor D. The friction and lubrication of solids. Oxford: Clarendon Press, 1950. p.98.

[236] Majidi C, Groff RE, Maeno Y, Schubert B, Baek S, Bush B, Maboudian R, Gravish N, Wilkinson M, Autumn K, Fearing RS. High friction from a stiff polymer using microfiber arrays. Physical Review Letters 2006;97.

[237] Aksak B, Sitti M, Cassell A, Li J, Meyyappan M, Callen P. Friction of partially embedded vertically aligned carbon nanofibers inside elastomers. Applied Physics Letters 2007;91:061906.

[238] Autumn K, Dittmore A, Santos D, Spenko M, Cutkosky M. Frictional adhesion: a new angle on gecko attachment. Journal of Experimental Biology 2006;209:3569.

[239] Lee J, Fearing RS, Komvopoulos K. Directional adhesion of gecko-inspired angled microfiber arrays. Applied Physics Letters 2008;93:191910.

10. Deutsche Kurzzusammenfassung der Dissertation

10.1 Motivation und Literaturüberblick

Die Natur hat viele alltäglichen Probleme gelöst, die Ingenieure in der Technik beschäftigen. Deshalb dienen Pflanzen und Tiere der Menschheit seit langem als Vorbild für innovative Ideen. Im Laufe der Evolution wurden vielseitige Oberflächen entwickelt, um sich besser an die Umgebungsbedingungen anzupassen. Bekannte Beispiele sind die Haifischhaut (Reduzierung des Reibungswiderstands) [51], der Lotus-Effekt (selbst-reinigende Oberflächen) [55-58], die Mottenaugen (entspiegelte Oberflächen) [49, 50] oder auch die Geckohaftung [1, 66, 72, 74]. Die Füße des Geckos sind mit feinen Hafthaaren bedeckt, die sehr stark haften, aber trotzdem einfach abzulösen sind und keine klebrigen Rückstände hinterlassen. Zudem sind diese Hafthaare selbstreinigend.

Inspiriert von der Natur entwickelte sich ein großes Interesse, Mikro- und Nanostrukturen auf technische Anwendungen zu übertragen, um dieses Potential zur Verbesserung von Produkten zu nutzen und zum Beispiel ein Gecko-Klebeband herzustellen. Innovative Entwicklungen im Bereich der Mikro- und Nanotechnologie haben dazu geführt, dass eine große Bandbreite an Strukturierungsmethoden vom Millimeter- bis in den Nanometerbereich entstanden ist. Dazu zählen zum Beispiel Methoden wie Lithographieverfahren [76-81, 89-93], Rastersondenmikroskopie [82, 95], Transferdruck [118-123], Strukturierung mittels Instabilitäten im elektrischen Feld [82, 125], kontrollierte Faltenbildung [42, 43], oder die Übertragung eines Musters mittels Plasmaätzen [11, 128]. Jede einzelne Technik hat individuelle Einschränkungen, es

werden eine spezielle Ausstattung wie Reinräume, Masken oder Template benötigt, der Herstellungsprozess ist langwierig, teuer oder aufwendig, oder es lassen sich nur sehr kleine Bereiche strukturieren. Ziel dieser Arbeit ist es, eine einfache, billige und schnelle Methode zu entwickeln, mit der geckoähnliche Nanostrukturen auf Polymeroberflächen hergestellt werden können. Das Plasmaätzen von Polymeroberflächen scheint dafür eine geeignete Technik zu sein. Während der Plasmabehandlung wird die Oberfläche gereinigt, abgetragen, Polymerketten vernetzt und die Oberflächenchemie verändert [139]. Dabei werden im Polymer amorphe Bereiche stärker abgetragen als kristalline Bereiche, was zu einer Aufrauung und Strukturierung der Oberfläche führt [139]. Es wurden Versuche an einer Vielzahl von Polymeren wie PET [24, 142-146], PE [33], Cellulose [22], PMMA [28, 29, 31, 147, 148, 150], PTFE [35-37, 151], Fotolack [153-155], oder PDMS [40-42, 159, 160] durchgeführt. Die hergestellten Strukturen wurden auf Adhäsion, Superhydrophobizität oder Entspiegelungsvermögen untersucht. Eine systematische Untersuchung auf den Einfluss der einzelnen Plasmaparameter auf die entstehenden Nanostrukturen wurde in der Literatur bisher nicht durchgeführt. Der Schwerpunkt dieser Arbeit liegt daher auf einer gezielten Untersuchung des Einflusses der Plasma- und Polymerparameter auf die Entstehung von Nanostrukturen. Ziel ist es, geckoähnliche haarige Strukturen herzustellen und den Herstellungsmechanismus zu verstehen sowie zu kontrollieren. Für die Versuche wurde das Polymer Poly(ethylene terephthalate) (PET) als Modellsystem ausgewählt. Aus der Literatur war bereits bekannt, dass es mit Hilfe eines Sauerstoffplasmas möglich ist, auf PET Nanosäulen herzustellen, die den Geckohafthaaren ähneln [24].

10.2 Experimentelles

Nachdem die Herstellung von säulenartigen Nanostrukturen auf kommerziell erhältlichen PET-Folien durch reaktives Ionenätzen mit Sauerstoff gelungen war, wurden systematisch zuerst die Plasmabedingungen variiert und danach der Einfluss der Polymerparameter auf die Säulenbildung untersucht. Folgende Plasmaparameter wurden analysiert: Prozessgas, Prozessdruck, Leistung, Behandlungsdauer und Elektrodentemperatur. Die Proben wurden anschließend mittels Rasterelektronenmikroskopie untersucht. Für die weiteren Versuche wurden Plasmaparameter verwendet, mit denen möglichst lange und freistehende Nanosäulen hergestellt werden konnten. Anschließend wurde der Einfluß der Materialeigenschaften analysiert. Sowohl kommerzielle als auch selbst hergestellte Folien unterschiedlicher Kristallinität wurden plasmabehandelt und auf Gewichtsverlust und entstehende Oberflächenstrukturen untersucht. Des Weiteren wurde der Einfluß der Orientierung der Polymerketten durch uniaxiales und biaxiales Strecken auf die Anordnung der Nanostrukturen analysiert. Mit Hilfe uniaxialer Zugversuche an selbsthergestellten Filmen wurden Proben mit unterschiedlicher uniaxialer Orientierung hergestellt. Die auf diesen Proben entstandenen Nanosäulen wurden mit denen auf kommerziell erhältlichen Fäden und Filmen verglichen. Zudem wurde der Einfluss der chemischen Struktur auf entstehende Nanostrukturen untersucht. Verschiedene Polymerfilme wurden mit den gleichen Plasmabedingungen behandelt und die Ergebnisse mit der Literatur verglichen. Im letzten Teil der Arbeit wurden die Eigenschaften der plasmastrukturierten Proben in Bezug auf Benetzbarkeit der Oberfläche, Adhäsion und Reibung untersucht und mit glatten Folien verglichen.

10.3 Ergebnisse und Diskussion

Durch reaktives Ionenätzen konnten Nanostrukturen in Form von Körnern und Säulen auf der PET-Oberfläche hergestellt werden. Abhängig von den verwendeten Plasmaparametern wuchsen aus den Körnern mit zunehmender Behandlungszeit Nanosäulen. Die Länge der Nanosäulen stieg dabei mit steigendem Sauerstoffgehalt im Prozessgas an. Deshalb wurde in den weiterführenden Versuchen ausschließlich mit reinem Sauerstoffplasma gearbeitet. Durch wiegen der Proben direkt vor und nach der Plasmabehandlung wurde ein Gewichtsverlust während der Plasmabehandlung festgestellt. Das bedeutet, dass die PET-Oberfläche wie erwartet durch einen Ätzprozess abgetragen wurde. Eine systematische Untersuchung der einzelnen Plasmaparameter ergab, dass sowohl der Gewichtsverlust als auch die Säulenlänge mit zunehmender Behandlungsdauer, zunehmender Leistung, steigender Probentemperatur und sinkendem Druck zunahm. Die entstandenen Strukturen erreichten einen Durchmesser zwischen 15 und 40 nm und eine Länge bis zu 1 µm. Eine Änderung der Plasmaparameter hatte keinen Einfluss auf Durchmesser und Abstand der Säulen. Bis zu einem Aspektverhältnis (Verhältnis von Länge zu Durchmesser) von 3 entstanden freistehende Säulen. Stieg das Aspektverhältnis weiter an, wurden die Säulen instabil und begannen zusammenzukleben.

Um mehr über den Einfluss der Materialparameter auf die Entstehung der Nanosäulen zu lernen, wurden Versuche mit PET-Proben unterschiedlicher Kristallinität und Orientierung der Polymermoleküle durchgeführt. Dazu wurden amorphe und teilkristalline PET-Filme mit Hilfe einer Presse hergestellt. Die Filme wurden bei 100 W,

0,1 mbar und Raumtemperatur für verschiedene Zeiten plasmabehandelt. Sowohl auf dem amorphen als auch auf dem teilkristallinen Film entstanden ähnliche Körner und Säulen. Bei kurzen Behandlungszeiten von bis zu 5 Minuten waren die Strukturen auf dem amorphen Film allerdings weniger deutlich zu erkennen als auf dem teilkristallinen Film. Dieser Unterschied verschwand bei Behandlungszeiten von 10 Minuten und mehr. Der Gewichtsverlust durch die Plasmabehandlung war bei amorphen Proben bei niedrigen Behandlungszeiten (bis 10 Minuten) höher als in der teilkristallinen Probe. Wurde die Plasmadauer erhöht, so glich sich der Gewichtsverlust an. Ab 45 Minuten Plasmadauer änderte sich das Verhalten der amorphen Probe. Nun wurde ein geringerer Gewichtsverlust als in der teilkristallinen Probe beobachtet. Dies deutete darauf hin, dass sich die Morphologie der amorphen Probe während der Plasmabehandlung änderte.

Durch Temperaturmessungen während der Plasmabehandlung wurde ein Ansteigen der Elektrodentemperatur beobachtet, das durch den kontinuierlichen Beschuss mit Ionen verursacht wird. Nach einer Stunde Behandlungsdauer erhöhte sich die Temperatur von 24°C auf 80°C. Da die Proben während der Plasmabehandlung auf dieser Elektrode positioniert waren, erhöhte sich die Probentemperatur ebenfalls. Mittels DSC-Messungen wurde festgestellt, dass die Glasübergangstemperatur T_g der amorphen Probe bei 75°C und die Kristallisationstemperatur T_c bei 150°C lagen. Eine Kristallisation der Probe während der Plasmabehandlung konnte ausgeschlossen werden. Weitere DSC-Messungen der plasmabehandelten amorphen Filme zeigten, dass es während der Plasmabehandlung zu einer physikalischen Alterung des Polymers kam. Dadurch entstanden verdichtete amorphe Bereiche, die vermutlich eine geringere Ätzrate als das

umgebende amorphe Material haben und dadurch für die entstehenden Nanostrukturen verantwortlich sein könnten. In teilkristallinen Proben konnten keine Alterungseffekte festgestellt werden. Da kristalline und amorphe Bereiche aber ebenfalls unterschiedliche Ätzraten aufweisen, dienen in diesem Fall vermutlich die Kristallite als Ätzmasken, durch die die beobachteten Nanostrukturen entstehen.

Die Orientierung der Molekülketten wurde als weiterer Materialparameter untersucht. Dazu wurden uniaxiale Zugversuche bei 100°C mit selbstgemachten amorphen und teilkristallinen PET-Filmen durchgeführt. Ein Teil der Proben wurde im Anschluss an den Zugversuch im eingespannten Zustand bei ebenfalls 100°C ausgelagert. Probenstücke aus dem gestreckten Bereich und dem eingeklemmten Ende wurden für 10 Minuten bei 100 W und 0,1 mbar plasmabehandelt. Dies ermöglichte den direkten Vergleich von orientiertem und nichtorientiertem Probenmaterial mit gleicher Temperaturbehandlung. In nicht orientieren Proben entstanden Nanosäulen, die keinerlei Vorzugsrichtung aufwiesen. Nanosäulen mit gleicher Größe und Verteilung wurden auch in uniaxial gestreckten und anschließend ausgelagerten Proben gefunden. Es konnten keine Unterschiede zwischen nicht orientierten Proben sowie gestreckten und ausgelagerten Proben festgestellt werden. Durch das Auslagern kommt es zu verschiedenen Effekten wie Kettenrelaxation, Kristallisation amorpher Bereiche, Reorganisation von amorphen und kristallinen Bereichen und Ausheilung von Defekten. Dadurch relaxiert die Mikrostruktur der PET Probe und nähert sich dem thermischen Gleichgewichtszustand an. Die Probe vergisst dabei zu einem gewissen Teil ihre mechanische Vorbehandlung. Wurden die Proben nach dem Streckvorgang direkt aus

dem Gerät ausgebaut und auf Raumtemperatur abgekühlt, so zeigte sich eine Orientierung der Nanosäulen senkrecht zur Streckrichtung. Diese Orientierung wurde sowohl in amorphen als auch in kristallinen Filmen beobachtet. Die Frage, warum sich die Säulen senkrecht zur Streckrichtung orientieren ist noch ungeklärt.

Eine Plasmabehandlung von kommerziell erhältlichen amorphen PET-Fäden führte ebenfalls zur Entstehung von Nanosäulen auf der dem Plasma zugewandten Fadenseite. Auch hier wurde eine Orientierung der Nanosäulen senkrecht zur herstellungsbedingten Streckrichtung beobachtet. In biaxial gestreckten, kommerziell erhältlichen Folien wurde keine Orientierung der Nanosäulen gefunden.

Vergleicht man orientierte mit unorientierten Proben, so fällt ein Unterschied ins Auge: Die Nanosäulen in den orientierten Proben sind durch wellenartige Erhöhungen miteinander verbunden und Proben ohne Orientierung zeigen keinerlei Verbindungen zwischen den Säulen. Es wird vermutet, dass sich während des Streckvorgangs orientierte amorphe Bereiche bilden, deren Ätzrate im Plasma höher ist als von kristallinen Bereichen, aber auch geringer als von nicht orientiertem amorphen PET.

Teilkristallines PET kann nicht als einfaches Zwei-Phasen Modell bestehend aus amorphen und kristallinen Bereichen beschrieben werden. Versuche mit uniaxial gestrecktem amorphen PET zeigen, dass gleichzeitig kristalline, amorphe und mesomorphe Phasen in einer gestreckten Probe vorliegen. Das Verhältnis dieser Phasen hängt dabei von den Zugbedingungen und der Temperatur ab [214]. Wir vermuten, dass

die Ätzraten diese mesomorphen Phasen im Plasma zwischen denen der rein amorphen und kristallinen Bereiche liegen.

Es wurde versucht, die Strukturierung mittels Plasmabehandlung auf andere Polymere zu übertragen. Die chemische Struktur des Polymers beeinflusst die Wechselwirkung des Materials mit dem Plasma, daher werden unterschiedliche Ätzraten von den verschiedenen Polymeren erwartet. Auf den Polymeren PEN und PBT, die eine ähnliche chemische Struktur wie PET aufweisen, konnten bei gleichen Plasmabedingungen Nanosäulen hergestellt werden. Auch auf zwei unterschiedlichen Teflonfilmen gelang die Erzeugung von Nanosäulen, die deutlich länger waren als auf PET. Auf PE, PS und PMMA entstanden körnige Strukturen in der Größenordnung von einigen 10 bis mehreren 100 nm, während sich auf der Oberfläche von PDMS ein wellenförmiges Muster bildete. Aus den vorliegenden Ergebnissen und dem Vergleich mit Literaturwerten konnte keine Beziehung zwischen Polymerchemie, Mikrostruktur, Ätzrate und Säulenentstehung hergestellt werden. Aber es konnte gezeigt werden, dass Plasmastrukturierung auch auf andere Polymere angewendet werden kann. Um Nanosäulen zu erzeugen müssen die Plasmaparameter jedoch auf jedes einzelne Material abgestimmt werden.

Unsere Ergebnisse zeigen einen deutlichen Zusammenhang zwischen der Mikrostruktur und der entstehenden Oberflächentopographie. Daher nehmen wir an, dass amorphe, teilkristalline und mesomorphe Bereiche unterschiedliche Ätzraten im Sauerstoffplasma aufweisen und dadurch die beobachteten Nanostrukturen entstehen. Die thermische und

mechanische Vorbehandlung der Proben bestimmt die endgültige Oberflächenstruktur. Allerdings ist noch nicht ganz klar, warum die Nanostrukturen in amorphen und teilkristallinen Proben sehr ähnlich aussehen.

Im letzten Teil der Arbeit wurden die Eigenschaften der strukturierten Oberflächen untersucht. Unbehandelte PET-Filme haben einen Wasserkontaktwinkel von etwa 60°. Durch die Behandlung mit einem Sauerstoffplasma wurde die Oberfläche stark hydrophil (≈ 0°). Durch Beschichtung mit einem Fluorsilan konnte eine hydrophobe Oberfläche hergestellt werden. Wurde nun die Plasmabehandlung, die zu einer Erhöhung der Oberflächenrauigkeit führt, mit der Beschichtung kombiniert, konnte der Kontaktwinkel weiter erhöht werden. Bei einer Plasmadauer zwischen 0 und 10 Minuten konnten die Wassertropfen die Oberfläche benetzen. Wurde die Plasmadauer auf 20 Minuten und mehr ausgedehnt, war eine Benetzung nicht mehr möglich und die Tropfen rollten von der Oberfläche. Durch die Kombination von Plasmabehandlung und der Beschichtung der Oberfläche mit einem Fluorsilan konnte ein Lotus-Effekt auf der PET-Oberfläche erzeugt werden.

Adhäsionsmessungen wurden mit flachen und nanostrukturierten Filmen durchgeführt. Die glatten Proben zeigten eine Adhäsion im Bereich mehrerer hundert µN, während die Obergrenze der strukturierten Proben im Bereich von 10 µN lag. Die niedrigen Haftwerte lassen sich durch die geringe Dichte der Nanosäulen und der dadurch stark reduzierten Kontaktfläche erklären. Gleichzeitig verhindert die steife PET-Folie eine Anpassung der

Säulen an den Untergrund, was die Kontaktfläche zusätzlich verringerte. Eine Folie mit geckoähnlichen Hafteigenschaften konnte somit leider nicht hergestellt werden.

Reibungsmessungen ergaben bei flachen Filmen eine Abnahme des Reibungskoeffizienten mit zunehmender Substratrauigkeit, während bei strukturierten Proben ein Anstieg zu beobachten war. Dieser Anstieg lässt sich mit einer Zunahme von Verhakungen zwischen den Nanosäulen und der steigenden Unebenheit der Substrate erklären.

Insgesamt konnte im Rahmen der vorliegenden Arbeit gezeigt werden, dass es möglich ist die Oberfläche von PET mittels einer Plasmabehandlung zu strukturieren. Dabei konnten sowohl Körner als auch Säulen mit einem Durchmesser von 15 bis 40 nm und einer Länge bis zu 1 µm hergestellt werden. Die Strukturierung ist einfach und schnell und außer einem Plasmagerät wird kein weiteres Zubehör benötigt. Es können große Flächen behandelt werden und zudem ist es möglich nicht nur flache sondern auch gekrümmte Proben zu strukturieren. Die Polymermikrostruktur, die durch thermische und mechanische Vorbehandlungen beeinflusst wird, beeinflusst die erhaltene Oberflächenstruktur, da amorphe, kristalline und mesomorphe Phasen unterschiedliche Ätzraten aufweisen. Es wurde gezeigt, dass diese Strukturierungsmethode auch auf andere Polymere angewendet werden kann. Dabei müssen die einzelnen Plasmaparameter jedoch gezielt auf das jeweilige Material abgestimmt werden. Durch die Kombination von Plasmabehandlung und der Beschichtung mit Fluorsilan konnten superhydrophobe Oberflächen hergestellt werden. Strukturierte Proben zeigten im Vergleich zu

unbehandelten PET-Filmen eine sehr geringe Adhäsion. Eine geckoähnliche Klebefolie konnte nicht hergestellt werden.